A FINITE ELEMENT METHOD AND THE METHOD OF FINITE SPHERES ENRICHED FOR ANALYSIS OF WAVE PROPAGATIONS

by

SEOUNGHYUN HAM
M.Eng., University of Illinois at Urbana-Champaign, 2007

Submitted to the Department of Mechanical Engineering
in Partial Fulfilment of the Requirements for the Degree of

DOCTOR OF PHILOSOPHY IN MECHANICAL ENGINEERING

at the

MASSACHUSETTS INSTITUTE OF TECHNOLOGY

[september 2014]
August 2014

Signature redacted

Author ....

Seounghyun Ham
Department of Mechanical Engineering
August 6, 2014

Signature redacted

Certified by ....

Klaus-Jürgen Bathe
Professor of Mechanical Engineering
Thesis Supervisor

Signature redacted

Accepted by ....

David Edgar Hardt
Professor of Mechanical Engineering
Chairman, Departmental Committee on Graduate Students

A FINITE ELEMENT METHOD AND THE METHOD OF FINITE SPHERES ENRICHED FOR ANALYSIS OF WAVE PROPAGATIONS

by

Seounghyun Ham

Submitted to the Department of Mechanical Engineering
on August 6, 2014 in Partial Fulfilment of the
Requirements for the Degree of Doctor of Philosophy in
Mechanical Engineering

Abstract

The objective of this thesis is to present a finite element method and the method of finite spheres enriched for the solution of various wave propagation problems. The first part of this thesis is to present an enriched finite element method which is an extension of the procedure introduced by Kohno, Bathe, and Wright for one dimensional problems [1]. Specifically, the novelties are: two-dimensional problems are solved (and three-dimensional problems would be tackled similarly), a scheme is given to overcome ill-conditioning, the method is presented for time-dependent problems, and focus is on the solution of problems in solids and structures using real arithmetic only. The method combines advantages of finite element and spectral techniques, but an important point is that it preserves the fundamental properties of the finite element method. The second part of this thesis focuses on developing the method of finite spheres for the analysis of wave propagations. This method is a truly meshless technique developed for the solution of boundary value problems on geometrically complex domains [2 - 5]. In the new development trigonometric functions are used to interpolate the solution of wave propagations. An effective numerical integration rule resulting in a significant reduction in computational cost is presented. Several numerical examples are provided demonstrating the effectiveness of the scheme.

Thesis Supervisor: Klaus-Jürgen Bathe

Title: Professor of Mechanical Engineering

Acknowledgements

I sincerely appreciate to my thesis supervisor, Professor Klaus-Jürgen Bathe, for his lovely caring and great trust on me. I wanted to be involved into *the finite element method world* for my PhD only to work with him who is a true *Doktorvater* at MIT and without him, I couldn't have a chance to have this thesis done. I am truly grateful of him.

I also thank my other thesis committee members, Professors Tomasz Wierzbicki and Eduardo Kausel, also for their valuable guidance and suggestions to get my thesis to be a current version and their encouragements during my studies at MIT.

I sincerely thank *the light and truth church* in South Korea. A group of about twelve people have helped and supported and cared for me to get this thesis done. Especially Dr Jun Lee had lived with me together and helped and encouraged me to be able to complete the work on this thesis. He had cared for me and sincerely loved me. I also sincerely thank to Hosik Yu who has lived with me together after Dr Jun Lee left and helped and loved me.

Finally, I give *my most valuable thanks* to Kyungmin Ma who is my mentor and father and saved my life for his unconditional love towards me. Especially When he reproached me for my selfish and thoughtless behaviors, I felt great love from

him. Without his love, I couldn't finish this thesis. I am truly grateful of his help and willingly dedicate this thesis to him.

Contents

CHAPTER 1 INTRODUCTION 14

1.1 OVERVIEW 14

1.2 THESIS OUTLINE 21

CHAPTER 2 A FINITE ELEMENT METHOD ENRICHED FOR WAVE PROPAGATION PROBLEMS 23

2.1 FORMULATION OF THE METHOD 23

2.1.1 Governing continuum mechanics equations 24

2.1.2 Variational form of the governing continuum mechanics equations . 25

2.1.3 Element interpolation functions 25

2.1.4 Imposing boundary conditions 27

2.1.5 Geometrically distorted elements 28

2.1.6 A scheme to overcome the (possible) ill-conditioning of the algebraic equations 30

2.2 NUMERICAL EXAMPLES 32

2.2.1 Solution of time harmonic scalar wave 32

2.2.2 Solution of transient scalar wave 34

2.2.3 One-dimensional impact of an elastic bar 38

2.2.4 Solution of two-dimensional P, S and Rayleigh waves 40

2.2.5 Solution of time harmonic acoustic pressure wave 42

CHAPTER 3 THE METHOD OF FINITE SPHERES ENRICHED FOR WAVE PROPAGATION PROBLEMS 47

3.1 METHOD OF FINITE SPHERES INTERPOLATION FUNCTIONS 47
  3.1.1 The partition of unity functions 48
  3.1.2 The interpolation functions for wave propagation 50
3.2 WAVE PROPAGATIONS IN 2D 53
  3.2.1 Formulation for the linear elastic wave equation 53
    3.2.1.1 Variational form 54
    3.2.1.2 Nodal interpolations 55
    3.2.1.3 Discrete equations 56
  3.2.2 Formulation for the linear viscoelastic wave equation 58
    3.2.2.1 Discrete equations 61
3.3 IMPROVED NUMERICAL INTEGRATION PROCEDURE 62
  3.3.1 Piecewise midpoint quadrature rule 62
  3.3.2 Piecewise Gauss-Legendre quadrature rule 63
    3.3.2.1 Interior disk 64
    3.3.2.2 Boundary sector 65
  3.3.3 Numerical integration rule comparison 66
    3.3.3.1 Strain energy convergence 69
    3.3.3.2 Cantilever plate problem results 71
3.4 NUMERICAL EXAMPLES 73
  3.4.1 Two-dimensional scalar wave propagation problem 75
    3.4.1.1 Spatial and temporal discretization error 77
    3.4.1.2 Wave propagation time step size estimate 81
    3.4.1.3 Computational cost 84
  3.4.2 Scattered waves by an array of rigid circular cylinders 87
  3.4.3 Two-dimensional elastic wave propagation problem 93
  3.4.4 Two-dimensional viscoelastic wave propagation problem 96

CHAPTER 4 CONCLUDING REMARKS 99

APPENDIX 102

BIBLIOGRAPHY 112

List of Figures

2.1: (a) Analytical solution of problem considered; (b) 10×10 mesh of 4-node elements with distortion ratio = 4. 29

2.2: Numerical solutions using (a) the 4-node enriched element and (b) the 9-node enriched element; the distortion ratio =10. 29

2.3: Relative error in L^2 norm using enriched elements. 30

2.4: Analytical solutions for problems considered (a) case 1; (b) case 2. 33

2.5: Solution errors using uniform meshes: (a) case 1, using 80 linear elements of the conventional finite element method; 8 linear enriched elements with cutoff number 2; 4 quadratic enriched elements with cutoff number 3; (b) case 2, using 320 linear elements of the conventional finite element method; 20 linear enriched elements with cutoff number 3; 16 quadratic enriched elements with cutoff number 3. 33

2.6: Snapshots of displacements at t=0.95s with various cutoff numbers. 35

2.7: Displacement variations along the x-axis at two times. 36

2.8: Study of solution accuracy at time t=0.95s; (a) Relative errors in L^2 norm for various cutoff numbers and values of α, the solution using α=0.0 and is used as the solution to compare with; (b) Comparison of the numerical solutions obtained using α=0.0 and α=0.00001. 37

2.9: Solution of impact of a bar at time t=0.00005s using uniform meshes; (a) Elastic bar considered; (b) Velocity distribution calculated using 100 traditional linear elements; (c) Solution using 700 traditional linear elements (d) Solutions using 50 linear enriched elements with cutoff numbers 0 ,1 ,5; (e) Solutions using the cutoff number 5 with 10 ,50 ,100 linear enriched elements. 39

2.10: Wave profiles at time t=0.72s showing the Rayleigh, P and S waves in Lamb's problem. Point A indicates the applied force position, and R640 and R1280 indicate the positions of the receivers. 41

2.11: Time history of displacement variations in x-direction and y-direction at the two receivers, numerical versus analytical results. 42

2.12: Solution of pressure wave (a) the analytical pressure, A is at (x_0, y_0)=(0.5,0); (b) mesh of 9-node elements used including the perfectly matched layer. 45

2.13: Numerical solutions including the perfectly matched layer, and relative error in L^2 norm not including the perfectly matched layer as a function of the cutoff number. 46

3.1: General problem domain V with domain boundary $S = S_u \cup S_f$ 48

3.2: One-dimensional interpolation functions for an interior node for cutoff number p=2

$h_{I1} = \varphi_I^0(\underline{x}), h_{I2} = h_{I1}\cos(\frac{2\pi}{\Lambda_x}x), h_{I3} = h_{I1}\sin(\frac{2\pi}{\Lambda_x}x), h_{I4} = h_{I1}\cos(\frac{2\pi}{\Lambda_x}2x), h_{I5} = h_{I1}\sin(\frac{2\pi}{\Lambda_x}2x)$ 52

3.3: Schematic of the generalized Maxwell body for (a) the complex viscoelastic bulk modulus and (b) the complex viscoelastic shear modulus. 58

3.4: Integration points on interior disk (a) and lens-shaped region of overlap (b) for piecewise Gauss-Legendre quadrature rule. 64

3.5: Integration points on boundary sectors (a) and lens-shaped region of overlap (b) for piecewise Gauss-Legendre quadrature rule. 65

3.6: Cantilever plate problem. 67

3.7: (a) Discretization of the finite element domain with Lagrange shape function for a middle node and (b) discretization of the finite sphere domain with internal disk shape function. 68

3.8: Strain energy convergence for the piecewise Gauss-Legendre quadrature rule. 69

3.9: Strain energy convergence with decrease in element size for the finite element method and decrease in radius of support for the method of finite spheres. 70

3.10: Finite element results of (a) y-displacement and (b) z-displacement and method of finite spheres results of (c) y-displacement and (d) z-displacement. 72

3.11: Vertical deflection of the neutral axis for the 50×50 FE 9-node mesh and the 9×9 MFS discretization. 73

3.12: Displacement variations at time 0.95s for (a) 33×33 spheres with cutoff number 1, (b) 17×17 spheres with cutoff number 2, (c) 9×9 spheres with cutoff number 3, and (d) a comparison between analytical solution and numerical solutions for response along x-axis. 76

3.13: (a) h-convergence and (b) p-convergence behavior of the method of finite spheres at time 0.95s. 78

3.14: Displacement variations at time 0.95s for (a) 5×5 spheres with cutoff number 3 and (b) a comparison between analytical and numerical solution for response along x-axis. 79

3.15: Displacement variations along x-axis at time 0.95s for 9×9 spheres and cutoff number 3. Comparison between analytical and numerical solutions with (a) Δt=0.003125s and Δt=0.00625s and (b) Δt=0.0125s and Δt=0.025s. 80

3.16: (a) Percentage relative error in the L^2 norm for increasing n. Comparison between analytical and numerical solutions for 17×17 spheres with cutoff number 2 for (b) n=10 and (c) n=12. 82

3.17: (a) 80×80 mesh of 4-node elements with distortion ratio = 10 and (b) Relative error in L^2 norm for the finite element method. 86

3.18: (a) Problem description and (b) discretization of the computational domain. 21×21 spheres are arranged regularly and the spheres whose centers are located inside the circular cylinder have been removed. The computational domain is edged with a perfectly matched layer to model the radiation boundary condition. 88

3.19: Real part of numerical solution with (a) cutoff number 1, (b) cutoff number 2, (c) cutoff number 3, and (d) percentage relative error in the L^2 norm as a function of the cutoff number. 90

3.20: (a) Problem description and (b) discretization of the computational domain. 37×37 spheres are arranged regularly and the spheres whose centers are located inside the circular cylinders have been removed. The computational domain is edged with a perfectly matched layer to model the radiation boundary condition. 91

3.21: Real part of numerical solution with (a) cutoff number 1, (b) cutoff number 2, (c) cutoff number 3, and (d) percentage relative error in the L^2 norm as a function of the cutoff number. 92

3.22: Displacement field at time t=0.74s. 94

3.23: Displacement variations in x-direction and y-direction at the two receivers. Numerical solutions are compared with analytical solutions (a) at 640m from the source and (b) at 1280m from the source. 95

3.24: Determination of quality factors using generalized Maxwell model: (a) Q_p=26 and (b) Q_s=19 as a function of relaxation mechanics. 97

3.25: Displacement distributions in viscoelastic body at (a) t=0.22s and (b) t=0.32s due to a vertical force. 98

3.26: Displacement variations at $x = y =$ 1500m compared with analytical solutions in (a) x-direction and (b) y-direction. 98

List of Tables

2.1: Condition number of coefficient matrix (largest eigenvalue/ smallest eigenvalue [6]) for various cutoff numbers and values of α using the 8×8 mesh of 4-node enriched elements. 37

3.1: Computational times (in seconds) measured for the enriched method of finite spheres. 84

3.2: Computational times (in seconds) measured for the finite element method. . 85

Chapter 1

Introduction

1.1 Overview

The *finite element method* is known to be an effective numerical tool for the solution of boundary value problems on complex domains [6]. However, the standard *finite element method* is not very effective for the solution of wave propagation problems [6 – 8]. The errors introduced in wave propagation analyses using the piecewise polynomial approximations of standard techniques have been identified and analyzed, see e.g. [9 - 10]. In the case of time harmonic wave solutions, it is well-known that the accuracy of the numerical solution becomes rapidly worse with increasing wave number [6, 11 - 14]. Therefore, for problems with short waves, very fine meshes are required to obtain reasonable solutions, so fine, that the numerical solution effort may be prohibitive. In the case of transient wave propagations, the solution may exhibit spurious oscillations, related to the Gibb's phenomenon, and the numerical wave propagation velocity may be significantly different from the physical velocity, due to the numerical period elongation and amplitude decay [6, 15] resulting in the dispersion and dissipation errors [15 – 27]. When a wave travels long distances, the errors become large and the numerical solution is very inaccurate. Therefore, whenever high-frequency components are present in the loading, significant errors are present in the numerical solution unless the mesh is fine enough to model the rapid spatial variations.

In addition, in the implementation of the *finite element method* sometimes complications arise with regard to constructing a good quality mesh [28]. Consequences of a poorly constructed mesh include the loss of accuracy and reliability in the finite element solution. For the solution of wave propagation problems, an unstructured mesh causes the wavefront of a physical wave to distort resulting in the computed wave behaving as if it propagates in an anisotropic domain even though the physical domain is actually isotropic. A large solution error may occur because of one badly distorted element [11]. Furthermore, the process of constructing a good quality mesh is time consuming.

A considerable amount of research has been focused on the development of the *finite element method* for wave propagation problems. For time harmonic wave problems, the *partition of unity finite element method* has been proposed for the solution of Helmholtz problems at high frequencies [29 – 32]. An important point is that in this method specific wave propagation solutions are incorporated into the solution space. However, when solving practical wave propagation problems, we frequently do not know a priori what waves and travels need to be predicted. In fact, the solution is a sum of unknown waves and propagations, and may also include wave conversions. Therefore, embedding *general* multiple wave patterns, like we propose in this thesis, into the solution space seems to be a more natural way of capturing the unknown wave solutions.

The *spectral method*, see Ref. [33], the *spectral element method*, see Refs. [34 – 41] and the *spectral finite element method*, see Refs. [42 - 45] and each time the references therein, have also been developed to solve wave propagation problems. Considering the literature, it is sometimes difficult to see whether a method belongs to one or another of these categories. However, in all cases higher-order polynomials or harmonic functions are used in the solution space.

The *spectral method* can be used to obtain numerical solutions very close to exact solutions because harmonic functions are used as basis functions and the solutions of wave equations are basically harmonic functions. However, the *spectral method* is difficult to use for geometrically complicated domains, as encountered in practice, since the method uses global basis functions. Hence in the analysis of solids and structures, the method has found limited practical use. A natural extension is therefore the *spectral element method*. Here, in essence, high-order Lagrangian-based finite elements are used with special nodal positions and integration schemes that lead to diagonal mass matrices. The method shows low numerical dispersion with respect to standard *finite element methods* and can be very effective in explicit time integration but does not lend itself to modeling complex structures and to the hierarchical increase in the displacement interpolations that we pursue in this thesis.

In addition, the *spectral finite element method* has been developed and is used effectively to solve certain wave propagation problems in that it approximates the solutions with trigonometric polynomials [42 - 45]. However, this method uses a transformation of the governing wave equations to the frequency domain, the solution in the frequency domain, and the back transformation to the time domain. The method is overall an expensive procedure and also difficult to extend to general nonlinear analysis.

A considerable attention has been given to the development of *discontinuous finite element formulations* [46 – 48]. These methods provide much generality for the solution of problems and can in particular be used for wave solutions. However, the methods are, in practice, not sufficiently effective because of the discontinuities between the elements that need to be dealt with, for example, using penalty factors. An extension of these techniques is the *discontinuous enrichment method* in which free-space solutions of the governing problem are used for each element in addition to the polynomial approximations [49, 50]. Hence these methods too do not lend themselves to solve in a uniform and effective manner general linear and nonlinear problems in solid and structural mechanics.

Meshless methods have become increasingly popular and are proving to be supportive procedures for the *finite element method* in addressing the problem of constructing a good quality mesh. Many have been developed for the solution of wave propagation problems. Herein, we will provide a brief description of representative meshless methods, particularly those which seek to analyze wave propagation problems. These include the *element free Galerkin method* (EFG), the *radial basis function method* (RBF), the *meshless local Petrov-Galerkin method* (MLPG), and the *smoothed-particle hydrodynamics method* (SPH).

The *element free Galerkin method* employs the moving least square approximation to construct the shape functions. This method has demonstrated good performance when solving acoustic and elastic wave propagation problems; however, shortcomings also exist. A requirement for using the moving least square approximation is that the weight moment matrix, used to construct shape functions, must be invertible. Furthermore, the shape function in this approximation does not possess the Kronecker delta property unlike the shape functions of the *finite* *element method*, and so imposing the Dirichlet boundary conditions is not as straightforward. In order to impose the essential boundary conditions, the constrained Galerkin weak form with Lagrange multipliers can be used. However, disadvantages arise including a larger system of algebraic equations and the loss of positive definiteness which reduce computational efficiency. An alternative method of enforcing Dirichlet boundary conditions is to use the constrained Galerkin weak form with the penalty method. Using this method does not lead to the disadvantages that arise when using Lagrange multipliers. However, the problem with this method is that it requires selecting appropriate penalty factors that can be applied universally to all kinds of problems [51, 52].

Radial basis functions have been successfully used to solve transient acoustic wave propagation problems [53]. The strong form of the partial differential equation was used in the differential representation of a variable within a local domain. The field variable is spatially approximated by a point interpolation method, and an explicit time marching scheme based on the central difference method is used for time integration. Shape functions are constructed using both multiquadric and Gaussian radial basis functions which warrant a non-singular moment matrix, contrary to polynomial basis functions, but provide less solution accuracy [53 - 55]. A problem with using the *radial basis function method* is choosing a shape parameter which can be applied to a universal set of problems. Shape parameters have to be chosen according to nodal distributions and the number of nodes included for interpolation. Otherwise, the solution accuracy decreases drastically. Thus, for arbitrary nodal distributions, this method is not as stable as the *finite element method* [53].

The *meshless local Petrov-Galerkin method* is a truly meshless method because numerical integration is performed within a local domain so that background cells are not necessary for numerical integration. The method adopts trial functions and test functions from different approximation spaces resulting in various formulations [56 - 59]. In [58], the MLPG is used to solve propagation and scattering of the electromagnetic wave field. Trial functions are constructed using moving least square approximations and tests functions are constructed using the solution of Green's problem. While the method obtains accurate solutions, the main drawback reported is the high computational cost due to numerical integration. The MLPG is also used for the solution of wave propagations in 3D poroelastic solids [59]. Test functions are constructed by using a unit step function and trial functions are constructed using radial basis functions and point interpolation approximations. The numerical solutions obtained are in good agreement with analytical solutions, but it is reported that as the density of nodes increases, the computational cost increases drastically due to numerical integration for the trial functions which are usually complex within the subdomains. Consequently, as seen throughout, high computational cost of numerical integration is the main obstacle preventing meshless methods from being used widely [56 - 59].

Smoothed particle hydrodynamics is a particle method commonly used for simulating fluid flows. However, current research for SPH also shows good results have been obtained for wave propagations in solid materials. The method presents the field quantity in an integral form based on kernel approximations. The kernel approximation functions can be categorized as either Eulerian or Lagrangian and are related to the stability of SPH. Early development of SPH used an Eulerian kernel which exhibited tensile instability due to expressing Lagrangian motion with Eulerian kernel functions. However, the problem with Lagrangian kernel functions is that they become unstable through large deformations since the influence domains are distorted. Two major issues commonly cited for SPH are tensile instability and boundary deficiency [60 - 61]. Tensile instability refers to an unstable solution when tensile stresses are present. Boundary deficiency is a consequence of not satisfying zeroth-order consistency near or on the boundary of the problem domain. Improved versions of the method, which address these issues, have been developed [60 - 61]. The model equations were formulated with stress and velocities as variables [61]. A corrected form of the Lagrangian kernel approximation was used for the spatial discretization [61]. This corrected form enables linear fields to be reproduced exactly, thus overcoming the boundary deficiency issue [61]. For the temporal discretization procedure, a two-step time discretization scheme using Taylor series expansions was proposed. This procedure requires using virtual particles to calculate solutions at intermediate time steps [61]. This method showed good accuracy for the solution to viscoplastic wave propagation problems [61]. However, SPH still requires the use of a large number of nodes in order to obtain reasonably accurate solutions since the approximation of the field variables still depend only on the kernel function. In addition, Randles and Libersky mentioned that, the tensile instability is latent for the problems which involve material strength so that very often the damages in solid continuum models grow much faster than the growth rate of the tensile instability [60]. Lastly, if irregularly distributed particles are used to approximate the solution field, then the order of accuracy becomes less [60].

In order for the meshless methods to be practical engineering alternatives, they must be computationally efficient and reliable. In 2000, De and Bathe introduced the *method of finite spheres* [2 - 5], which is based on the *meshless local Petrov-Galerkin approach.* It is a truly meshless technique where both interpolation and integration can be performed without a mesh. The *method of finite spheres* uses the partition of unity paradigm to construct the approximation functions. Dirichlet boundary conditions can be satisfied effectively when using a special arrangement of the nodes. The *method of finite spheres* is reasonably effective for the solution of boundary value problems on geometrically complex domains [2 - 5]. The potential of the method in solving wave propagation problems will be investigated in this thesis.

1.2 Thesis outline

The outline of this thesis is as follows. In Chapter 2, we provide a generally applicable enriched finite element scheme for the solution of wave propagation problems. The solution field is discretized with the usual Lagrangian functions plus harmonic functions within the elements that provide for additional element behavior and degrees of freedom. In the following, in Section 2.1, we present the governing equations of the elastic wave propagation problems that we consider in this thesis and the new finite element interpolation functions. A practical point is that these functions are formulated to avoid computations in complex arithmetic. We also discuss how to impose the boundary conditions, the use of the interpolations with distorted elements, and the problem of ill-conditioning of the governing algebraic equations. To overcome ill-conditioning, we introduce a simple computational scheme. Then, in Section 2.2, we present the results of a range of numerical tests that illustrate the capabilities of the method. We consider the cases of time harmonic and transient scalar wave equations; the impact of an elastic bar against a rigid wall; a two-dimensional elastic transient wave propagation problem and the solution of a Helmholtz equation around a cylinder, both in infinite domains. For the transient analyses we use an implicit time integration and focus on the capabilities of the spatial discretization. It is seen that the finite element formulation can be used to control the numerical dispersion and dissipation by increasing the element degrees of freedom, and that accurate results can be obtained.

In Chapter 3, we demonstrate the effectiveness of the *method of finite spheres* for the solution of wave propagation problems. In Section 3.1 the formulation of the *method of finite spheres* is outlined as it pertains to the solution of wave propagation problems. Specifically, the global approximation space, defined by the Shepard partition of unity functions multiplied by trigonometric functions, results in efficient and reliable solutions. In Section 3.2, the formulation for two-dimensional elastic and viscoelastic wave propagation problems is introduced. An important discussion of improved numerical integration techniques is given in Section 3.3. A two-dimensional linear elastostatics problem will be used to demonstrate the efficiency and convergence properties of the numerical integration rule that will be used for the wave propagation problems. Section 3.4 illustrates the solutions to various complex wave propagation problems which show the effectiveness of the *method of finite spheres*.

Finally, in Chapter 4 we present the conclusions.

Chapter 2

A finite element method enriched for wave propagation problems

The objective of this Chapter is to extend the specific procedure of Ref. [1] to solve multi-dimensional wave propagation problems. We provide a generally applicable enriched finite element scheme. The solution field is discretized with the usual Lagrangian functions times harmonic functions within the elements that provide for additional element behavior and degrees of freedom.

2.1 Formulation of the method

In this Section we first present the governing equations of the physical problems considered, then the finite element procedure, and thereafter some important attributes of the solution technique.

2.1.1 Governing continuum mechanics equations

We consider an elastic, isotropic, homogeneous medium, V, occupying a domain in $\mathbb{R}^3$. The boundary of V is denoted by S. In order to model an unbounded domain, a "model boundary condition" is used on S_{ext}. The displacement is denoted by $\underline{u}(\underline{x},t)$ where $\underline{x} \in V$.

For isotropic elastic wave propagations, the equations of motion are

$$\rho\underline{\ddot{u}} = \nabla \cdot \underline{\tau}(\underline{u}) + \underline{f}^B \qquad (2.1)$$

where ρ is the mass density, $\underline{f}^B$ is the body force vector, and $\underline{\tau}(\underline{u})$ is the stress tensor [6].

The equations of motion are completed with appropriate boundary conditions. As is usual, we split the boundary S into two parts S_u and S_f with the boundary conditions

$$\underline{u} = \underline{u}^{S_u} \qquad \text{on } S_u \text{ (Dirichlet boundary)} \qquad (2.2)$$

$$\underline{\tau}(\underline{u}) \cdot \underline{n} = \underline{f}^{S_f} \qquad \text{on } S_f \text{ (Neumann boundary)} \qquad (2.3)$$

Here $\underline{u}^{S_u}$ is the prescribed displacement, $\underline{n}$ is an outward unit normal vector on S_f, and $\underline{f}^{S_f}$ is the imposed boundary traction vector.

Included in S_f is the boundary, S_{ext}, used to model an unbounded domain, on which we use

$$\underline{f}^{S_f} = -c_L \rho [\underline{v} \cdot \underline{n}] \underline{n} - c_T \rho \underline{v}_T \tag{2.4}$$

Here $\underline{v}_T = \underline{v} - [\underline{v} \cdot \underline{n}] \underline{n}$ is the velocity tangent to the surface and c_L and c_T are the P and S wave velocities, respectively.

2.1.2 Variational form of the governing continuum mechanics equations

Multiplying Eq. (2.1) by a virtual displacement $\underline{\overline{u}}$ and integrating by parts over V we obtain in the standard way the principle of virtual displacements [6]

$$\int_V \underline{\overline{\varepsilon}}^T \underline{\tau}\, dV + \int_V \rho \underline{\overline{u}}^T \underline{\ddot{u}}\, dV = \int_{S_f} \underline{\overline{u}}^T \underline{f}^{S_f}\, dS + \int_V \underline{\overline{u}}^T \underline{f}^B\, dV \tag{2.5}$$

where $\underline{\overline{u}}$ is the virtual displacement and $\underline{\overline{\varepsilon}}$ is the corresponding virtual strain. The important point is that for the method we propose, the usual standard procedures of finite element analysis are used. Hence, regarding the finite element formulation the only – but important – novelty is the use of the specific interpolation functions given next.

2.1.3 Element interpolation functions

While we next consider the two-dimensional analysis of solids, the basic equations can directly be generalized to plate, shell and three-dimensional solutions. The element interpolation functions for Eq. (2.5) are for two-dimensional analyses given by – considering only one typical solution variable u

$$\begin{aligned} u(r,s) = \textstyle\sum_{\alpha} h_{\alpha}(r,s)[U_{(\alpha,0,0)} + \sum_{k_x=1}^{n} \{\cos(\tfrac{2\pi k_x x}{\Lambda_x}) U^{C}_{(\alpha,k_x,0)} + \sin(\tfrac{2\pi k_x x}{\Lambda_x}) U^{S}_{(\alpha,k_x,0)}\} \\ + \textstyle\sum_{k_y=1}^{m} \{\cos(\tfrac{2\pi k_y y}{\Lambda_y}) U^{C}_{(\alpha,0,k_y)} + \sin(\tfrac{2\pi k_y y}{\Lambda_y}) U^{S}_{(\alpha,0,k_y)}\} \\ + \textstyle\sum_{k_x=1}^{n} \sum_{k_y=1}^{m} \{\cos(\tfrac{2\pi k_x x}{\Lambda_x} + \tfrac{2\pi k_y y}{\Lambda_y}) U^{C+}_{(\alpha,k_x,k_y)} + \sin(\tfrac{2\pi k_x x}{\Lambda_x} + \tfrac{2\pi k_y y}{\Lambda_y}) U^{S+}_{(\alpha,k_x,k_y)} \\ + \cos(\tfrac{2\pi k_x x}{\Lambda_x} - \tfrac{2\pi k_y y}{\Lambda_y}) U^{C-}_{(\alpha,k_x,k_y)} + \sin(\tfrac{2\pi k_x x}{\Lambda_x} - \tfrac{2\pi k_y y}{\Lambda_y}) U^{S-}_{(\alpha,k_x,k_y)}\}] \end{aligned} \qquad (2.6)$$

where the $U_{(\alpha,k_x,k_y)}$ with superscripts are the nodal degrees of freedom; here the S, C and + and – are used in the superscripts to correspond to the harmonic expressions. In one-dimensional solutions, Eq. (2.6) is simply [1]

$$u(r) = \sum_{\alpha} h_{\alpha}(r)[U_{(\alpha,0)} + \textstyle\sum_{k_x=1}^{n} \{\cos(\tfrac{2\pi}{\Lambda_x} k_x x)\, U^{c}_{(\alpha,k_x)} + \sin(\tfrac{2\pi}{\Lambda_x} k_x x)\, U^{s}_{(\alpha,k_x)}\}] \qquad (2.7)$$

In Eq. (2.6), x and y are the coordinates at any point of the element and h_{α} is the conventional finite element interpolation function with α the local node number of the element. Hence for a 4-node element we have α = 1,...,4, and for a 9-node element we have α = 1,...,9. These conventional interpolation functions are enriched by harmonic functions to obtain the actual interpolations used for the displacements. Of course, these interpolation functions can be written using exponentials on the complex plane, but since we consider the solution of solids we mostly use real arithmetic (see Section 2.2.5 for an exception) which can be much more effective.

For the geometry interpolation of the elements, we use the original functions h_{α} in the natural (r,s) space.

In Eq. (2.6), the Λ_x and Λ_y are fundamental wavelengths, and k_x and k_y are integers in the range of $1 \le k_x \le n$, $1 \le k_y \le m$, respectively, where n and m are the cutoff numbers for each term. The analyst needs to choose these data, as part of the finite element model definition, for the problem solution. In our current work, and in all solutions given in Section 2.2, we have so far used $\Lambda_x = 2\Delta x$ and $\Lambda_y = 2\Delta y$, where Δx and Δy are typical element sizes. This choice is physically appropriate and has also some mathematical basis, see Ref. [1].

Considering the integers n and m , values between 1 and 3 are most appropriate as exemplified in Section 2.2. Here we should note that it is not necessary to use $n = m$ but if done, the functions not needed will simply not add additional solution accuracy as it is always the case in finite element analysis.

Of course, the elements used with the interpolation functions in Eq. (2.6) satisfy the rigid-body mode criteria and the patch tests [6].

2.1.4 Imposing boundary conditions

The way we impose boundary conditions is explained in detail in Ref. [1]. Here it is important to note that in this finite element scheme the nodal values $U_{(\alpha,k_x,k_y)}$ contain the effect of the harmonic functions. Hence to exactly satisfy the displacement boundary conditions, we choose the following values

$$U_{(\alpha,k_x,k_y)} = u^{S_u} \quad \text{for } k_x = 0 \text{ and } k_y = 0 \qquad (2.8)$$

$$U_{(\alpha,k_x,k_y)} = 0 \quad \text{for } k_x \neq 0 \text{ or } k_y \neq 0 \qquad (2.9)$$

where u^{S_u} is the prescribed displacement. Therefore we impose the boundary displacements not using the harmonic functions. For the Neumann boundary conditions, the boundary term in the discretized equations is calculated in the same way as in the standard finite element method.

2.1.5 Geometrically distorted elements

To evaluate the coefficient matrices, analytical integration (as used in Ref. [1]) can directly be used as long as the elements are rectangular. If the elements are slightly distorted, a semi-analytical integration may still be possible. However, when the element distortions are significant, numerical integration is probably necessary. In this research we simply used the conventional Gauss-Legendre integration scheme [6]. While we use this scheme it is clear that more efficient techniques are very desirable.

To test the performance of the elements when these are distorted, we solve a simple problem in the domain $[0,1]\times[0,1]$ for which the exact solution is $u(x,y)=\sin(4\pi x)$, see *Fig. 2.1(a)*. *Fig. 2.1(b)* shows a distorted 10×10 mesh using 4-node elements. Here, the distortion ratio is defined as the ratio of the longest side length of any of the elements over the shortest side length of any of the elements in the domain [6].

In the study we use the 10×10 mesh of 4-node elements and a 5×5 mesh of 9-node elements (simply geometrically combining four 4-node elements to one 9-node element) which leads to the same number of total degrees of freedom, and $(n,m)=(2,2)$ for the cutoff numbers. *Fig. 2.2* shows the results obtained using the 4-node and 9-node element meshes. Note that the numerical result using the 9-node enriched element is very similar to the analytical solution even for the largest distortion ratio.

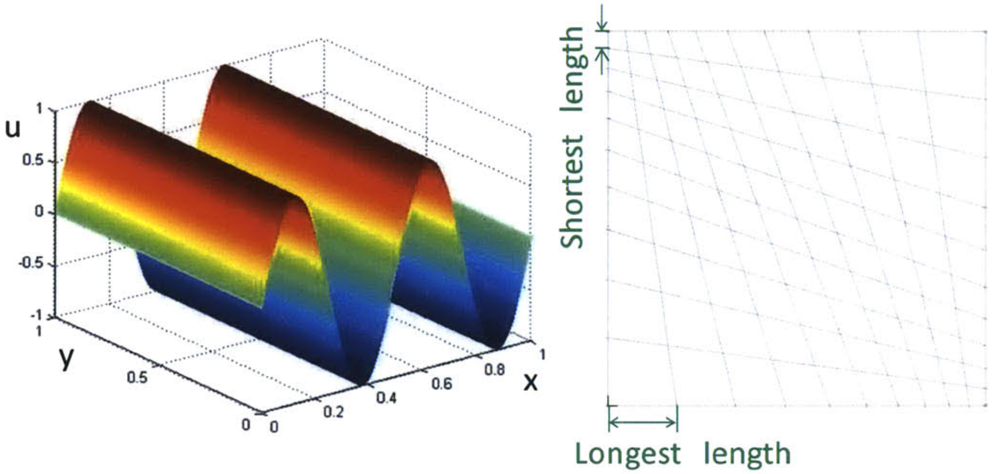

(a) *(b)*

Fig. 2.1: *(a) Analytical solution of problem considered; (b) 10×10 mesh of 4-node elements with distortion ratio = 4.*

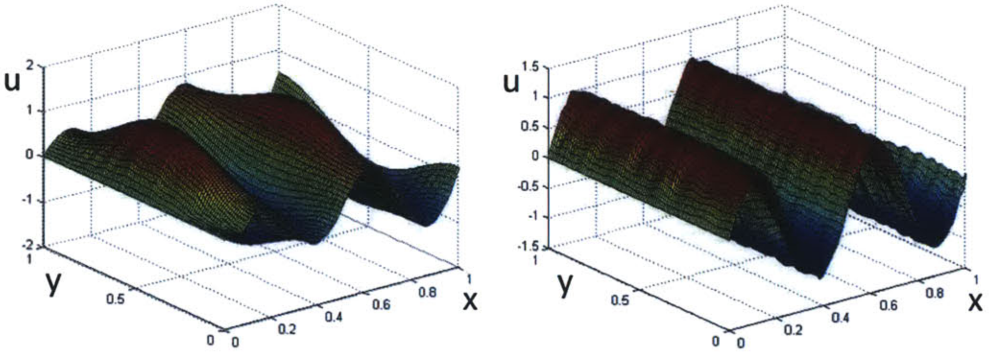

(a) *(b)*

Fig. 2.2: *Numerical solutions using (a) the 4-node enriched element and (b) the 9-node enriched element; the distortion ratio =10.*

Fig. 2.3 shows the relative error in the L^2 norm, in percent, defined as

$$\frac{\sqrt{\int_V |u-u_h|^2 \, dV}}{\sqrt{\int_V |u|^2 \, dV}} \times 100(\%) \qquad (2.10)$$

While the 4-node enriched element is quite sensitive to distortion, the 9-node enriched element is not that sensitive and hence performs much better.

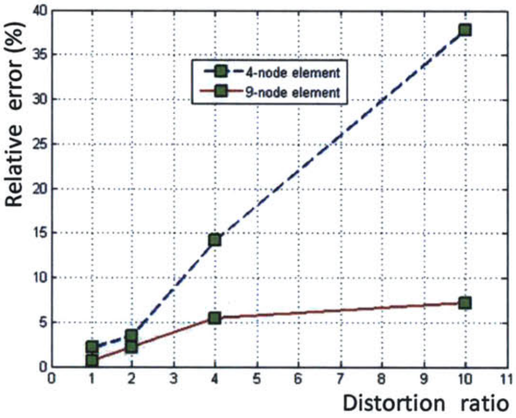

Fig. 2.3: *Relative error in L^2 norm using enriched elements.*

This result can be explained by the loss of predictive capability of the elements due to element geometric distortions, which is discussed in Refs. [6, 62].

2.1.6 A scheme to overcome the (possible) ill-conditioning of the algebraic equations

In earlier research on the partition of unity finite element and generalized finite element methods, it was reported that the resulting interpolation functions can lead to singular matrices or to ill-conditioning of the system of linear equations. The singularity occurs because some interpolation functions are linearly dependent, and the ill-conditioning occurs because the interpolation functions used are "close" to each other. With Eq. (2.6), the functions are linearly independent but do become close to each other as the cutoff numbers become large.

Strouboulis et. al. [63] proposed to change the stiffness matrix slightly, and then iterate in order to annihilate the resulting error. However, our aim is to not iterate and, also, to have a scheme that lends itself to nonlinear analysis, in which exact tangent stiffness matrices change and may become singular (for physical reasons). Hence we change the mass matrix, rather than the stiffness matrix, and use in the time integration on the left-hand side of the algebraic equations

$$\underline{M} = (1-\alpha)\underline{M}_{consistent} + \alpha\underline{M}_{lumped} \tag{2.11}$$

and on the right-hand side of the equations

$$\underline{M} = \underline{M}_{consistent} \tag{2.12}$$

where α is a parameter of very small magnitude, and we calculate the lumped mass matrix $\underline{M}_{lumped}$ using the total mass and allocating the lumped masses in the ratio of the diagonal elements of the consistent mass matrix. Specific results using this scheme are given in Section 2.2.2. Note that the mass matrix in Eq. (2.11) is only used to overcome a possible ill-conditioning of the coefficient matrix and not to reduce artificial dispersion or dissipation.

2.2 Numerical examples

In this Section, we illustrate the performance of the enriched finite element method by solving several wave propagation problems. First, we solve time harmonic and transient scalar wave equations and focus on the numerical dispersion. Then, we use the method to solve for the stress wave in the impact of an elastic bar and focus on the sharpness of the wave front. Third, an elastic wave propagation problem is solved which contains P, S and Rayleigh waves. Finally, we use the method to predict the propagation of an acoustic pressure wave, originating from a circular cylinder, in an infinite domain.

For all transient analyses we use implicit time integration – which is not mostly employed in practical wave analyses. However, using implicit time integration provides a stringent test on the spatial discretization scheme and when employed in practice can be more reliable [6].

2.2.1 Solution of time harmonic scalar wave

For the problem considered, the solution for u is governed by

$$\frac{\partial^2 u}{\partial x^2}+\frac{\partial^2 u}{\partial y^2}+k^2u=0\ ,\ 0\le x\le 2 \text{ and } 0\le y\le 2 \tag{2.13}$$

with the boundary conditions

$$\begin{aligned} &u(0,y)=0,\ \frac{\partial u(x,2)}{\partial y}=0,\ \frac{\partial u(x,0)}{\partial y}=0,\\ &\frac{\partial u(2,y)}{\partial x}=4\pi\left(\text{ and }=8\pi \text{ for case } 2\right) \end{aligned} \tag{2.14}$$

where $k = 8\pi(32\pi)$ in $0 \le x \le 1$ and $k = 4\pi(8\pi)$ in $1 \le x \le 2$ for the case 1(case 2).

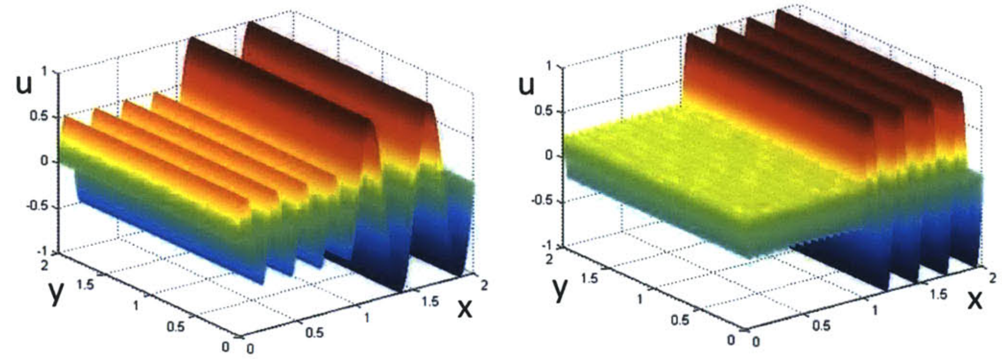

(a) *(b)*

***Fig. 2.4**: Analytical solutions for problems considered (a) case 1; (b) case 2.*

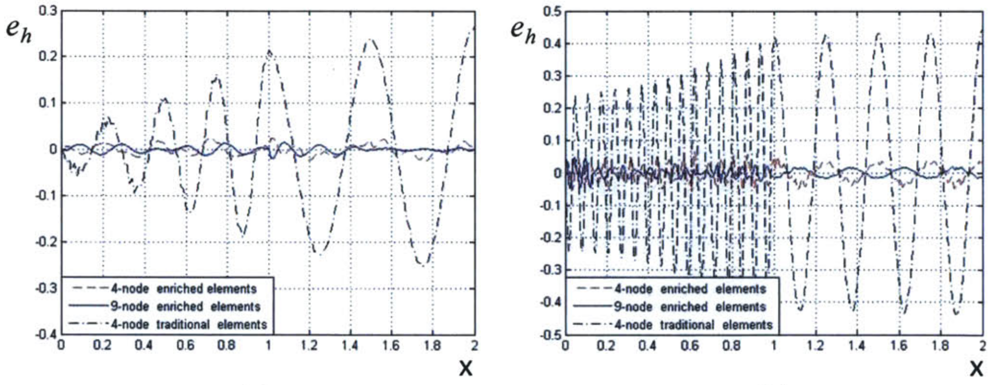

(a) *(b)*

***Fig. 2.5:** Solution errors using uniform meshes: (a) case 1, using 80 linear elements of the conventional finite element method; 8 linear enriched elements with cutoff number 2; 4 quadratic enriched elements with cutoff number 3; (b) case 2, using 320 linear elements of the conventional finite element method; 20 linear enriched elements with cutoff number 3; 16 quadratic enriched elements with cutoff number 3.*

In *Fig. 2.4*, we present the exact solutions of u for both cases. This is, of course, really only a one-dimensional problem but it is a useful problem to study the errors occurring in numerical schemes. In *Fig. 2.5*, we study the error $e_h = u(x,0) - u_h(x,0)$ using equal-sized elements in each solution. The error in the finite element solution is due to the numerical period elongation and amplitude decay, also referred to as numerical dispersion and dissipation. Analyses of these errors are given, for example, in Refs. [6, 11 - 15]. We see that in these cases the 4-node and 9-node enriched elements perform very well.

2.2.2 Solution of transient scalar wave

The scalar wave equation with a Ricker wavelet source at the center of a two-dimensional domain, as considered in Ref. [25], is given by

$$\frac{\partial^2 u}{\partial x^2} + \frac{\partial^2 u}{\partial y^2} + F(0,0,t) = \frac{1}{c^2}\frac{\partial^2 u}{\partial t^2} \qquad (2.15)$$

$$F(0,0,t) = 10\left(1 - 2\pi^2 f^2 (t-0.25)^2\right)\exp\left(-\pi^2 f^2 (t-0.25)^2\right) \qquad (2.16)$$

where u is the displacement solution sought, c is the wave velocity, f is the central frequency and in this example $c = 1$ and $f = 6\text{Hz}$. Only the domain $[0,1]\times[0,1]$ shown in *Fig. 2.6* is used for the finite element solution because of symmetry. While, in general, absorbing boundary conditions should be prescribed at the outer boundary, in this solution no "absorbing" boundary conditions are used because for the time considered 0.95s, the wave does not reach this boundary. With the conventional finite element method, an 80×80 4-node element mesh is employed, leading to 6,561 degrees of freedom. For the enriched method, an 8×8

4-node element mesh with cutoff numbers $(n,m)=(1,1),(2,2),(3,3)$ is used, leading to 729, 2,025, and 3,969 degrees of freedom, respectively. In all solutions, we used the trapezoidal rule of time integration, with a very small time step $\Delta t = 0.00625\text{s}$, which corresponds to a CFL number = 0.5 for the $80{\times}80$ mesh. To assess the accuracy of the solution, we also solved the problem with the $8{\times}8$ mesh of 4-node elements and $(n,m)=(4,4)$ and obtained negligible differences to the response calculated with $(n,m)=(3,3)$, see *Fig. 2.7.*

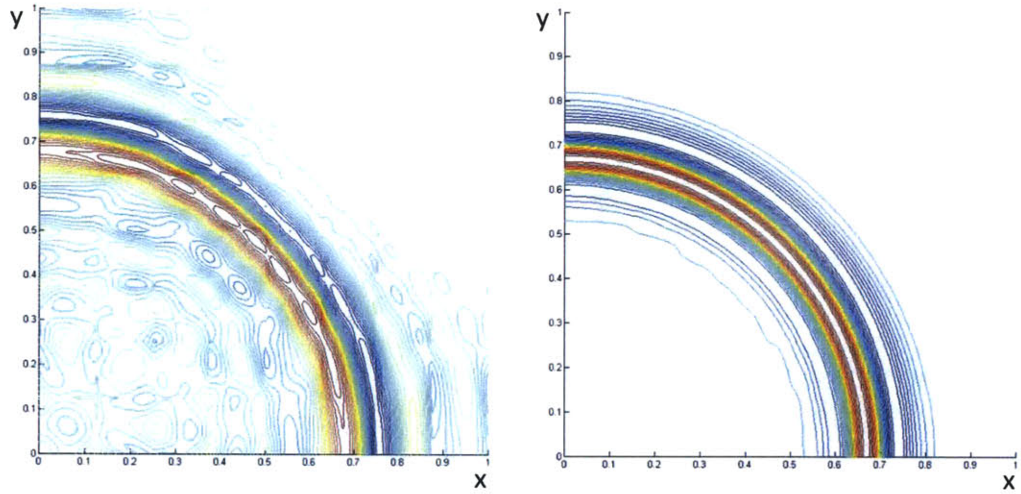

8×8 mesh with cutoff number (a) (n,m)=(1,1) and (b) (n,m)=(2,2)

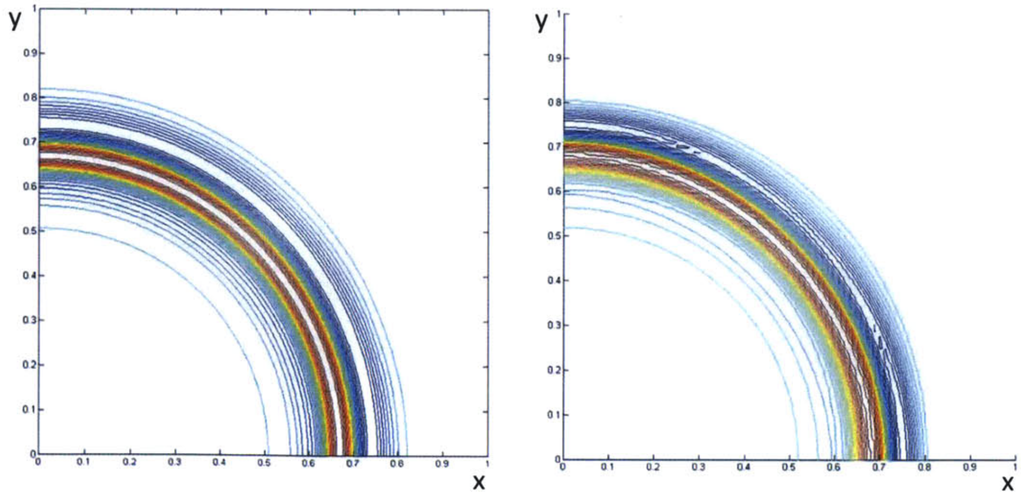

8×8 mesh with cutoff number (c) (n,m)=(3,3) and (d) 80×80 mesh

Fig. 2.6: *Snapshots of displacements at t=0.95s with various cutoff numbers.*

Fig. 2.6 gives snapshots of the displacements at time t=0.95s as calculated using the conventional and enriched methods. As expected, the numerical results of the enriched method exhibit better accuracy as the cutoff number increases. Also, for the meshes used, the conventional method gives results that are not as good as obtained with the enriched method with the cutoff number $(n,m)=(3,3)$. Considering the displacement variations along the x-axis [25], as shown in *Fig. 2.7*, the error in the response prediction increases, using the traditional method, with the distance of wave travel in the computational domain. As well known, even an apparently small error in wave propagation velocity may result into unacceptable displacement and hence stress errors as time increases.

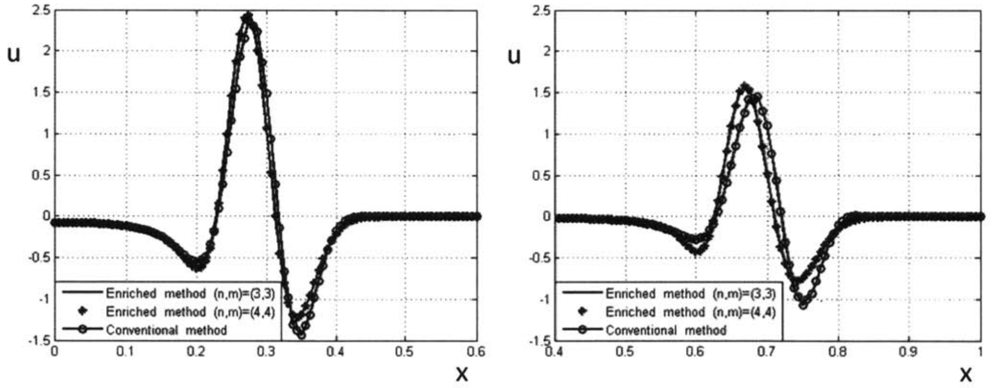

Displacement variations at (a) t=0.55s and (b) t=0.95s

Fig. 2.7: *Displacement variations along the x-axis at two times.*

We obtained the results given above without regard to ill-conditioning of the coefficient matrix. However, as pointed out in Section 2.1.6, using the displacement interpolation functions of Eq. (2.6) can lead to ill-conditioning and indeed in this problem solution, ill-conditioning can be seen when calculating the condition number (although the solution is obtained without numerical difficulties even when $(n,m)=(4,4)$). *Table 2.1* lists the condition number of the coefficient matrix using various cutoff numbers and values of α in Eq. (2.11). *Fig. 2.8* shows the relative solution errors calculated over the domain in the L^2 norm when using different parameters, and also the displacements along the *x*-axis obtained with $(n,m)=(4,4)$. As seen, when using $\alpha=0.00,00,1$ the condition number is much improved while the error due to using this value of α can be neglected.

Table 2.1: *Condition number of coefficient matrix (largest eigenvalue/ smallest eigenvalue [6]) for various cutoff numbers and values of α using the 8×8 mesh of 4-node enriched elements.*

Cutoff number	*Condition number*			
	α=0	*α =0.000001*	*α =0.00001*	*α =0.0001*
(n,m)=(1,1)	5.8E+07	3.6E+07	1.1E+07	1.7E+06
(n,m)=(2,2)	3.4E+10	1.2E+09	1.5E+08	1.7E+07
(n,m)=(3,3)	9.7E+12	4.0E+09	4.0E+08	4.2E+07
(n,m)=(4,4)	2.8E+16	8.1E+09	8.3E+08	7.8E+07

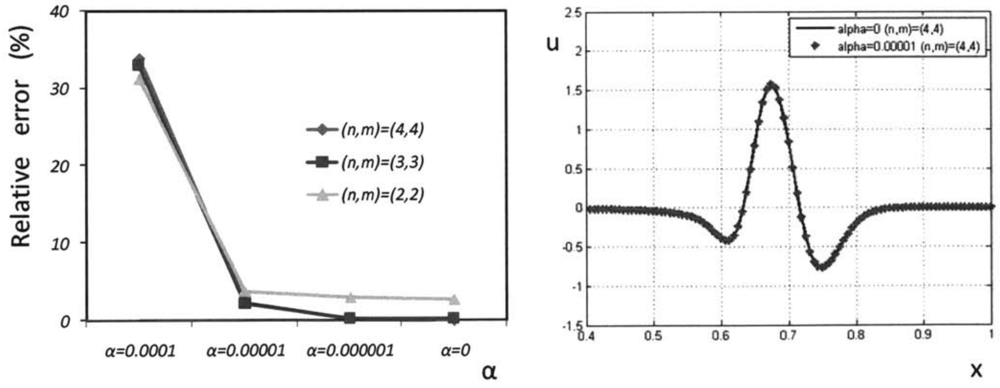

(a) *(b)*

Fig. 2.8: *Study of solution accuracy at time t=0.95s; (a) Relative errors in* L^2 *norm for various cutoff numbers and values of α, the solution using α=0.0 and* $(n,m)=(4,4)$ *is used as the solution to compare with; (b) Comparison of the numerical solutions obtained using α=0.0 and α=0.00001.*

2.2.3 One-dimensional impact of an elastic bar

A good benchmark problem for testing a finite element method for wave propagation solutions is the one-dimensional impact problem shown in *Fig. 2.9* [27].

The problem can, of course, be solved very accurately using explicit time integration, lumped mass matrices, and meshes of 2-node linear elements [6]. To test the proposed formulation, we solve the problem using uniform meshes of linear elements, consistent mass matrices, and in each case, we use the trapezoidal rule of time integration with the very small time step $\Delta t = 2.5\times10^{-8}\,\mathrm{s}$.

Fig. 2.9 gives the results obtained. As well known, using the traditional finite element discretizations, spurious oscillations in the stress and velocity predictions are obtained. These oscillations are somewhat reduced using the time integration method proposed by Bathe [64] but are still present. As seen in the figure, when we use the enriched finite element method, we can control the spurious high-frequency oscillations and make them acceptably small. As mentioned already, we used the consistent mass matrix, although in certain analyses, using a lumped mass matrix or a combination of lumped and consistent mass matrices might reduce the errors [65].

2.2.4 Solution of two-dimensional P, S and Rayleigh waves

In this Section, we solve the Lamb problem of elastic waves propagating inside a semi-infinite domain due to an imposed surface vertical force [66], as considered in Refs. [35, 36].

From Eq. (2.5), the finite element formulation gives for an element [6]

$$\begin{aligned}\int_{V^{(m)}} \underline{H}^{(m)T} \begin{bmatrix} \rho & 0 \\ 0 & \rho \end{bmatrix} \underline{H}^{(m)}\, dV^{(m)}\, \underline{\ddot{U}} + \int_{S_{ext}^{(m)}} \underline{H}^{(m)T} \begin{bmatrix} \rho c_L & 0 \\ 0 & \rho c_T \end{bmatrix} \underline{H}^{(m)}\, dS^{(m)}\, \underline{\dot{U}} \\ + \int_{V^{(m)}} \underline{B}^{(m)T} \underline{C}^{(m)} \underline{B}^{(m)} dV^{(m)}\, \underline{U} = \int_{S_f^{(m)}} \underline{H}^{(m)T} \underline{f}^{S_f(m)}\, dS^{(m)}\end{aligned} \qquad (2.17)$$

where $\underline{H}^{(m)}$ is the displacement interpolation matrix obtained from Eq. (2.6), $\underline{B}^{(m)}$ is the corresponding strain-displacement matrix, and $\underline{C}^{(m)}$ is the constitutive matrix for the plane strain condition used. Note that the boundary condition to model the infinite domain, Eq. (2.4) for S_{ext}, results into the velocity dependent term in Eq. (2.17).

The isotropic semi-infinite elastic medium has a P-wave velocity $3200\,\mathrm{m/s}$, an S-wave velocity $1847.5\,\mathrm{m/s}$, a mass density $2200\,\mathrm{kg/m^3}$, and is modeled as a domain of size $4000\times2000\mathrm{m}^2$ in plane strain conditions, see *Fig. 2.10*. The force, a Ricker wavelet with a central frequency of 14.5 Hz, is applied on the free surface at $(x_A, y_A) = (2000\,\mathrm{m}, 2000\,\mathrm{m})$. Two receivers are located at 640m and 1280m from the applied force. For the numerical solution, we use a mesh of 50×25 4-node enriched elements, with $(n,m)=(2,2)$ leading to a total of 66,300 degrees of freedom, a consistent mass matrix, and the trapezoidal rule of time integration with a time step 0.0008s. The total time of response to be calculated is 1s; hence the P wave will reach the outer boundary during the solution time.

Fig. 2.10 shows the wave profiles at time 0.72s, a strong Rayleigh wave along the surface and the P and S waves inside the domain. *Fig. 2.11* gives the numerical prediction at the two receivers, which is in reasonable agreement with the analytical solution. Note that in the finite element solution presented here, we did not incorporate any knowledge of the two waves a priori – this response was naturally solved for by use of our displacement interpolation functions, see Eq. (2.6). These displacement functions can naturally represent many different waveforms and will automatically solve for the actual wave response.

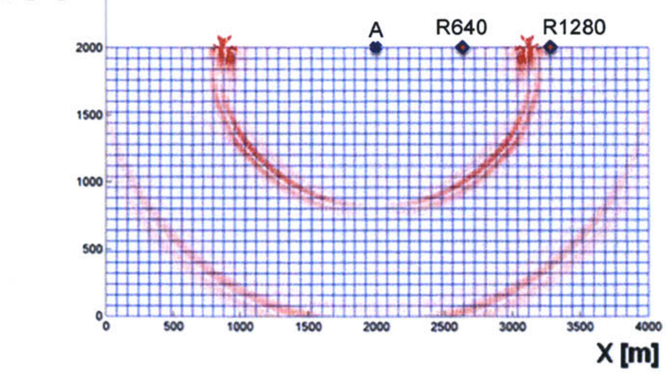

***Fig. 2.10**: Wave profiles at time 0.72s showing the Rayleigh, P and S waves in Lamb's problem. Point A indicates the applied force position, and R640 and R1280 indicate the positions of the receivers*

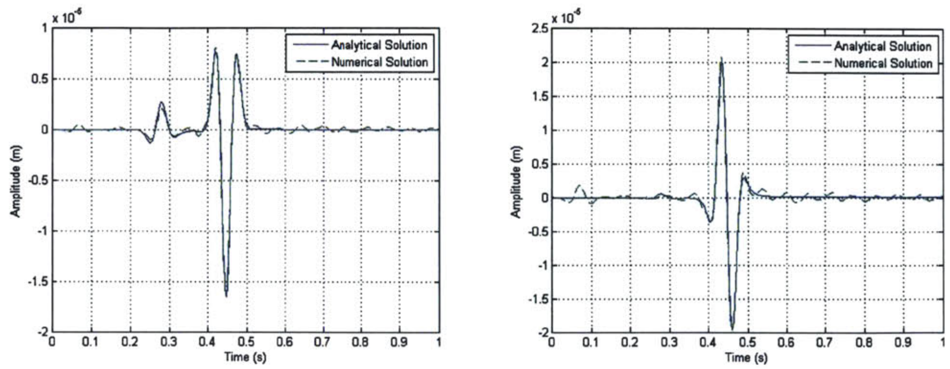

(a) Displacements at 640m from the source in x-direction and y-direction

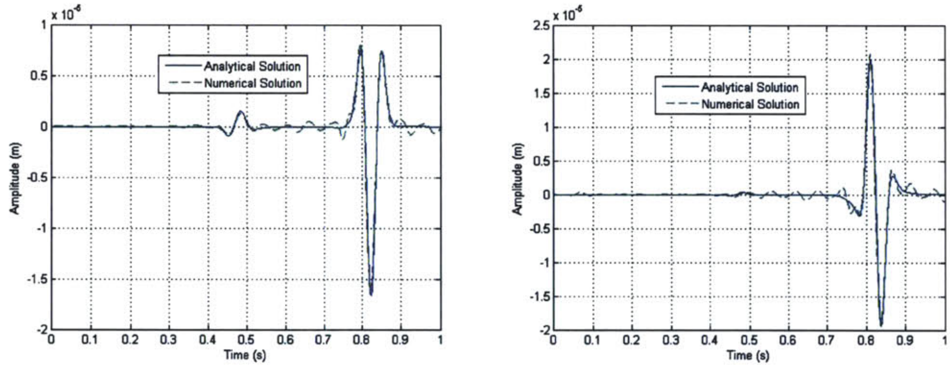

(b) Displacements at 1280m from the source in x-direction and y-direction

Fig. 2.11: *Time history of displacement variations in x-direction and y-direction at the two receivers, numerical versus analytical results.*

2.2.5 Solution of time harmonic acoustic pressure wave

Consider an inviscid fluid for which we define the velocity potential ϕ with

$$\underline{v} = \nabla\phi; \quad p = -\rho\dot{\phi} \tag{2.18}$$

where $\underline{v}$ is the velocity and p is the pressure [6]. The equation governing the pressure behavior is

$$\nabla^2 p = \frac{1}{c^2}\frac{\partial^2 p}{\partial t^2} \qquad (2.19)$$

with the wave speed $c=\sqrt{\beta/\rho}$ where β is the bulk modulus and ρ is the density of the fluid. Focusing on the propagation of a two-dimensional acoustic pressure wave at a single frequency, the time dependent pressure p can be written as [67 - 69]

$$p(x,y,t)=\mathrm{Re}\left[P(x,y)e^{-i\omega t}\right] \qquad (2.20)$$

Substituting from Eq. (2.20) into Eq. (2.19) we obtain the Helmholtz equation for the time harmonic pressure P. For the numerical test, we consider a circular cylinder with boundary S_f placed in the unbounded domain V (see *Fig. 2.12*). Our goal is to solve the Helmholtz problem like in Ref. [70]:

$$\begin{aligned} &\nabla^2 P + k^2 P = 0 && \text{in } V, \\ &\frac{\partial P}{\partial n} = g(x,y) && \text{on } S_f, \\ &\lim_{r\to\infty}\sqrt{r}\left(\frac{\partial P}{\partial r} - ikP\right) = 0. && \end{aligned} \qquad (2.21)$$

where $k=\omega/c$ and r is the distance from the origin in the Cartesian coordinates (*Fig. 2.12*).

Considering this problem, the Hankel function of the first kind satisfies the first and third equations

$$P(x,y)=\frac{i}{4}H_0^{(1)}\left(k\sqrt{(x-x_0)^2+(y-y_0)^2}\right) \qquad (2.22)$$

Hence using this function to prescribe $g = \partial P/\partial n$ on the boundary S_f, Eq. (2.22) is the exact solution for the Helmholtz problem in Eq. (2.21). Using $x_0 = 0.5$, $y_0 = 0$, the radius of the circular cylinder = 1, like in Ref. [70], and $k = 22.06$, *Fig. 2.12(a)* shows the analytical solution of the pressure.

In the finite element solution we prescribe the boundary condition $g = \partial P/\partial n$ on the cylindrical boundary S_f and calculate the pressure response in the computational domain.

To model the infinity of the physical domain, we use the perfectly matched layer of Ref. [70] with the recommended parameters. This layer truncates the unbounded domain in the numerical calculation by the following equations

$$\frac{1}{\gamma_1}\frac{\partial}{\partial x}\left(\frac{1}{\gamma_1}\frac{\partial P}{\partial x}\right)+\frac{1}{\gamma_2}\frac{\partial}{\partial y}\left(\frac{1}{\gamma_2}\frac{\partial P}{\partial y}\right)+k^2 P=0 \qquad (2.23)$$

where

$$\gamma_1=\begin{cases}1 & \text{for } |x|<2\\ 1+\dfrac{i}{k(3-|x|)} & \text{for } 2\le|x|\le 3\end{cases} \text{ and}$$

$$\gamma_2=\begin{cases}1 & \text{for } |y|<2\\ 1+\dfrac{i}{k(3-|y|)} & \text{for } 2\le|y|\le 3\end{cases} \qquad (2.24)$$

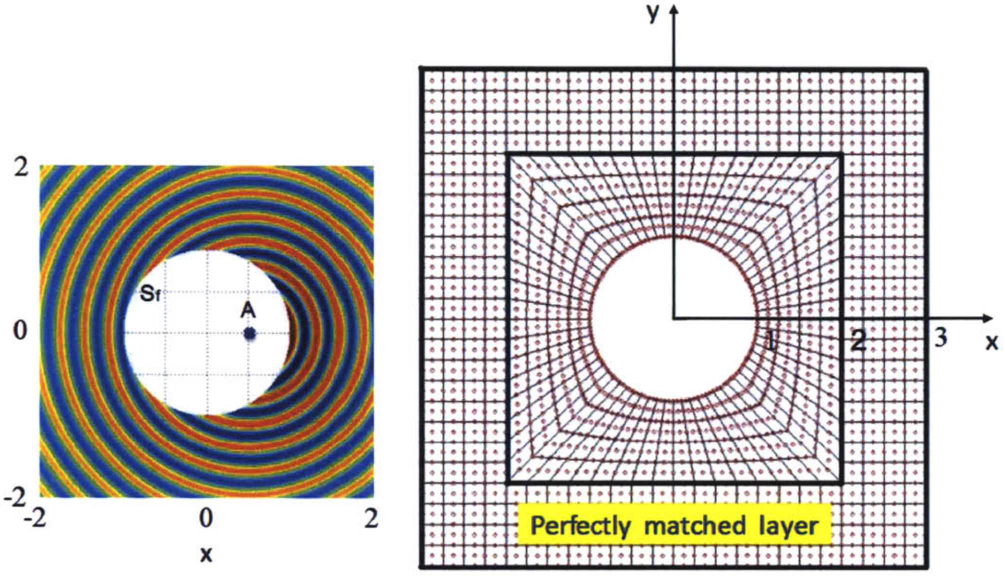

(a) *(b)*

***Fig. 2.12**: Solution of pressure wave (a) the analytical pressure, A is at* $(x_0, y_0)=(0.5,0)$; *(b) mesh of 9-node elements used including the perfectly matched layer.*

Fig. 2.12(b) shows the complete finite element domain meshed with 9-node elements, giving a total of 576 degrees of freedom when $(n,m)=(0,0)$.

Fig. 2.13 gives contour plots of the pressure numerical solutions using the cutoff numbers from 0 to 2, where the result obtained using the cutoff numbers $(n,m)=(2,2)$ is in good agreement with the analytical solution.

As expected, the relative error in the L^2 norm decreases as the cutoff number increases, see *Fig. 2.13*, and only a few harmonic functions need to be included to obtain sufficiently accurate results. If the numerical solution for a higher wave number k were to be obtained, it would be necessary to either increase the number of elements or the cutoff number in order to have the same level of solution accuracy.

We note that while in all previous solutions, we only used real arithmetic, in this example solution, we employed complex arithmetic for the perfectly matched layer in the discretized domain.

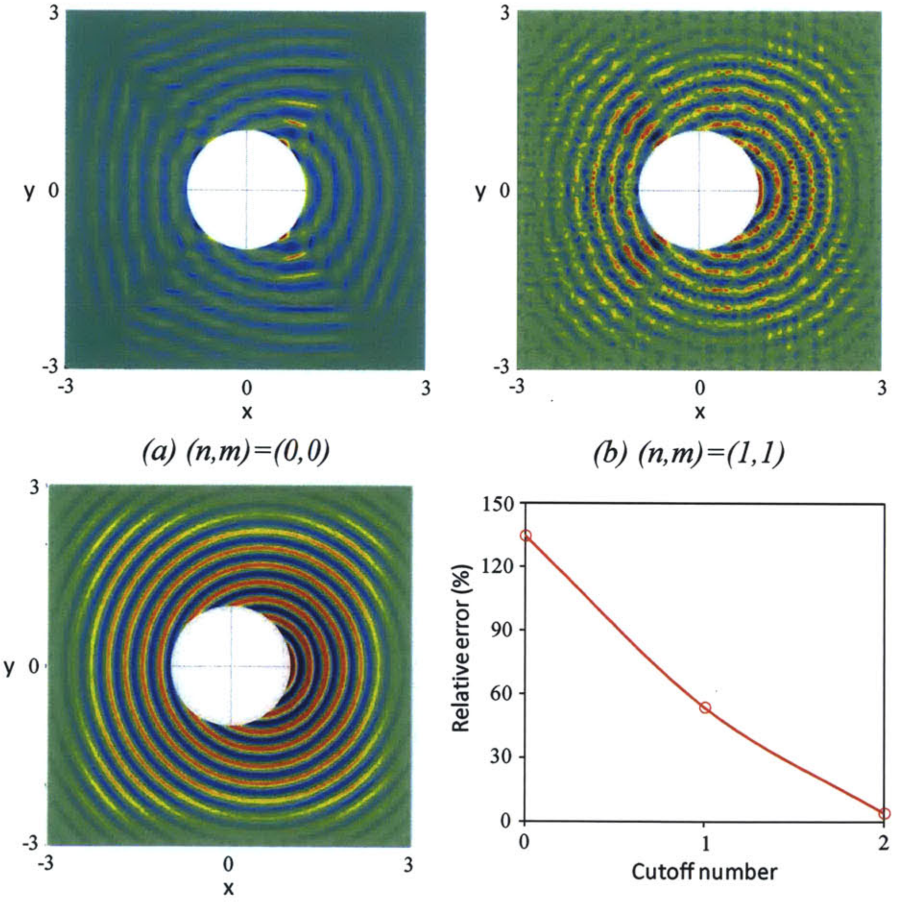

(a) (n,m)=(0,0) *(b) (n,m)=(1,1)*

(c) (n,m)=(2,2) *(d) Relative error in L^2 norm*

Fig. 2.13: *Numerical solutions including the perfectly matched layer, and relative error in L^2 norm not including the perfectly matched layer as a function of the cutoff number.*

Chapter 3

The method of finite spheres enriched for wave propagation problems

The objective of this Chapter is to demonstrate the effectiveness of the method of finite spheres for the solution of wave propagation problems. An effective numerical integration scheme is introduced which improves the computational efficiency of the method. Several examples of wave propagation are used to illustrate the advantages of the method of finite spheres.

3.1 Method of finite spheres interpolation functions

The objective in developing the method of finite spheres is to obtain an efficient and reliable method to solve complex boundary value problems without the construction of a mesh. The selection of efficient and reliable interpolation functions used for the solution of wave propagation problems will be presented here.

3.1.1 The partition of unity functions

The method of finite spheres is based on the Shepard partition of unity functions [2 - 5]. These functions are nonpolynomial and have zeroth-order consistency. The nonpolynomial nature of these functions poses a challenge for numerical integration, which will be addressed in Section 3.3. Zeroth-order consistency ensures rigid body modes can be reproduced exactly.

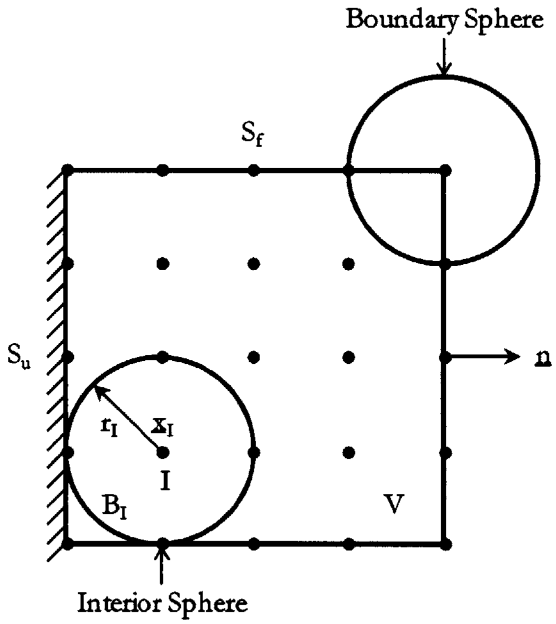

Fig. 3.1: General problem domain V with domain boundary $S = S_u \cup S_f$.

Let $V \in R^d$ $(d = 1,\ 2, \text{or } 3)$ be the computational problem domain. Let S be the boundary of the domain, where $S = S_u \cup S_f$ and $S_u \cap S_f = 0$, with S_f being the Neumann boundary and S_u being the Dirichlet boundary. Then

$\{B(\underline{x}_I, r_I);\ I = 1,\ 2, \ldots,\ N\}$ is a set of spheres which form a covering for V, i.e., $V \subset \bigcup_{I=1}^{N} B(\underline{x}_I, r_I)$, where $\underline{x}_I$ and r_I refer to the center and radius of the sphere, B_I, respectively, and where I is the 'node' number of each sphere and N is the total number of spheres. The unit normal, $\underline{n}$, is defined as positive in the outward direction to the domain boundary. The spheres are categorized as either an interior sphere, a sphere which is entirely within the problem domain, or a boundary sphere, a sphere with nonzero intercept with the domain boundary, as shown in *Fig. 3.1.*

Let $W_I(\underline{x})$ denote a weight function. Then the Shepard partition of unity functions are defined as

$$\varphi_I^0(\underline{x}) = \frac{W_I}{\sum_{J=1}^{N} W_J}, \qquad I=1,2,\ldots,N \qquad (3.1)$$

with the following requirements:

$$\sum_{I=1}^{N} \varphi_I^0(\underline{x}) = 1 \quad \forall \underline{x} \in V \qquad (3.2)$$

$$\text{supp}(\varphi_I^0(\underline{x})) \subset B(\underline{x}_I, r_I) \qquad (3.3)$$

The selection of the weight functions should consider the continuity class to which they belong as well as how easily they can be differentiated and integrated. The quartic spline weight functions are used since they provide a low cost partition of unity. The quartic spline weight functions are

$$W_I(\underline{x}) = W_I(s) = \begin{cases} 1 - 6s^2 + 8s^3 - 3s^4, & 0 \le s \le 1 \\ 0, & s > 1 \end{cases} \qquad (3.4)$$

where $s = |\underline{x} - \underline{x}_I| / r_I$.

3.1.2 The interpolation functions for wave propagation

In the method of finite spheres, the interpolation functions are easily modified for various problems. The interpolation functions within each sphere are generated by multiplying the Shepard partition of unity functions with local approximation functions. It is the choice of the local approximation functions that makes the method of finite spheres a powerful computational tool because any function included in the local bases can be exactly reproduced. A suitable approximation space for wave propagation problems is based on trigonometric functions.

As mentioned above, the Shepard partition of unity functions satisfy zeroth-order consistency. For higher order consistency, a local approximation space $V_I^h = \mathrm{span}_{m\in\Im}\{p_m(\underline{x})\}$ is defined at each node I, where $p_m(\underline{x})$ is a function in V_I^h, $\Im$ is an index set, and h is a measure of the size of the sphere. Then, the global approximation space V_h is generated by multiplying the Shepard partition of unity functions with the functions from the local basis

$$V_h = \sum_{I=1}^{N} \varphi_I^0 V_I^h \tag{3.5}$$

For two-dimensional wave propagation problems, the local approximation space is defined as

$$\begin{aligned} V_I^h = \mathrm{span}\{&1, \cos(\frac{2\pi k_x x}{\Lambda_x}), \sin(\frac{2\pi k_x x}{\Lambda_x}), \cos(\frac{2\pi k_y y}{\Lambda_y}), \sin(\frac{2\pi k_y y}{\Lambda_y}), \\ &\cos(\frac{2\pi k_x x}{\Lambda_x} + \frac{2\pi k_y y}{\Lambda_y}), \sin(\frac{2\pi k_x x}{\Lambda_x} + \frac{2\pi k_y y}{\Lambda_y}), \\ &\cos(\frac{2\pi k_x x}{\Lambda_x} - \frac{2\pi k_y y}{\Lambda_y}), \sin(\frac{2\pi k_x x}{\Lambda_x} - \frac{2\pi k_y y}{\Lambda_y}), k_x, k_y = p\}, p \in \{1,2,3\} \end{aligned} \tag{3.6}$$

where Λ_x and Λ_y are fundamental wavelengths in the x and y directions, respectively, and p is the cutoff number. A suitable choice for the fundamental wavelengths to be used throughout the thesis is $\Lambda_x = \Lambda_y = 2r_I$ [71]. Higher order trigonometric functions are included in the local approximation space as the cutoff number increases. As additional higher order terms are included, the condition number of the constructed matrices increases. Due to the fact that increasingly higher order terms become less significant for approximating solutions, an upper bound of p=3 has been selected in this thesis for two-dimensional wave propagation problems.

A patch test was performed for two-dimensional linear elasticity problems [6] using the above local approximation space. Although the interpolation functions do not include the bilinear functions, the patch test is passed with reasonable accuracy using regularly spaced and same radii spheres. This is because using a finite number of terms of a Fourier series can approximate not exactly but very closely the polynomial functions that are needed to reproduce the three constant stress states. More investigations on the patch test using irregularly spaced and different radii spheres are required, but in this thesis only regularly spaced and same radii spheres are used even for a problem with a complicated geometry (see Section 3.4.2). Also, see ref. [86] where the bilinear functions have been included.

Any function $v_h \in V_h$ can be approximated by

$$v_h(\underline{x}) = \sum_{I=1}^{N} \sum_{m \in \Im} h_{Im}(\underline{x}) \alpha_{Im} \qquad (3.7)$$

where α_{Im} denotes the nodal unknowns at node I corresponding to the mth degree of freedom and $h_{Im}(\underline{x})$ is the interpolation function,

$$h_{Im}(\underline{x}) = \varphi_I^0(\underline{x}) p_m(\underline{x}) \qquad (3.8)$$

Fig. 3.2 shows the one-dimensional interpolation functions for an interior node for cutoff number $p = 2$. Here, it is important to question whether the interpolation functions based on the trigonometric functions are effective in approximating the solution of wave propagation problems. In order to answer this question, we refer to the mathematical basis for the method of finite spheres. According to [2, 72, 73], the method of finite spheres is capable of reproducing $p_m(\underline{x})$ exactly (as it is included in the local finite dimensional space V_I^h). Consequently, choosing the appropriate local approximation space V_I^h is important in order to enhance the approximation capabilities of the method of finite spheres. It has been shown that trigonometric functions are one of the appropriate choices for the solution of wave propagation problems in Chapter 2.

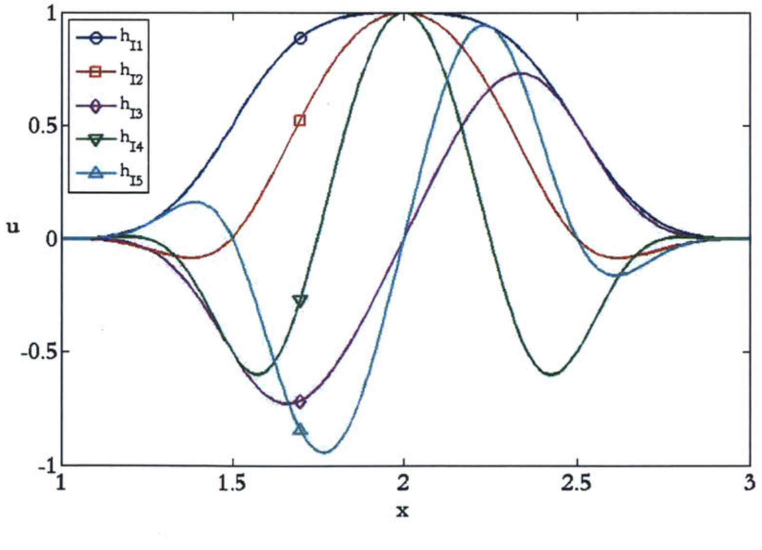

***Fig. 3.2:** One-dimensional interpolation functions for an interior node for cutoff number p=2*

$$h_{I1} = \varphi_I^0(\underline{x}), h_{I2} = h_{I1}\cos(\frac{2\pi}{\Lambda_x}x), h_{I3} = h_{I1}\sin(\frac{2\pi}{\Lambda_x}x), h_{I4} = h_{I1}\cos(\frac{2\pi}{\Lambda_x}2x), h_{I5} = h_{I1}\sin(\frac{2\pi}{\Lambda_x}2x)$$

3.2 Wave propagations in 2D

Next, we apply the framework of the method of finite spheres and present the fundamental equations governing wave propagations in two dimensions. Section 3.2.1 summarizes the formulation for the linear elastic wave equation, while Section 3.2.2 presents the formulation for the linear viscoelastic wave equation.

3.2.1 Formulation for the linear elastic wave equation

Let us consider a bounded domain $V \in R^2$ with boundary S.

The governing equation is

$$\underline{\partial}_{\varepsilon}^{T} \underline{\tau} + \underline{f}^{B} = \underline{0} \qquad \text{in } V \tag{3.9}$$

where $\underline{f}^{B}$ is the body force vector. The strain-displacement relation is

$$\underline{\varepsilon} = \underline{\partial}_{\varepsilon} \underline{u} \qquad \text{in } V \tag{3.10}$$

and the stress-strain relationship is

$$\underline{\tau} = \underline{C\varepsilon} \qquad \text{in } V \tag{3.11}$$

where $\underline{C}$ is the stress-strain material matrix. For plane strain conditions

$$\underline{C} = \begin{bmatrix} c_{11} & c_{12} & 0 \\ c_{12} & c_{11} & 0 \\ 0 & 0 & c_{33} \end{bmatrix} \tag{3.12}$$

where $c_{11} = \frac{E(1-\nu)}{(1+\nu)(1-2\nu)}$, $c_{12} = \frac{E\nu}{(1+\nu)(1-2\nu)}$, and $c_{33} = \frac{E}{2(1+\nu)}$ with E and ν being the Young's modulus and Poisson's ratio of the material, respectively.

The boundary conditions are

$$\underline{N\tau} = \underline{f}^S \quad \text{on } S_f \tag{3.13}$$

$$\underline{u} = \underline{u}^S \quad \text{on } S_u \tag{3.14}$$

In Eqs. (3.9) - (3.11), $\underline{u}$, $\underline{\varepsilon}$, and $\underline{\tau}$ are the displacement, strain, and stress vectors, respectively; $\underline{\partial}_\varepsilon$ is a linear gradient operator; $\underline{f}^S$ is the prescribed traction vector on the Neumann boundary S_f; $\underline{u}^S$ is the vector of prescribed displacements on the Dirichlet boundary S_u ; and $\underline{N}$ is the matrix of direction cosine components of a unit normal to the domain boundary [2 - 5].

3.2.1.1 Variational form

We consider the following variational indicator [2 - 5]:

$$\Pi^*(\underline{u}) = \int_V \tfrac{1}{2}\underline{\varepsilon}^T(\underline{u})\underline{C}\underline{\varepsilon}(\underline{u})dV - \Re \tag{3.15}$$

The term $\Re$ accounts for the externally applied body forces, surface tractions, and applied displacements,

$$\Re = \int_V \underline{u}^T \underline{f}^B dV + \int_{S_f} \underline{u}^T \underline{f}^S dS + \int_{S_u} \underline{f}^{uT}(\underline{u} - \underline{u}^S)dS \tag{3.16}$$

where $\underline{f}^u$ is the traction vector on the Dirichlet boundary and may be expressed as

$$\underline{f}^{u} = \underline{NC\varepsilon(\underline{u})} \qquad (3.17)$$

and we have $\underline{f}^{B} = -\rho\underline{\ddot{u}}$ where only body forces due to inertia forces are considered [6].

Invoking the stationarity of Π^{*}, we obtain the following weak form:

Find $\underline{u} \in H^{1}(V)$ such that

$$\begin{aligned}\int_{V} \underline{\varepsilon}^{T}(\underline{v})\underline{C\varepsilon(\underline{u})}dV + \int_{V} \rho\underline{v}^{T}\underline{\ddot{u}}dV - \int_{S_u}\left[\underline{\varepsilon}^{T}(\underline{v})\underline{CN}^{T}\underline{u} + \underline{v}^{T}\underline{NC\varepsilon(\underline{u})}\right]dS \\ = \int_{S_f}\underline{v}^{T}\underline{f}^{S}dS - \int_{S_u}\underline{\varepsilon}^{T}(\underline{v})\underline{CN}^{T}\underline{u}^{S}dS \qquad \forall\underline{v} \in H^{1}(V)\end{aligned} \qquad (3.18)$$

where $H^{1}(v)$ is the first order Hilbert space [2 - 6].

3.2.1.2 Nodal interpolations

The displacement field is approximated from Eq. (3.5)

$$\underline{u}(x,y) = \sum_{J=1}^{N}\sum_{n\in 3}\underline{H}_{Jn}(x,y)\underline{\alpha}_{Jn} = \underline{H}(x,y)\underline{U} \qquad (3.19)$$

where

$$\underline{U} = [\underline{\alpha}_{11} \quad \underline{\alpha}_{12} \quad \underline{\alpha}_{13} \quad \cdots \quad \underline{\alpha}_{Jn} \quad \cdots]^{T} \qquad (3.20)$$

is the vector of nodal unknowns, and

$$\underline{\alpha}_{Jn} = [u^{Jn} \quad v^{Jn}] \qquad (3.21)$$

is the vector of nodal unknowns at node J corresponding to the nth degree of freedom (u^{Jn} and v^{Jn} are the nodal variables for the x and y direction displacements). The nodal shape function matrix corresponding to the nth degree of freedom is

$$\underline{H}_{Jn}(x,y) = \begin{bmatrix} h_{Jn}(x,y) & 0 \\ 0 & h_{Jn}(x,y) \end{bmatrix} \tag{3.22}$$

Hence, the discretized versions of Eqs. (3.10) and (3.11) are

$$\underline{\varepsilon}(x,y) = \sum_{J=1}^{N} \sum_{n\in\Im} \underline{B}_{Jn}(x,y)\underline{\alpha}_{Jn} = \underline{B}(x,y)\underline{U} \tag{3.23}$$

and

$$\underline{\tau}(x,y) = \sum_{J=1}^{N} \sum_{n\in\Im} \underline{C}\underline{B}_{Jn}(x,y)\underline{\alpha}_{Jn} = \underline{C}\underline{B}(x,y)\underline{U} \tag{3.24}$$

where the strain-displacement matrix $\underline{B}(x,y)$ is partitioned as

$$\underline{B}(x,y) = [\underline{B}_{11}(x,y) \quad \underline{B}_{12}(x,y) \quad \cdots \quad \underline{B}_{Jn}(x,y) \quad \cdots] \tag{3.25}$$

with

$$\underline{B}_{Jn}(x,y) = \underline{\partial}_{\varepsilon}\underline{H}_{Jn}(x,y) = \begin{bmatrix} \partial h_{Jn}/\partial x & 0 \\ 0 & \partial h_{Jn}/\partial y \\ \partial h_{Jn}/\partial y & \partial h_{Jn}/\partial x \end{bmatrix} \tag{3.26}$$

3.2.1.3 Discrete equations

Substituting Eqs. (3.19) - (3.26) into Eq. (3.18), we obtain the discrete system of algebraic equations corresponding to node I and degree of freedom m

$$\sum_{J=1}^{N}\sum_{n\in\Im}\underline{K}_{ImJn}\underline{\alpha}_{Jn}+\sum_{J=1}^{N}\sum_{n\in\Im}\underline{M}_{ImJn}\underline{\ddot{\alpha}}_{Jn}=\underline{\hat{f}}_{Im} \tag{3.27}$$

In this equation, the various matrices and vectors are as follows:

$$\underline{K}_{ImJn}=\int_{V_I}\underline{B}_{Im}^{T}\underline{C}\underline{B}_{Jn}dV \tag{3.28}$$

$$\underline{M}_{ImJn}=\int_{V_I}\rho\underline{H}_{Im}^{T}\underline{H}_{Jn}dV \tag{3.29}$$

where $V_I=V\cap B(\underline{x}_I,r_I)$.

If I is a node associated with an interior sphere, then

$$\underline{\hat{f}}_{Im}=\underline{0} \tag{3.30}$$

If the sphere corresponding to node I has nonzero intercept on the Neumann boundary, then

$$\underline{\hat{f}}_{Im}=\int_{S_{fI}}\underline{H}_{Im}^{T}\underline{f}^{S}dS \tag{3.31}$$

where $S_f=\bigcup_{I\in N_f}S_{f_I}$, with N_f being the index set of such nodes.

On the other hand, if the sphere corresponding to node I has nonzero intercept on the Dirichlet boundary, then

$$\underline{\hat{f}}_{Im}=\sum_{J=1}^{N}\sum_{n\in\Im}\underline{KU}_{ImJn}\underline{\alpha}_{Jn}-\underline{fU}_{Im} \tag{3.32}$$

where

$$\underline{KU}_{ImJn}=\int_{S_{uI}}\underline{H}_{Im}^{T}\underline{NCB}_{Jn}dS+\int_{S_{uI}}\underline{B}_{Im}^{T}\underline{CN}^{T}\underline{H}_{Jn}dS \tag{3.33}$$

and

$$\underline{fU}_{Im} = \int_{S_{uI}} \underline{B}_{Im}^{T}\underline{C}\underline{N}^{T}\underline{u}^{S}dS \tag{3.34}$$

where $S_u = \bigcup_{I \in N_u} S_{u_I}$, with N_u being the index set of such nodes. A point to note is that we may incorporate the Dirichlet boundary conditions by a special arrangement of nodes as discussed in [2 - 5]. If we use the special arrangement of nodes on the Dirichlet boundary condition, then the specified value of the field variable u at node I on the Dirichlet boundary is taken up by the coefficient of h_{I1}.

3.2.2 Formulation for the linear viscoelastic wave equation

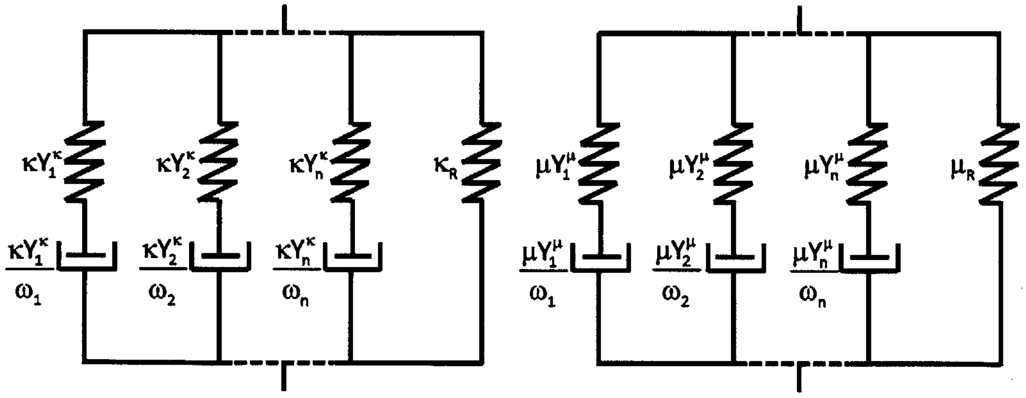

(a) *(b)*

Fig. 3.3: *Schematic of the generalized Maxwell body for (a) the complex viscoelastic bulk modulus and (b) the complex viscoelastic shear modulus.*

In an isotropic viscoelastic body, the stress-strain relation can be expressed in Einstein notation as

$$\tau_{ij}(t) = \delta_{ij}\int_{-\infty}^{t} \kappa(t-\tau)\dot{\varepsilon}_{kk}(\tau)d\tau + 2\int_{-\infty}^{t} \mu(t-\tau)[\dot{\varepsilon}_{ij}(\tau) - \frac{1}{3}\delta_{ij}\dot{\varepsilon}_{kk}(\tau)]d\tau \tag{3.35}$$

where $\kappa(t)$ and $\mu(t)$ are bulk and shear relaxation functions, respectively [74 - 77]. We use a generalized Maxwell body, which is constructed in the frequency domain, to approximate these two relaxation functions [77]. *Fig. 3.3* shows the schematic illustration of the complex viscoelastic bulk modulus and shear modulus, respectively. The elastic bulk modulus and the elastic shear modulus are κ and μ, respectively, Y_l^{κ} and Y_l^{μ} are the coefficients, ω_l are the relaxation frequencies, n is the number of relaxation mechanisms, and l ranges from 1 to n [77]. The expressions relating the elastic bulk modulus to the relaxed bulk modulus, κ_R, and the elastic shear modulus to the relaxed shear modulus, μ_R, respectively, are

$$\kappa = \kappa_R + \kappa \sum\nolimits_{l=1}^{n} Y_l^{\kappa} \tag{3.36}$$

and

$$\mu = \mu_R + \mu \sum\nolimits_{l=1}^{n} Y_l^{\mu} \tag{3.37}$$

By transforming the two complex viscoelastic moduli from the frequency domain to the time domain, we can obtain the stress-strain relation in the time domain [77] as

$$\tau_{ij} = \kappa \varepsilon_{kk} \delta_{ij} + 2\mu[\varepsilon_{ij} - \frac{1}{3}\varepsilon_{kk}\delta_{ij}] - \sum\nolimits_{l=1}^{n} [\kappa \mathrm{Y}_l^{\kappa} \zeta_l^{kk} \delta_{ij} + 2\mu \mathrm{Y}_l^{\mu} (\zeta_l^{ij} - \frac{1}{3}\zeta_l^{kk}\delta_{ij})] \tag{3.38}$$

where ζ_l^{ij} is the function defined as

$$\zeta_l^{ij}(t) = \omega_l (\int_{-\infty}^{t} \exp(-\omega_l (t-\tau)) \cdot \varepsilon_{ij}(\tau) d\tau) \tag{3.39}$$

which can be changed into

$$\dot{\zeta}_l^{ij} + \omega_l \zeta_l^{ij} = \omega_l \varepsilon_{ij} \qquad (3.40)$$

For plane strain conditions, we write the stress in the form

$$\underline{\tau} = \underline{\tau}^E - \sum_{l=1}^{n} \underline{\tau}^{Al} \qquad (3.41)$$

where $\underline{\tau}^E$ is the elastic contribution given by Eq. (3.11), and $\underline{\tau}^{Al}$ is the viscous contribution which on unloading disappears for the *l*th relaxation frequency given by

$$\underline{\tau}^{Al} = \underline{C}^{Al} \underline{\zeta}_l \qquad (3.42)$$

where

$$\underline{C}^{Al} = \begin{bmatrix} Y_l^+ & Y_l^- & 0 \\ Y_l^- & Y_l^+ & 0 \\ 0 & 0 & \mu Y_l^\mu \end{bmatrix} \text{ and } \underline{\zeta}_l = [\zeta_l^{xx} \quad \zeta_l^{yy} \quad 2\zeta_l^{xy}]^T \qquad (3.43)$$

where

$$Y_l^+ = \kappa Y_l^\kappa + \frac{4}{3}\mu Y_l^\mu; \quad Y_l^- = \kappa Y_l^\kappa - \frac{2}{3}\mu Y_l^\mu \qquad (3.44)$$

The coefficients Y_l^κ and Y_l^μ are obtained from

$$Q_\nu^{-1}(\tilde{\omega}_k) = \sum_{l=1}^{n} \frac{\omega_l \tilde{\omega}_k + \omega_l^2 Q_\nu^{-1}(\tilde{\omega}_k)}{\omega_l^2 + \tilde{\omega}_k^2} Y_l^\nu; \quad k = 1, \ldots, 2n-1; \quad \nu \in \{p,\ s\} \qquad (3.45)$$

where Q_p and Q_s are quality factors which characterize the attenuation of the viscoelastic P- and S-waves, respectively [77]. The relaxation frequencies are obtained by defining $\tilde{\omega}_1 = \omega_1, \ldots, \tilde{\omega}_{2n-1} = \omega_n$, where $k = 1, \ldots, 2n-1$. The coefficients can be solved for by Eq. (3.45) using the least square method.

The coefficients Y_l^p , Y_l^s and Y_l^κ , Y_l^μ are related to each other through the expressions

$$Y_l^\kappa = \frac{(\mathrm{c}_p^2 \mathrm{Y}_l^p - \frac{4}{3}\mathrm{c}_s^2 \mathrm{Y}_l^s)}{(\mathrm{c}_p^2 - \frac{4}{3}\mathrm{c}_s^2)}; \quad Y_l^\mu = Y_l^s \tag{3.46}$$

where c_p and c_s are the elastic P- and S-wave velocities, respectively.

3.2.2.1 Discrete equations

The difference between the linear viscoelastic wave equation and the linear elastic wave equation is embedded in the definition of the stress. In particular, the stress defined in Eq. (3.41) for the viscoelastic wave includes the additional viscous effect which on unloading disappear, whereas the stress defined in Eq. (3.11) for the elastic wave, only has the elastic effect. Consequently, the counterpart to Eq. (3.27), the discrete set of equations for the elastic wave, is the following discrete set of equations

$$\sum_{J=1}^{N} \sum_{n \in \mathfrak{I}} \underline{K}_{ImJn} \underline{\alpha}_{Jn} + \sum_{J=1}^{N} \sum_{n \in \mathfrak{I}} \underline{M}_{ImJn} \underline{\ddot{\alpha}}_{Jn} = \underline{\hat{f}}_{Im} + \underline{\hat{f}}_{Im}^{A} \tag{3.47}$$

where $\underline{\hat{f}}_{Im}^{A} = \int_{V_I} \underline{\underline{B}}_{Im}^{T} \underline{\underline{\hat{\Sigma}}} dV$ is the force vector accounting for element stresses due to the viscous effects which on unloading disappears, $\underline{\underline{\hat{\Sigma}}} = \sum_{l=1}^{n} \underline{\underline{\tau}}^{Al}$.

3.3 Improved numerical integration procedure

Numerical integration is a focal point of development for the method of finite spheres [78 - 80]. Unlike the finite element method where numerical integration is efficient due to polynomial interpolation functions, non-overlapping elements, and Gauss-Legendre product rules used over simple integration domains, the method of finite spheres requires integration of nonpolynomial functions over complicated integration domains such as spheres, truncated spheres, and general lens-shaped regions for the overlap of spheres. Consequently, specialized integration schemes have been developed, such as the piecewise midpoint quadrature rule in Ref. [78]. While the integration rule suggests that it is possible to contend with classical finite element procedures [78], more efficient integration schemes are still needed and essential to the success of the method of finite spheres. In this Section, we focus on developing a computationally efficient numerical integration procedure for the method of finite spheres for two-dimensional integration domains. By applying the integration rule to a two-dimensional linear elastostatics cantilever plate problem, we seek to demonstrate the improvements in numerical integration as a result of our new proposed integration method. The efficiency of the proposed integration method will then be further verified on problems of wave propagation in Section 3.4.

3.3.1 Piecewise midpoint quadrature rule

The piecewise midpoint quadrature rule was first presented by De and Bathe [78] as an improved numerical integration rule from the former Gaussian product rules [2]. Since the integrands to be evaluated are nonpolynomial functions over complicated integration domains, a high order Gauss quadrature rule was required, which is not efficient. The premise of the piecewise midpoint quadrature rule is to subdivide the domain and perform integration in a piecewise manner over these subdomains with simpler quadrature rules. The complication of the integration scheme is the selection of the number of integration points within each integration domain.

3.3.2 Piecewise Gauss-Legendre quadrature rule

While the piecewise midpoint quadrature rule decreased the computational time of the method of finite spheres [78], the integration rule still needs to be improved. A prominent challenge is the appropriate selection of the number of integration points within the integration domains. Since the solution is sensitive to the balance of integration points within each integration domain, the method lacks reliability. By inspecting the interior disk, it is evident that the number of integration points near the center is greater than the density of integration points near the boundary. Furthermore, the location and weights of the integration points for the regions of overlap do not coincide with the integration points of the interior disk or boundary sector, and the error can accumulate when the accuracy of the integrand for these integration domains are not of the same order.

Consequently, the piecewise Gauss-Legendre quadrature rule was developed with consideration of the density of the integration points. Furthermore, to avoid the reliability issue of relative error between the overlap and the interior disk or boundary sector, we do not calculate the overlap regions with a different set of integration points, but rather, we use the same location and weights as defined within the interior disk or boundary sector.

The integration domains for two-dimensional conditions are interior disks, boundary sectors, and lens-shaped regions of overlap, but for the piecewise Gauss-Legendre quadrature rule, the integrands for the lens-shaped regions of overlap are computed with the position and weights of the integration points for the interior disk or boundary sector. The premise of this integration scheme is to reduce the complexity of the integrand by subdividing the integration domain into quadrants and employing Gauss-Legendre quadrature which provides an equal density arrangement of integration points. For each of these domains, the procedure for the piecewise Gauss-Legendre quadrature rule will be summarized.

3.3.2.1 Interior disk

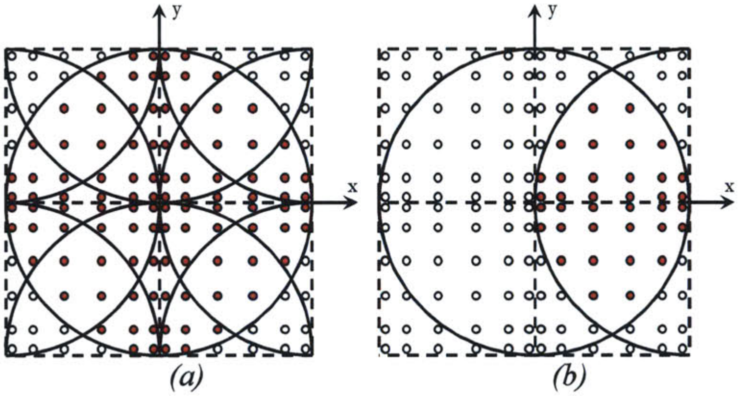

Fig. 3.4: *Integration points on interior disk (a) and lens-shaped region of overlap (b) for piecewise Gauss-Legendre quadrature rule.*

The piecewise Gauss-Legendre quadrature rule subdivides the interior disk into four quadrants as in *Fig. 3.4*. Within each of these subdomains, a Gauss-Legendre quadrature rule is selected, with the objective of achieving a reasonably accurate solution using a minimal number of integration points. Note that only the integration points within the disk will contribute to the interior disk stiffness calculation (red points in *Fig. 3.4(a)*). The location and weights of the integration points used to calculate the stiffness of the lens-shaped region of overlap coincide with those used for the interior disk stiffness calculation. In *Fig. 3.4(b)*, the red points indicate the integration points used to calculate the stiffness contribution corresponding to the overlap region shown. The Gauss-Legendre quadrature is performed in the global domain in contrast to the integration scheme of the MLPG method as in Ref. [56] where the integration is performed using isoparametric mapping. The piecewise Gauss-Legendre quadrature rule differs from general Gauss product rules in that the integration domain is first subdivided to simplify the functions that are to be integrated.

3.3.2.2 Boundary sector

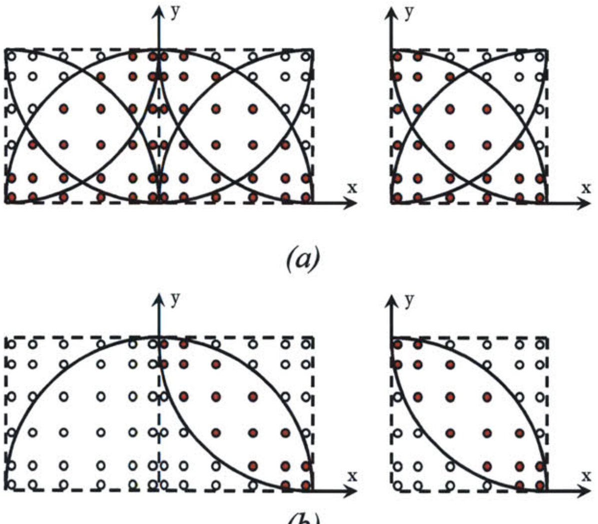

(a)

(b)

Fig. 3.5: *Integration points on boundary sectors (a) and lens-shaped region of overlap (b) for piecewise Gauss-Legendre quadrature rule.*

For the piecewise Gauss-Legendre quadrature rule for boundary sectors, the integration domain is divided into subdomains. The number of quadrants depends on the angle that the radii joining the center of the disk to the two intercepts of the disk make interior to the domain. Within each of these quadrants, a Gauss-Legendre quadrature rule is employed, but as for the interior disk, only the points within the boundary sector contribute to the stiffness term of the spheres with nonzero intercept with the domain boundary. *Fig. 3.5(a)* illustrates the integration points within the boundary sectors encountered in the two-dimensional problems presented in this thesis based on the Gauss-Legendre quadrature rule while *Fig. 3.5(b)* illustrates those points for the lens-shaped region of overlap.

3.3.3 Numerical integration rule comparison

For the finite element method, the element type, the mesh density, and the solution parameters are some of the choices that must be refined until sufficient accuracy is obtained. For the method of finite spheres, the sphere size, the local approximation space, the type of integration scheme, and the imposition of the boundary conditions are some of the choices that must be refined until sufficient accuracy is obtained. By comparing the error in strain energy for the method of finite spheres with the traditional finite element method, we will illustrate the advantages and disadvantages of the numerical integration scheme.

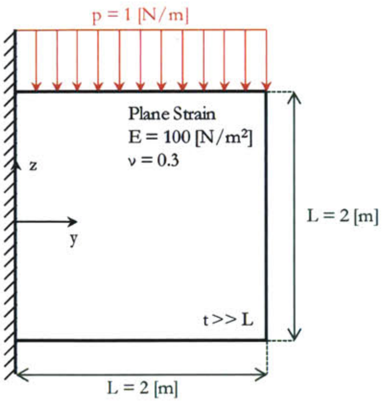

Fig. 3.6: *Cantilever plate problem.*

To illustrate the improvement in numerical integration, consider the cantilever plate problem in *Fig. 3.6*. This two-dimensional linear elasticity problem will be solved using the method of finite spheres with the piecewise Gauss-Legendre quadrature rule. For two-dimensional wave propagation problems, the local approximation space is given by Eq. (3.6), so the global approximation is the Shepard partition of unity functions enriched by these trigonometric functions. However, a suitable local approximation space for two-dimensional linear elasticity problems are the polynomial functions. For this example, we take the terms of a complete second degree polynomial, that is, $V_I^h = \text{span}\{1, x, y, x^2, xy, y^2\}$.

The piecewise midpoint quadrature rule is an improved numerical integration method as compared to the Gauss product rules which can only provide 'global' accuracy of the integration domain up to an arbitrary polynomial order. Since the integrands are complex nonpolynomial functions, the Gauss product rules, which can only give exact results when applied to a polynomial, require a large number of integration points and are not efficient. However, the piecewise Gauss-Legendre quadrature rule allows for 'local' high order approximations within the subdomains of the integration domain. Since the numerical integration errors are due to the complexities of the integrand, subdividing the quadrature domain into subdomains yields more accurate solutions since the complex integrand is divided into simpler functions. Consequently, proper choice of how to subdivide the domain can greatly increase the effectiveness of the piecewise Gauss-Legendre quadrature rule. An optimal solution is one that achieves a reasonable level of accuracy using minimal divisions, since an increase in the number of partitions increases the computational effort. The interpolation functions of the traditional finite element method and the method of finite spheres are illustrated in *Fig. 3.7*. An advantage of the piecewise Gauss-Legendre quadrature rule is that the stiffness terms corresponding to the overlap regions are calculated with the same location and weights of the integration points within the interior disk or boundary sector. Therefore, we anticipate that the piecewise Gauss-Legendre quadrature rule will be an improvement upon the piecewise midpoint quadrature rule.

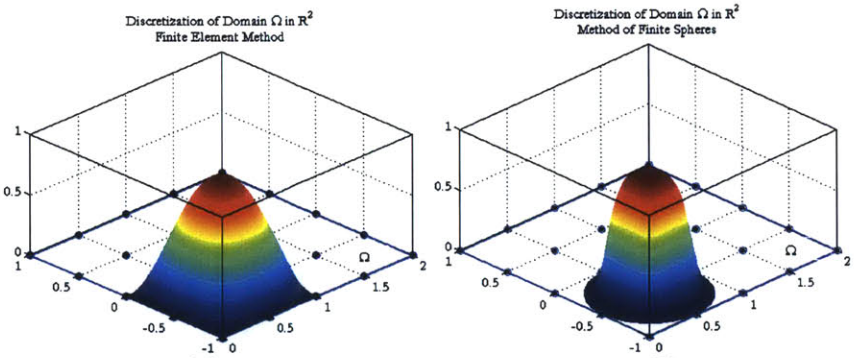

(a) *(b)*

Fig. 3.7: *(a) Discretization of the finite element domain with Lagrange shape function for a middle node and (b) discretization of the finite sphere domain with internal disk shape function.*

3.3.3.1 Strain energy convergence

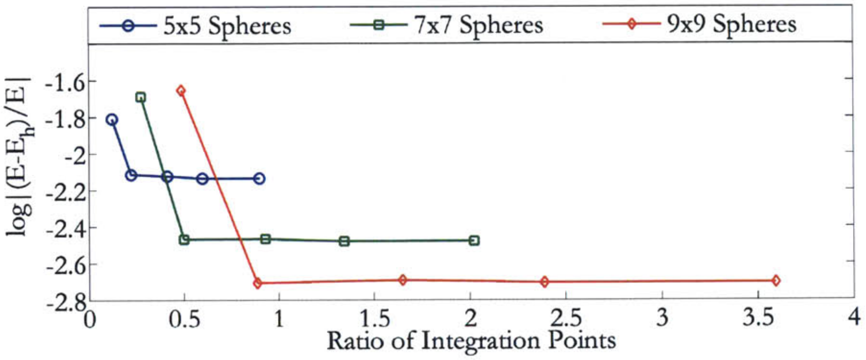

Fig. 3.8: *Strain energy convergence for the piecewise Gauss-Legendre quadrature rule*

The error in strain energy is determined from the reference solution which is based on the 50×50 9-node finite element solution of the cantilever plate problem. The strain energy convergence plot presented in *Fig. 3.8* is for the method of finite spheres using the piecewise Gauss-Legendre quadrature rule. The ratio of integration points is determined by the number of integration points used in the method of finite spheres divided by the number of integration points used in the finite element reference solution. Three sphere sizes are used for this numerical integration scheme.

Using the piecewise Gauss-Legendre quadrature rule, it is evident that the method of finite spheres solution converges as seen in *Fig. 3.8*. The behavior exhibited is similar to the finite element method in that using a number of integration points above a certain value will not improve the solution. By observing the ratio of integration points, it is apparent that the computational cost for the method of finite spheres is comparable to that of the finite element method. For a decrease in the radius of support, we see an improvement of the error in strain energy.

Therefore, the piecewise Gauss-Legendre quadrature rule demonstrates qualities desirable of an efficient numerical integration scheme.

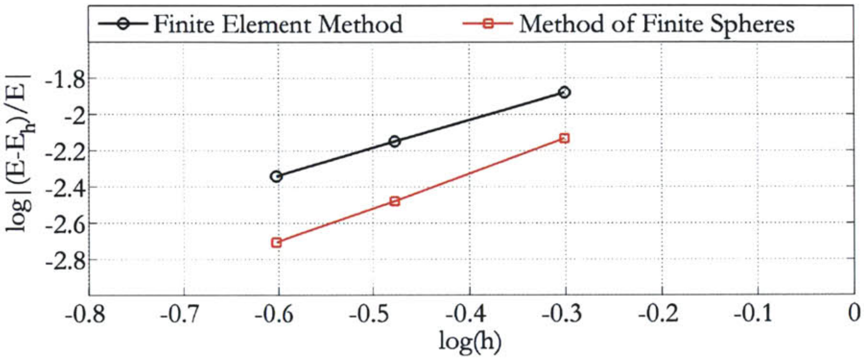

Fig. 3.9: *Strain energy convergence with decrease in element size for the finite element method and decrease in radius of support for the method of finite spheres.*

From *Fig. 3.9*, it is clear that the method of finite spheres using the piecewise Gauss-Legendre quadrature rule has a comparable rate of convergence as the finite element method as seen from the slope of the two curves. Furthermore, by noting the shift between the two convergence rate curves, it is clear that for a chosen element/sphere size, the method of finite spheres using the piecewise Gauss-Legendre quadrature rule provides a more accurate solution than the finite element method. Therefore, since the accuracy and efficiency of the method of finite sphere using the piecewise Gauss-Legendre quadrature rule is comparable to that of the finite element method, it appears that this numerical integration scheme has improved the method of finite spheres to be competitive with the traditional finite element method.

For the two-dimensional wave propagation problems presented in this thesis, the method of finite spheres is using the piecewise Gauss-Legendre quadrature rule. The advantages of this improved numerical integration scheme was demonstrated in this Section for the cantilever plate problem but the integration rule is similarly efficient for wave propagation problems. Furthermore, additional computational savings can be gained from the analysis of wave propagation problems when employing a uniform arrangement of equally sized spheres. The solutions to wave propagation problems can exploit this uniform arrangement since the solution is not confined to any specific region. Therefore, due to this uniform arrangement, the integration over interior spheres can be patternized in order to significantly reduce the stiffness and mass calculation cost.

3.3.3.2 Cantilever plate problem results

The computational cost of numerical techniques can be measured by the time of the solution procedure, often approximated by the number of operations. The major computational cost is in the computation of the global stiffness matrix and in the solution of the resulting set of algebraic equations. For the method of finite spheres, this means that the most expensive operations are the computation of the interpolation functions and their derivatives, which are evaluated at every integration point.

For the cantilever plate problem, the solution fields for displacement will be compared for the finite element method and the method of finite spheres. The centerline vertical displacement from the two methods will also be presented. The finite element model results presented are based on a 50×50 9-node element mesh and the method of finite spheres results presented are based on a 9×9 arrangement of spheres.

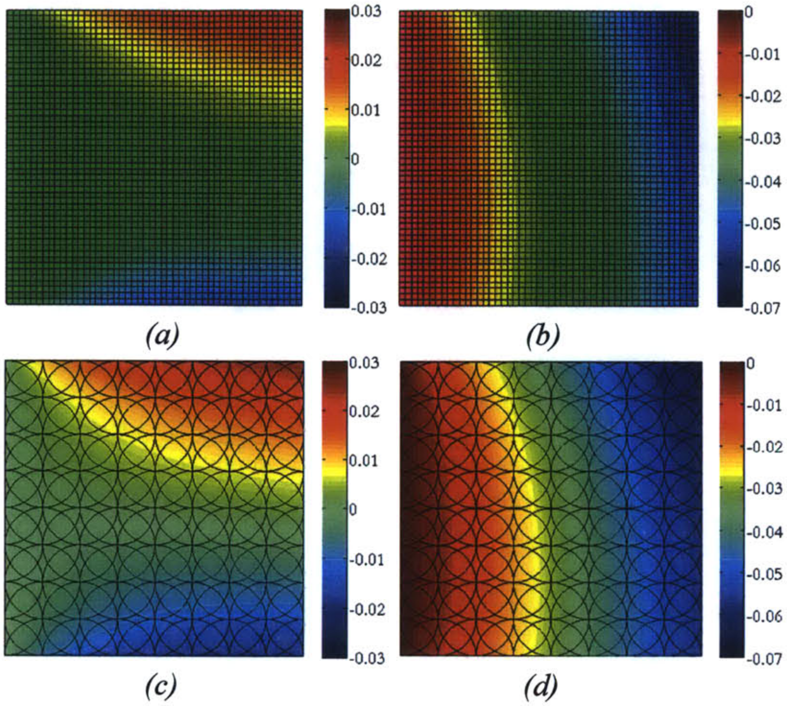

Fig. 3.10: *Finite element results of (a)* y *-displacement and (b)* z *-displacement and method of finite spheres results of (c)* y *-displacement and (d)* z *-displacement.*

The displacement results of the finite element method in *Fig. 3.10(a)-(b)* are similar to the displacement results of the method of finite spheres in *Fig. 3.10(c)-(d)*. The vertical deflection of the neutral axis for the method of finite spheres using the piecewise Gauss-Legendre quadrature rule is in agreement with the results of the classical finite element method as can be seen from *Fig. 3.11*.

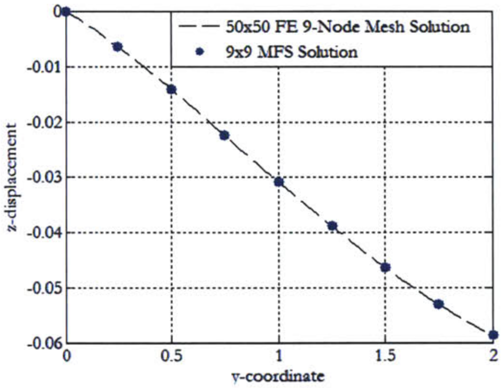

Fig. 3.11: *Vertical deflection of the neutral axis for the 50×50 FE 9-node mesh and the 9×9 MFS discretization.*

In the midst of increasing popularity for meshless methods, the method of finite spheres is proving to be a promising numerical technique for the analysis of solids, structures, fluid flows, and fluid-structure interaction. While the method provides reliably accurate solutions, the method lacks in computational efficiency when compared to the traditional finite element method. Consequently, the piecewise Gauss-Legendre quadrature rule was developed where from the results of the cantilever plate problem, it is apparent that the method provides an accurate solution with far fewer integration points than the previous piecewise midpoint quadrature rule.

3.4 Numerical examples

The objective of this Section is to demonstrate the computational potential of the method of finite spheres for the solution of wave propagation problems. The examples used will demonstrate novel features of the method of finite spheres including the use of interpolation functions enriched by trigonometric functions as well as the piecewise Gauss-Legendre quadrature rule for the numerical integration procedure.

The first example is a two-dimensional scalar wave propagation problem. This problem will demonstrate that accurate approximate solutions can be obtained using the method of finite spheres. Furthermore, it will reveal certain behavior of the approximate solutions when varying the sphere size, cutoff number, and time step size. The method of finite spheres exhibits interesting behavior indicating whether an error is due to discretization in space or time. We provide an estimate for determining an appropriate time step size for the method of finite spheres in the analysis of wave propagation problems. Finally, the computational costs using the method of finite spheres are measured and compared with those using the finite element method.

The second problem deals with scattered waves by an array of rigid circular cylinders. This example illustrates the simple and direct procedure of discretization for the method of finite spheres.

The next model concerns a two-dimensional linear elastic wave propagation problem in a semi-infinite domain. In this example, we focus on the wave propagation along the surface. Some meshless methods have shown poor accuracy in approximating solutions along the free-surface boundary. This example will illustrate the strong performance of the method of finite spheres with regard to the free-surface boundary condition.

Lastly, the fourth problem is a two-dimensional viscoelastic wave propagation problem. While elastic wave propagation is of importance, many media show significant viscosity, and therefore, cannot be idealized as linear elastic bodies.

Consequently, this example will demonstrate how the method of finite spheres is able to capture this viscous dissipation.

3.4.1 Two-dimensional scalar wave propagation problem

In this Section, we solve a scalar wave equation with the Dirichlet and Neumann boundary conditions considered in [71]. Due to the symmetry of the solution profile, we consider only a quarter of the domain. Let $V \in R^2$ be a bounded two-dimensional domain with the Dirichlet boundary on $x = y = 1\text{m}$ and the Neumann boundary on $x = y = 0\text{m}$. The initial boundary value problem consists of finding the solution u that satisfies

$$c^{-2}\ddot{u}(\underline{x},t) - \Delta u(\underline{x},t) = \tilde{f}(\underline{x},t) \quad in \ V_T = V \times I; \ V = [0,1\text{m}]^2, \ I = (0, 0.95\text{s}) \qquad (3.48)$$

where c is the wave speed and the initial conditions are

$$u(\underline{x},0) = 0; \ \dot{u}(\underline{x},0) = 0 \quad on \ V \qquad (3.49)$$

These equations are related to the dynamic motion of a prestressed membrane [81]. We choose $c = 1\text{m/s}$ and $\tilde{f}(0,0,t) = 10(1 - 2\pi^2 \hat{f}^2 (t - t_0)^2)\exp(-\pi^2 \hat{f}^2 (t - t_0)^2)$, where $\hat{f} = 6\text{Hz}$ and $t_0 = 0.25\text{s}$ are the central frequency and time shift, respectively.

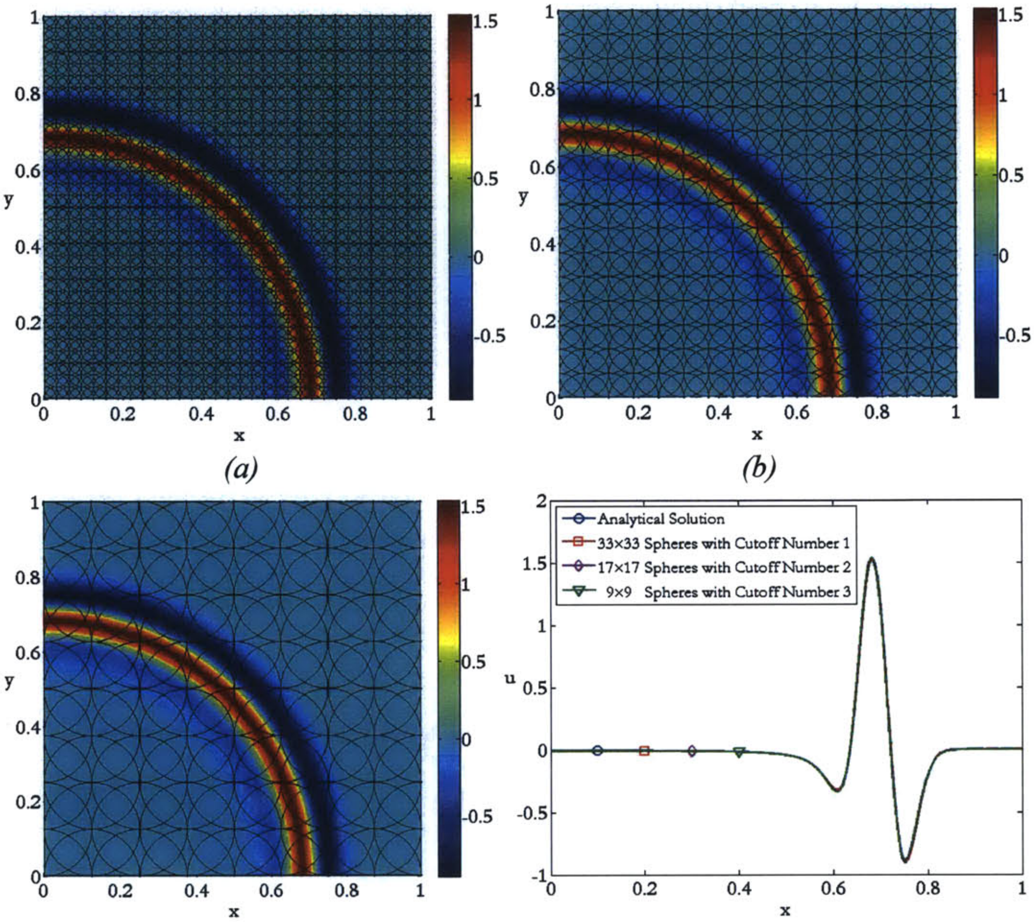

(a) *(b)* *(c)* *(d)*

Fig. 3.12: *Displacement variations at time 0.95s for (a) 33×33 spheres with cutoff number 1, (b) 17×17 spheres with cutoff number 2, (c) 9×9 spheres with cutoff number 3, and (d) a comparison between analytical solution and numerical solutions for response along* x *-axis.*

The Bathe time integration method was used to obtain the approximate solutions since it has been proven to provide more accurate solutions for wave propagation problems than the trapezoidal rule [82]. For the approximate solutions in *Fig. 3.12*, a time step size of $\Delta t = 0.003125\text{s}$ was used, which is small enough to assume that temporal discretization errors are negligible. *Fig. 3.12(a)-(c)* illustrates the wave response at time t = 0.95s for varying cutoff numbers and sphere sizes and *Fig. 3.12(d)* compares these approximate solutions to the analytical solution on the axis $x = 0$ [25]. The numerical results are satisfactory. We will use this example to further investigate the accuracy of the method of finite spheres by varying the spatial and temporal discretization.

3.4.1.1 Spatial and temporal discretization error

The purpose of a numerical method is to provide accurate solutions to the physical system of interest. For the wave propagation problems analyzed in this Section, analytical solutions are available so that the relative accuracy of our numerical results can be tested directly. However, it is important to investigate the sensitivity of the solution for our method since it is for solutions to complex physical phenomena, for which analytical solutions are not known, that the accuracy of the method is essential.

In numerical solutions, the error is usually a consequence of spatial and/or temporal discretization [81]. In order to minimize the spatial discretization error in the method of finite spheres, either the sphere size can be decreased, similar to h-refinement, or the cutoff number can be increased, comparable to p-refinement in the finite element method [6, 72]. To examine the h- and p-convergence of the method of finite spheres, we use the percentage relative error of the L^2 norm

$$\sqrt{\frac{\int_V |u-u_h|^2\,dV}{\int_V |u|^2\,dV}} \times 100(\%) \qquad (3.50)$$

where u is the analytical solution and u_h is the numerical solution. *Fig. 3.13* shows the h- and p-convergence behavior of the method of finite spheres solution at time 0.95s for the scalar wave problem. As expected, *Fig. 3.13(a)* signifies that for decreasing sphere radius (for different cutoff numbers) the solution accuracy improves, while *Fig. 3.13(b)* indicates an improvement for increasing cutoff number (for different sphere sizes).

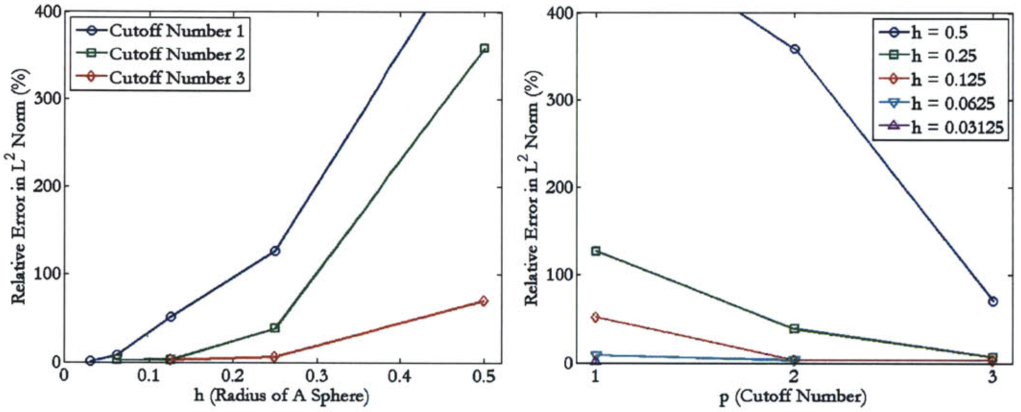

(a) *(b)*

Fig. 3.13: *(a) h-convergence and (b) p-convergence behavior of the method of finite spheres at time 0.95s.*

To inspect the accuracy of the displacement variations of the method of finite spheres solution with regard to spatial discretization, consider the relatively coarse 5×5 sphere discretization corresponding to a sphere radius size of 0.25. The percentage relative error of the L^2 norm for this discretization, using the cutoff number $p = 3$, is roughly 6.6%.

Fig. 3.14 illustrates the displacement variation results for this discretization and cutoff number at time 0.95s as well as a comparison of the numerical solution and analytical solution for the response along the x-axis. While the wavelength and amplitude of the wave agree well with the exact solution, we observe spurious oscillations in the response surrounding the peak displacement. The oscillations are a result of the spatial discretization. Therefore, while a relatively good quality solution can be obtained for the peak displacement using a coarse spatial discretization, spatial refinement is necessary to obtain a solution void of spurious oscillations.

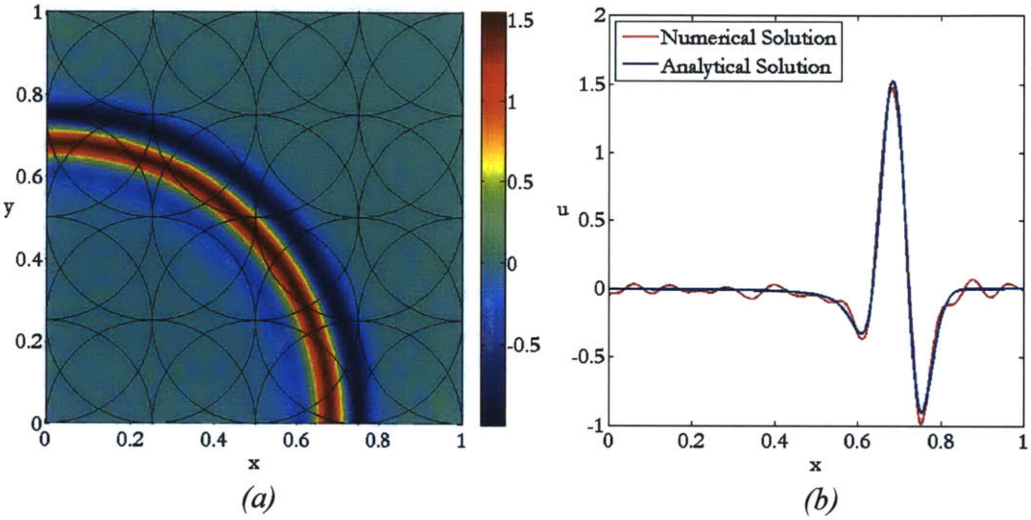

Fig. 3.14: *Displacement variations at time 0.95s for (a) 5×5 spheres with cutoff number 3 and (b) a comparison between analytical and numerical solution for response along x-axis.*

To inspect the accuracy of the displacement variations of the method of finite spheres solution with regard to temporal discretization, consider different time step sizes for the solution of the scalar wave problem. *Fig. 3.15* shows the results for the wave displacement along the *x*-axis at time 0.95s for four different time step sizes. Observe that as the time step size increases, the numerical wave profile shifts from the exact solution. The period elongation and amplitude decay of the numerical results are a result of dispersion and dissipation errors [15]. However, there are only few spurious oscillations in the solution, so we do not expect that spatial discretization is an issue. We can attribute the dispersion and dissipation error to an insufficient temporal discretization.

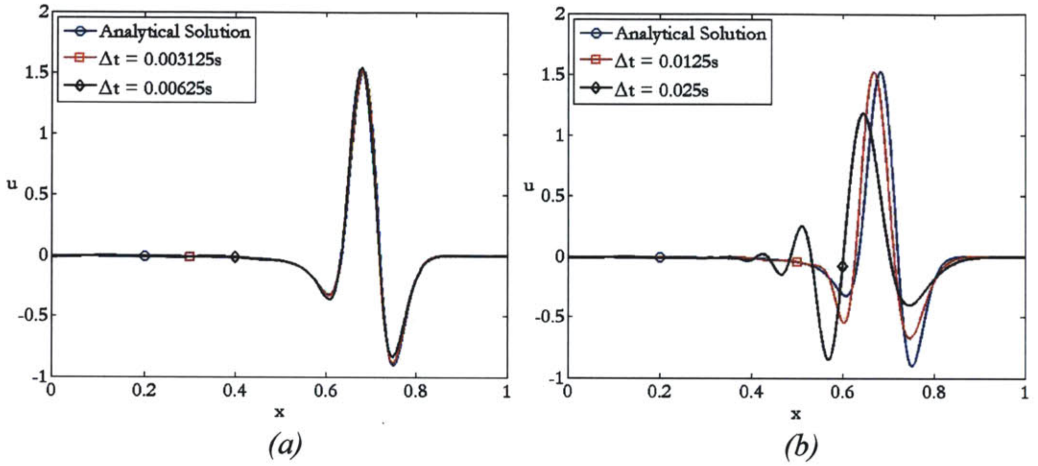

(a) *(b)*

Fig. 3.15: *Displacement variations along x-axis at time 0.95s for 9×9 spheres and cutoff number 3. Comparison between analytical and numerical solutions with (a) Δt=0.003125s and Δt=0.00625s and (b) Δt=0.0125s and Δt=0.025s.*

We have observed by numerical examples: the characteristic behavior due to insufficient spatial or temporal discretization indicates which type of refinement is necessary to improve the approximate solution for the method of finite spheres. In particular, if the solution has spurious oscillations, then spatial refinement, either *h*-type or *p*-type, is required, and if the solution exhibits dispersion and dissipations errors, then a decrease in the time step size is necessary.

3.4.1.2 Wave propagation time step size estimate

The spatial and temporal discretizations should be related to each other by the wave speed [82]. In order to estimate the numerical dispersion property as a function of CFL number, a very complicated calculation is usually required [82]. However, without carrying out such complicated calculations, Ref. [6] presents a simple approach for choosing an appropriate time step size for various time integration methods [6]. According to [6], we can assume that if the critical wavelength to be represented is L_w, then the time for the wave to travel this distance is

$$t_w = \frac{L_w}{c} \tag{3.51}$$

where c is the wave speed. We postulate that if n steps are required to approximate the traveling wave accurately, then we can obtain the appropriate time step size for the traveling wave by

$$\Delta t = \frac{t_w}{n} \tag{3.52}$$

The time step size depends on the time integration scheme used [6]. We assume that the smallest wavelength that the method of finite spheres can approximate accurately is $\lambda_p = 2r_I/p$, where p is the cutoff number and r_I is the radius of the sphere. Here we assume that the critical wavelength is $L_w = \lambda_p = 2r_I/p$. Then we have

$$\Delta t = \frac{t_w}{n} = \frac{L_w}{cn} = \frac{2r_I}{pcn} \tag{3.53}$$

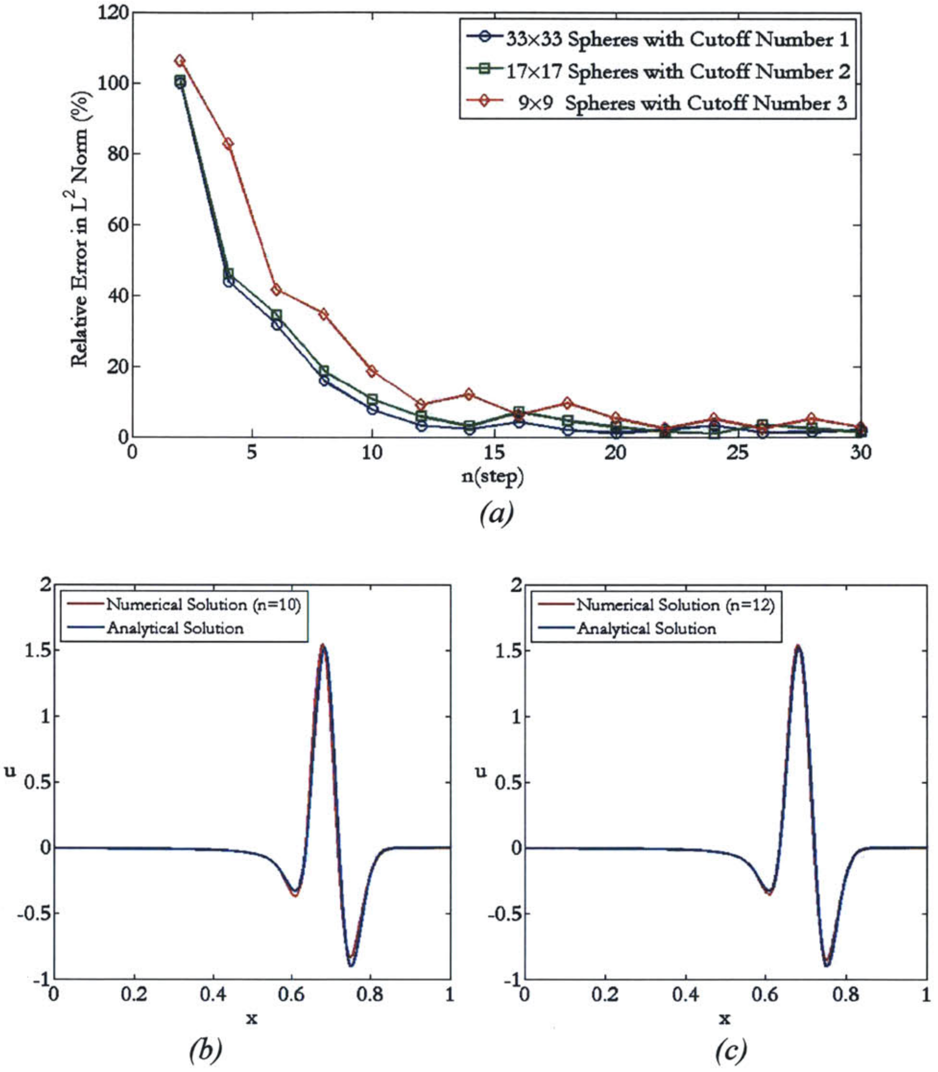

(a)

(b) *(c)*

Fig. 3.16: *(a) Percentage relative error in the L^2 norm for increasing n. Comparison between analytical and numerical solutions for 17×17 spheres with cutoff number 2 for (b) n=10 and (c) n=12.*

Fig. 3.16(a) shows the percentage relative error in the L^2 norm for increasing *n* for different sphere size/cutoff number combinations. It is evident that for all such combinations, an increase in *n* reduces the relative error. Since the time step size affects the computational cost of the method, it is practical to choose a time step size that provides a reasonably accurate solution without significantly increasing the computational cost associated with calculating the solution.

Certain unexpected trends arise from the results of *Fig. 3.16(a)* that can be explained without difficulty. First, we observe that the errors for cutoff number 1 and 2 are generally lower than that for cutoff number 3. This can be explained by examining the smallest wavelength λ_p for each of these cases. The time step size is related to the smallest wavelength, which is a function of both the cutoff number and the sphere radius.

By calculating the smallest wavelengths for the three cases, it is evident that the 9×9 sphere discretization with cutoff number 3 combination gives the larger of the smallest wavelengths for the three cases, resulting in slightly less accurate solutions, due to a larger time step size. Furthermore, we observe that as n increases, the error gradually decreases but with small fluctuations. This can be explained by the fact that the percentage relative error is calculated for the response at time 0.95s, but based on the time step size used, the approximate solution used in the error estimate may not precisely coincide with this time.

The generally accepted value for number of time steps per wavelength necessary to have an accurate solution is 10 steps. *Fig. 3.16(b)* illustrates the solution for n=10 and *Fig. 3.16(c)* for n=12, both for cutoff number 2 with the 17×17 sphere discretization. The percentage relative error in the L^2 norm is 10.5% for n=10 and 5.8% for n=12. Therefore, for an engineering approximation, we can say that n=12 provides a reasonably accurate solution. Thus, we recommend using this value for solving two-dimensional problems using the Bathe time integration method.

3.4.1.3 Computational cost

Table 3.1: Computational times (in seconds) measured for the enriched method of finite spheres.

	Method	Method of finite spheres					
	Discretization	9×9(p=3)		17×17 (p=2)		33×33 (p=1)	
	# of DOFs	3136		6400		9216	
	Int. Rule	4×13×13		4×9×9		4×6×6	
	Int. Points	39528		67048		113256	
	Time step size	0.003125s	0.00625s	0.003125s	0.00625s	0.003125s	0.00625s
	Percentage relative error	4.53%	12.01%	2.82%	10.58%	2.11%	7.80%
Time	Calculation of stiffness matrix	28.00s	23.33s	13.38s	13.36s	7.61s	7.53s
	Factorization of stiffness matrix	2.02s	1.95s	3.77s	3.77s	2.86s	2.91s
	Dynamic analysis	22.27s	11.47s	41.39s	20.72s	53.88s	27.39s
	Total solution	52.34s	36.75s	58.66s	37.85s	64.56s	37.83s

Table 3.1 shows the computational cost for the scalar wave propagation problem as seen in *Fig. 3.12*. The method was implemented in FORTRAN 77 and followed the format of the program, STAP (STatic Analysis Program) [6]. Relative error in L^2 norm was used to measure the accuracy. Although the error seems to be large when it says 12.01%, 10.58%, 7.8%, if we look at the *Fig. 3.15(a)* we can see that the error is almost negligible.

Although the smallest number of integration points were used for constructing the stiffness matrix for the case of 9×9 spheres and cutoff number 3, it took the longest time to get it. It is because 49 functions are included per a sphere for the case of cutoff number 3 so that constructing the stiffness matrix per a sphere is the most expensive.

Table 3.2: Computational times (in seconds) measured for the finite element method.

	Method	Finite element method (4-node)			
	Discretization	80×80		160×160	
	# of DOFs	6400		25600	
	Int. Rule	2×2		2×2	
	Int. Points	25600		102400	
	Time step size	0.00625s (CFL=0.5)	0.0125s (CFL=1)	0.003125s (CFL=0.5)	0.00625s (CFL=1)
	Percentage relative error	21.26%	12.73%	5.59%	3.27%
Time	Calculation of stiffness matrix	0.02s	0.03s	0.08s	0.09s
	Factorization of stiffness matrix	0.16s	0.16s	2.31s	2.44s
	Dynamic analysis	12.14s	5.94s	107.67s	57.22s
	Total solution	12.32s	6.13s	110.06s	59.75s

For comparing the solution time with the finite element method, *Table 3.2* shows the computational time for 4-node finite element method is used. Bathe time integration method is used for each case. In Bathe time integration method, when we choose the time step size corresponding to CFL = 1 then we are able to obtain the optimal accuracy [82]. Indeed, 80×80 mesh with the time step size of $\Delta t = 0.0125\text{s}$ gives an accurate result which is 12.01% in relative error in L^2 norm and it takes only 6.13s. However, the disadvantage of using an uniform mesh of 4-node elements is that when we use a smaller time step size than the time step size corresponding to CFL = 1, the solution accuracy becomes worse. We can observe this phenomenon from *Table 3.2* in which when smaller time step sizes were used, the solution errors increased for both cases (80×80 mesh and 160×160 mesh) but for the method of finite spheres, the solution gets more accurate with smaller time step sizes.

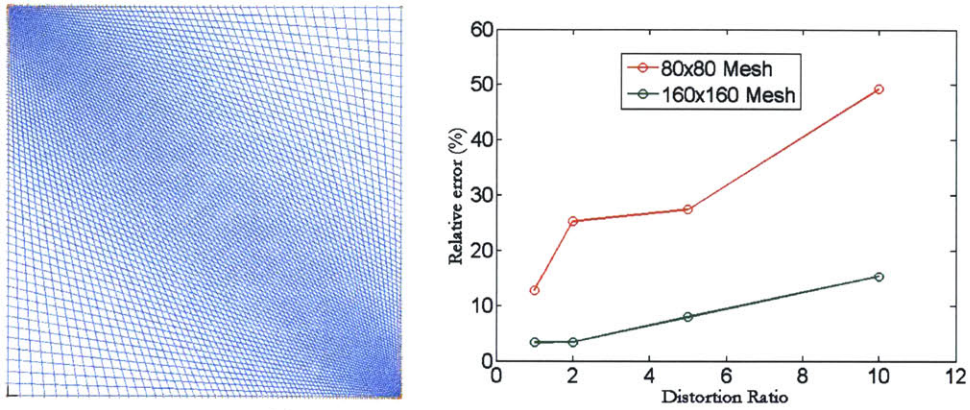

(a) *(b)*

Discretization	80×80				160×160			
Distortion ratio	1	2	5	10	1	2	5	10
Percentage relative error	12.73%	25.20%	27.36%	49.20%	3.27%	3.32%	7.90%	15.26%

Fig. 3.17: *(a) 80×80 mesh of 4-node elements with distortion ratio = 10 and (b) Relative error in L^2 norm for the finite element method.*

In addition, in realistic situation, using distorted elements are inevitable [6]. *Fig. 3.17* shows the distorted 80×80 mesh with the distortion ratio 10 as an example. The distortion ratio is defined as the ratio of the longest side length of any the elements over the shortest side length of any of the elements in the domain [6]. *Fig. 3.17(b)* shows the relative errors in L^2 norm for the distorted 80×80 mesh and the distorted 160×160 mesh. When the distortion ratio is 2, the solution error increased from 12.73% to 25.2% for the case of 80×80 mesh, while the error increased from 3.27% to 3.32% for the case of 160×160 mesh, which means that inevitably, the 80×80 mesh is more sensitive to distortion than the 160×160 mesh.

The advantage of using the method of finite spheres is that it does not have the issue of having distorted elements in the problem domain. The solution accuracy for the 160×160 mesh with the distortion ratio = 5 is 7.9% and when 33×33 spheres with cutoff number 1 are used the solution accuracy is 7.8%. When these two cases are compared, the method of finite spheres requires less computational time than the finite element method.

The solution accuracies (the computational costs) are 4.53% (52.34s), 2.82% (58.66s) and 2.11% (64.56s) respectively for the cases of 9×9, 17×17, and 33×33 spheres with the time step size $\Delta t = 0.003125\text{s}$ and is 3.27% (59.75s) for the case of an uniform 160×160 mesh with the time step size $\Delta t = 0.00625\text{s}$. All cases are almost the same in the computational costs and solution accuracies.

3.4.2 Scattered waves by an array of rigid circular cylinders

In this Section we consider the problem of scattered waves due to an array of rigid circular cylinders in an infinite medium. Such problems are commonly encountered in the construction of ocean structures such as oil rigs which consist of a number of tension-legs anchored to the bottom of the ocean. In constructing such structures, the interaction between water waves and the circular cylinders is of interest [83, 84].

First, consider the problem of scattered waves by a single rigid circular cylinder. A plane wave traveling in the x-direction strikes the circular cylinder and the wave scatters around, and radiates away, from the cylinder. The schematic illustrating this response is shown in *Fig. 3.18*. The analytical solution for the scattered waves is given by

$$u(r,\theta) = -\sum_{n=0}^{\infty} i^n \rho_n \frac{J_n'(ka)}{H_n'(ka)} H_n(kr)\cos n\theta \qquad (3.54)$$

where ρ_n is defined by $\rho_0 = 1$ and $\rho_n = 2$ for all $n \geq 1$, r and θ are the polar coordinates measured from the center of the circular cylinder, H_n is the Hankel function, and J_n is the Bessel function, with the prime (') indicating differentiation. The radius of the circular cylinder is $a = 1$ while the other parameters are scaled with respect to a. The wavenumber is $ka = 6\pi$.

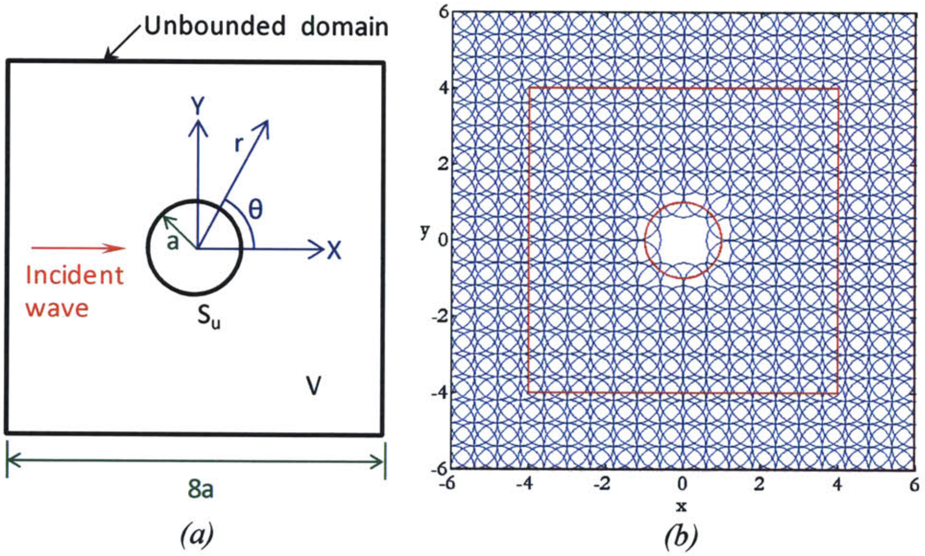

Fig. 3.18: *(a) Problem description and (b) discretization of the computational domain. 21x21 spheres are arranged regularly and the spheres whose centers are located inside the circular cylinder have been removed. The computational domain is edged with a perfectly matched layer to model the radiation boundary condition.*

As before, the percentage relative error in the L^2 norm is used to measure the accuracy of the numerical solution. Since the analytical solution consists of an infinite number of terms, we adopt n from 0 to 20 as our reference analytical solution. Eq. (3.54) for $n = 0,\ldots,20$ is applied to the boundary of the circular cylinder through the Dirichlet boundary conditions [83, 84]. The radiation boundary condition in an infinite domain is replaced by a perfectly matched layer [71]. Using either an absorbing boundary condition or a perfectly matched layer to simulate the unbounded physical domain results in some numerical errors, but we assume that the error is negligible [83, 84].

Fig. 3.18(b) illustrates the discretization of the computational domain using a sequence of regularly arranged spheres. A 21×21 sphere discretization and the spheres whose centers are located inside the circular cylinder are removed. Discretization of the domain is simple and inexpensive for the method of finite spheres. For the finite element method, constructing a good quality mesh is costly. The nodes have to coincide with the boundaries of complicated geometries, often leading to distorted elements [63]. Distorted elements are a common problem for the finite element method resulting in loss of accuracy and reliability of the solution. However, since nodes do not need to coincide with the boundaries of the computational domain for the method of finite spheres, discretization is straightforward and element distortion is never an issue.

Fig. 3.19 provides plots of the real part of the solution for the scattered numerical waves using cutoff numbers 1-3. The results obtained using cutoff number 1 are quite poor, due to inadequate spatial discretization within the perfectly matched layer. Consequently, there is a reflected wave, and *Fig. 3.19(a)* shows the result of the scattered wave deteriorated by this reflected wave which was not completely absorbed by the perfectly matched layer. The results obtained using cutoff number 3 are in good agreement with the analytical solution [71].

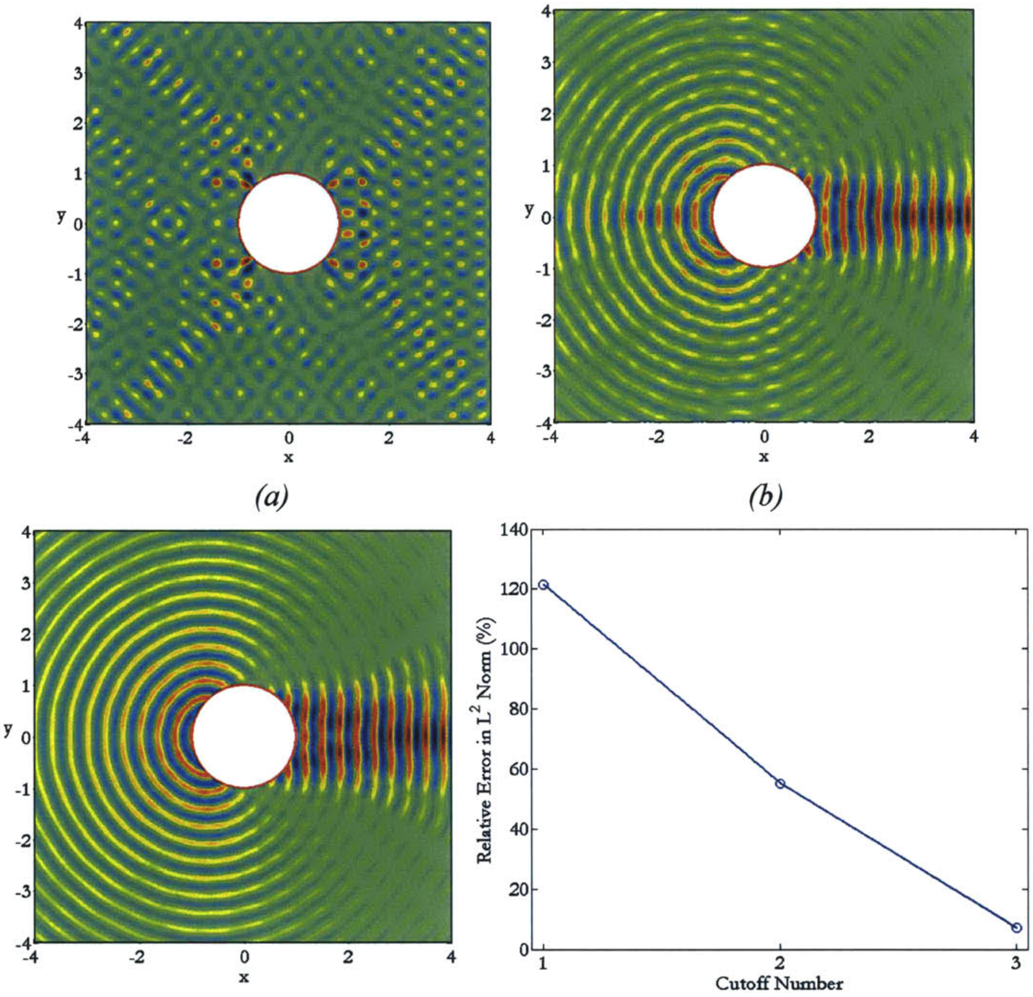

(a) (b)

(c) (d)

Fig. 3.19: *Real part of numerical solution with (a) cutoff number 1, (b) cutoff number 2, (c) cutoff number 3, and (d) percentage relative error in the domain not including the PML in the* L^2 *norm as a function of the cutoff number.*

Now, consider the problem of wave scattering due to an array of rigid circular cylinders [83, 84]. In the multiple scattering problem scenario, the wave scattered by one cylinder strikes another cylinder and again scatters [83, 84]. The exact solution is given by

$$u(r,\theta)=\sum_{j=1}^{N}\sum_{q=-M}^{+M}B_q^j\frac{J_q'(ka_j)}{H_q'(ka_j)}H_q(kr_j)\exp(iq\theta_j) \tag{3.55}$$

where a_j is the radius of the jth cylinder [83, 84]. The unknown coefficients B_q^j are found by solving the equations

$$\begin{aligned}&B_l^p+\sum_{j=1,j\neq p}^{N}\sum_{q=-M}^{+M}B_q^j\frac{J_q'(ka_j)}{H_q'(ka_j)}\exp[i(q-l)\alpha_{jp}]H_{q-l}(kR_{jp})\\&=-\exp[i(kx_p+\frac{\pi}{2}l)]\end{aligned} \tag{3.56}$$

where $p=1,...,N$ and $l=-M,...,M$.

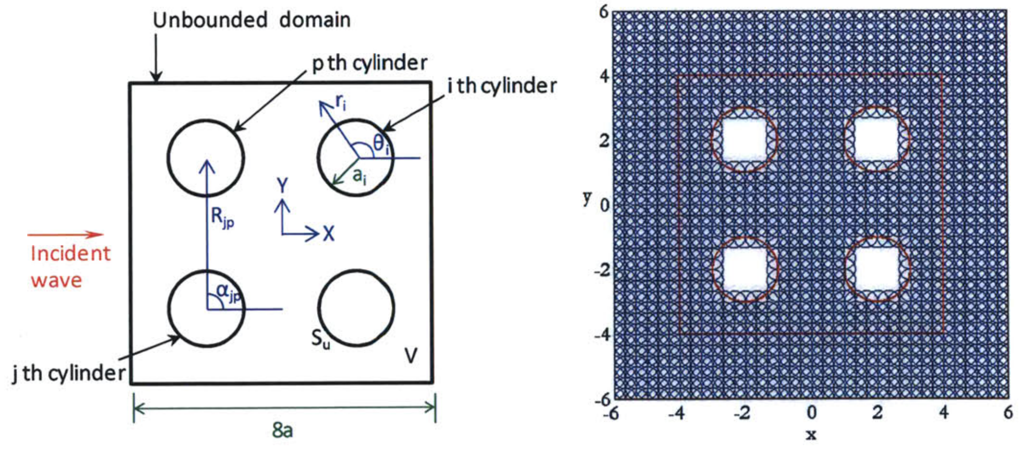

(a) *(b)*

Fig. 3.20: *(a) Problem description and (b) discretization of the computational domain. 37×37 spheres are arranged regularly and the spheres whose centers are located inside the circular cylinders have been removed. The computational domain is edged with a perfectly matched layer to model the radiation boundary condition.*

The schematic diagram in *Fig. 3.20* illustrates the parameters α_{jp} and R_{jp}. Refs. [83, 84] state that better accuracy is obtained by increasing M, and unless the cylinders are too closely spaced, $M = 6$ provides a reasonably accurate solution. Here, we adopt $M = 10$, which has been found to provide a good quality solution.

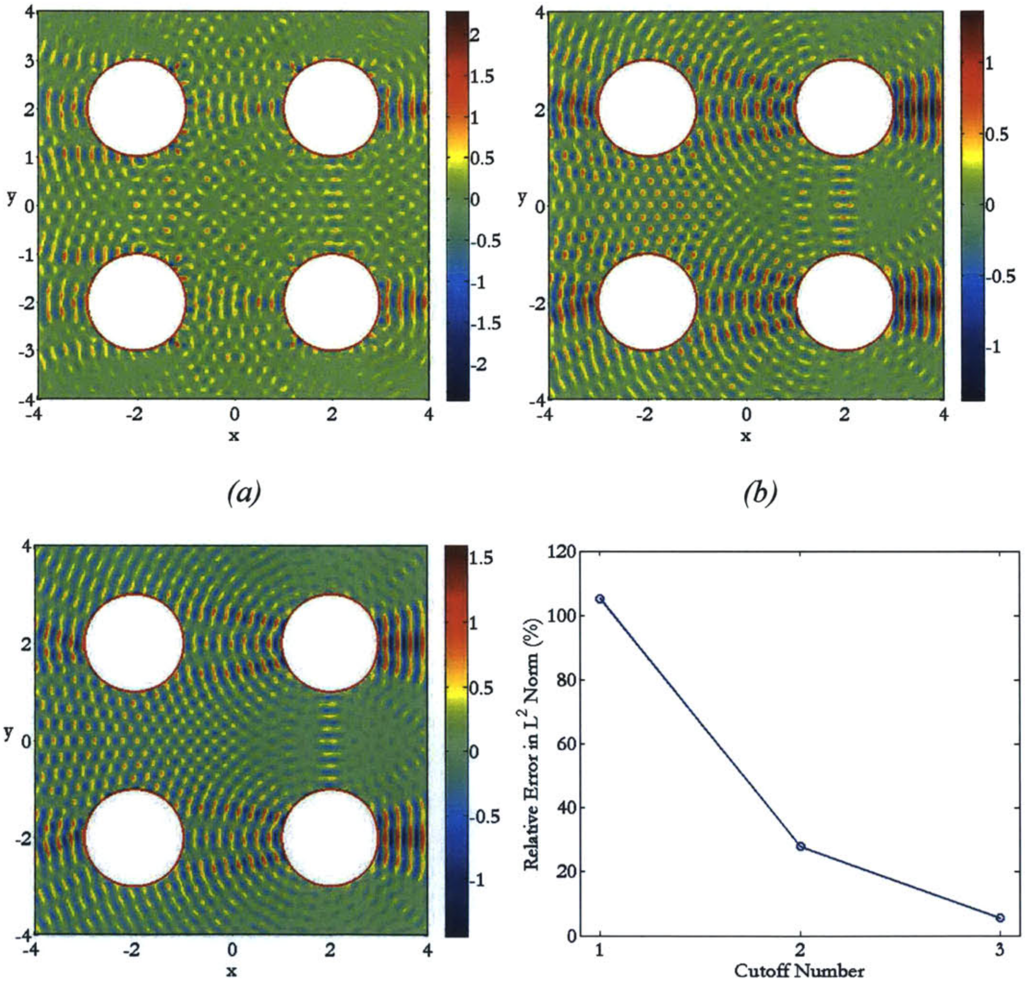

(a) *(b)*

(c) *(d)*

Fig. 3.21: *Real part of numerical solution with (a) cutoff number 1, (b) cutoff number 2, (c) cutoff number 3, and (d) percentage relative error in the L^2 norm as a function of the cutoff number.*

An array of four rigid cylinders is located within the problem domain and a plane wave is incident in the positive x-direction, as shown in *Fig. 3.20*. The problem domain is discretized with 37×37 spheres, and as with the single cylinder case, the spheres whose centers located inside the cylinders are removed. A Dirichlet boundary condition is prescribed on the boundaries of the cylinders and a perfectly matched layer is used along the edges of the domain boundary [71]. The wave number is $ka = 8\pi$. *Fig. 3.21* provides plots of the real part of the solution for the scattered numerical waves using cutoff numbers 1-3, and the results obtained using cutoff number 3 provide the best solution and are in good agreement with the analytical solution [71].

3.4.3 Two-dimensional elastic wave propagation problem

Wave motions appear in nearly every branch of physics, and there are numerous examples. Wave propagation deals with many ways in which waves can travel. Examples of waves found in elastic media include primary waves (P-waves) which are longitudinal pressure waves, secondary waves (S-waves) which are transverse shear waves, and Rayleigh waves which are a type of surface wave that travel near the surface of solids. In this Section, we consider the response of elastic wave propagations within a semi-infinite problem domain.

Consider an elastic medium with P-wave velocity, $v_p = 3200\,\mathrm{m/s}$, S-wave velocity, $v_s = 1847.5\,\mathrm{m/s}$, and mass density, $\rho = 2200\,\mathrm{kg/m^3}$ [71]. The problem domain is 4000m×2000m and will be discretized with a 51×26 sphere discretization, using the cutoff number 2. An absorbing boundary condition is used to model that the problem domain is unbounded. The forcing function is a Ricker wavelet with central frequency 10Hz, vertically imposed at the surface at (x,y)=(2000m,2000m). The Bathe time integration method is used with a time step size of $\Delta t = 0.0008\text{s}$ [82]. The total duration of the numerical simulation is 1s. *Fig. 3.22* shows the wave profiles at time t = 0.74s, where the P-, S-, and Rayleigh waves can be identified [71]. *Fig. 3.23* shows a comparison between the analytical and numerical solutions at two receivers, one located at $(x, y) = (2640\text{m}, 2000\text{m})$ and the other at $(x, y) = (3280\text{m}, 2000\text{m})$.

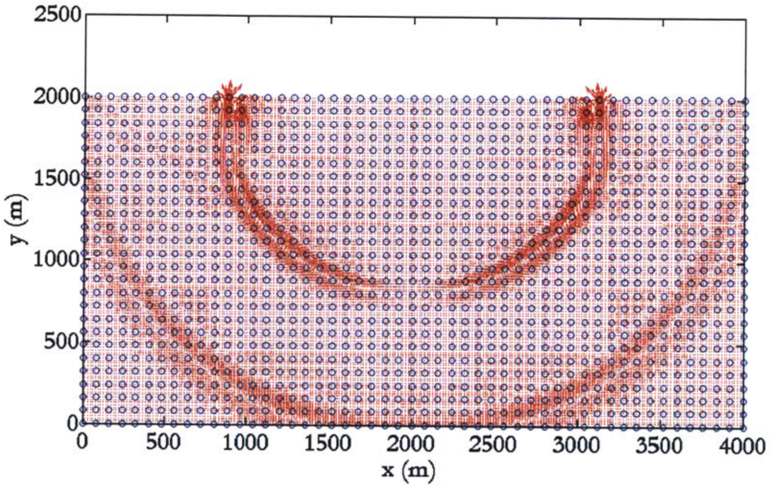

Fig. 3.22: *Displacement field at time t=0.74s.*

The simulation of the traveling Rayleigh wave is a common benchmark problem. The wave propagates along the surface, so this problem is used to test whether the numerical method is capable of accurately approximating this free-surface boundary condition [35]. Some meshless methods exhibit problems in accurately approximating the solution along this boundary condition due to the nature of how interpolation functions are constructed [28].

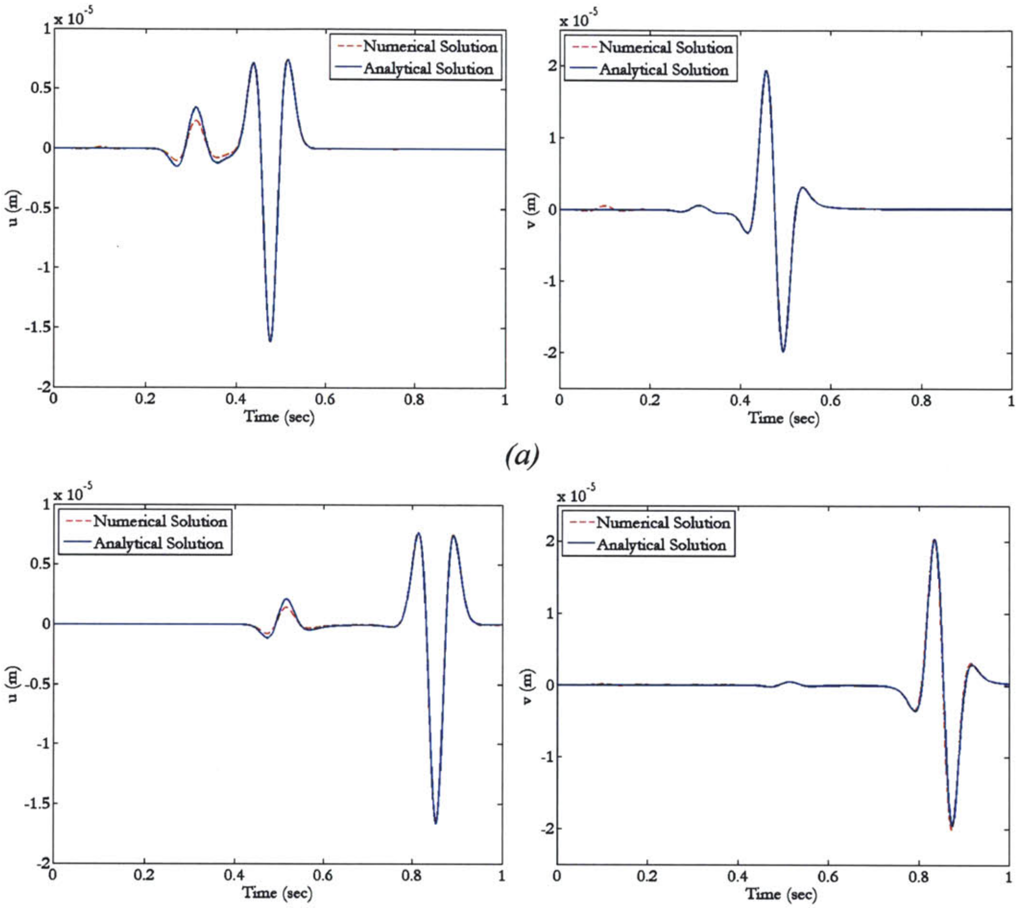

(a)

(b)

***Fig. 3.23**: Displacement variations in x-direction and y-direction at the two receivers. Numerical solutions are compared with analytical solutions (a) at 640m from the source and (b) at 1280m from the source.*

Fig. 3.23 shows that the numerical results for the method of finite spheres are in agreement with the analytical solutions for the two receivers. This verifies that the proposed algorithm exhibits accurate results along the free-surface boundary condition and is capable of matching the analytical results with relatively few degrees of freedom. Furthermore, the solutions do not exhibit any signs of spurious oscillations or dispersion and dissipation, indicating that the spatial and temporal discretizations are sufficient for the given frequency of loading. However, in *Fig. 3.23(a)*, we observe that the height of the numerical solution for the P-wave is slightly lower than that of the analytical solution. This is probably due to the fact that the analytical solution models the loading as a point load.

3.4.4 Two-dimensional viscoelastic wave propagation problem

The characteristics of wave propagations in an actual body as compared to an idealized linear elastic body can be different due to friction effects [74 - 77]. The viscous property in actual media causes dispersion and attenuation in the traveling waves [74 - 77]. In this Section, we consider wave propagation in a two-dimensional viscoelastic body. The problem domain is 2000m×2000m and will be discretized with a 33×33 sphere discretization and interpolated with cutoff number 3. The Bathe time integration method is used with a time step size of $\Delta t = 0.0004$s. The Ricker wavelet vertically applied at the center of the problem domain is given by

$$F(t) = (1 - 2\pi^2 \hat{f}^2 (t - t_0)^2) \exp(-\pi^2 \hat{f}^2 (t - t_0)^2) \qquad (3.57)$$

where the time shift is t_0 = 0.06s and the cutoff frequency is $\hat{f} = 50\text{Hz}$. The viscoelastic medium has P-wave velocity, $v_p = 3000\,\text{m/s}$, S-wave velocity, $v_s = 2000\,\text{m/s}$, and mass density, $\rho = 2000\,\text{kg/m}^3$. We define the quality factors as Q_p = 26 for P-wave attenuation and Q_s = 19 for S-wave attenuation. Since the quality factor for the S-wave is lower than that for the P-wave, we anticipate that the S-wave will be attenuated more than the P-wave as waves propagate through the viscoelastic medium. The analytical solution for this problem can be obtained from Ref. [74].

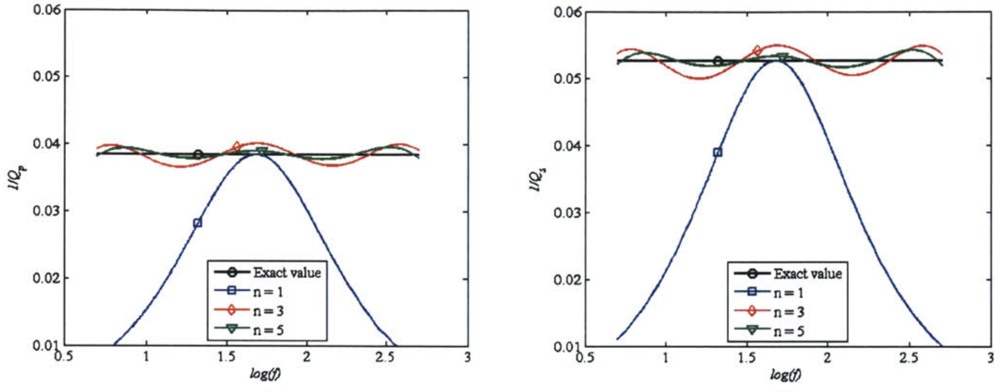

(a) *(b)*

Fig. 3.24: *Determination of quality factors using generalized Maxwell model: (a) Q_p=26 and (b) Q_s=19 as a function of relaxation mechanics.*

Fig. 3.24 illustrates the approximations for the quality factors using the generalized Maxwell body models. The black horizontal lines indicate the exact quality factors $1/Q_p$ and $1/Q_s$, while the remaining lines are approximations of the quality factors for increasing number of relaxation mechanisms n. As the number of relaxation mechanisms increases, the error decreases, but the computational cost increases. Therefore, we have chosen to use $n = 3$ relaxation mechanisms.

Fig. 3.25 shows the displacement fields in the viscoelastic body at time t = 0.22s and t = 0.32s. *Fig. 3.26* compares numerical and analytical time histories at the position $x = y$ = 1500m, for both the x- and y-direction. Note that for the elastic wave case, there would be no attenuation and the S-wave would be much stronger than the P-wave. Here, for the viscoelastic case, we observe that the amplitude of the S-wave is smaller than that of the P-wave due to stronger attenuation on the S-wave. The numerical solution is in good agreement with the exact solution, but a slight error is noticeable. This is due to an insufficient spatial discretization, so in order to obtain a more accurate solution, smaller sphere sizes are needed. However, in viscoelastic wave modeling, having a smaller sphere size leads to large increases in the computational cost because the element stresses accounting for the viscous parts which on unloading disappear have to be updated at each integration point within each sphere at every time step.

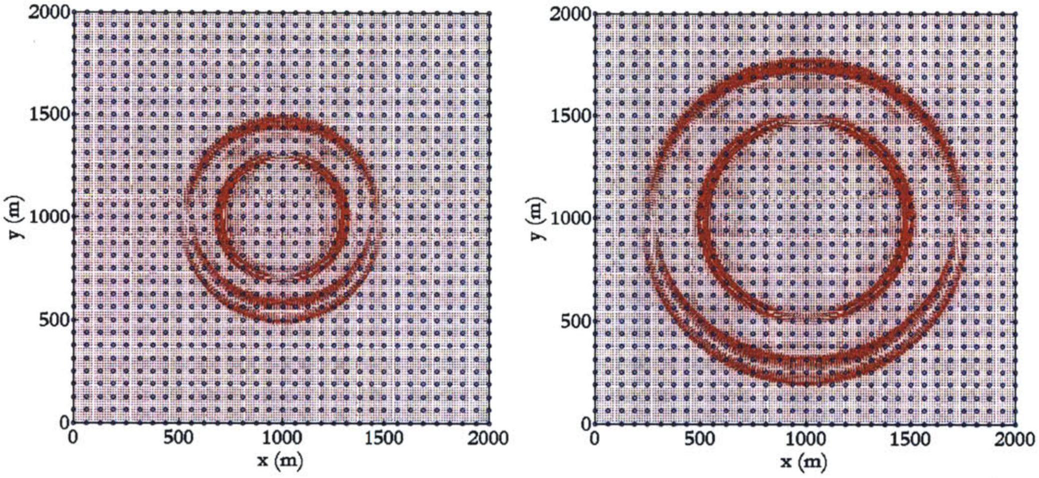

(a) (b)

Fig. 3.25: *Displacement distributions in viscoelastic body at (a) t=0.22s and (b) t=0.32s due to a vertical force.*

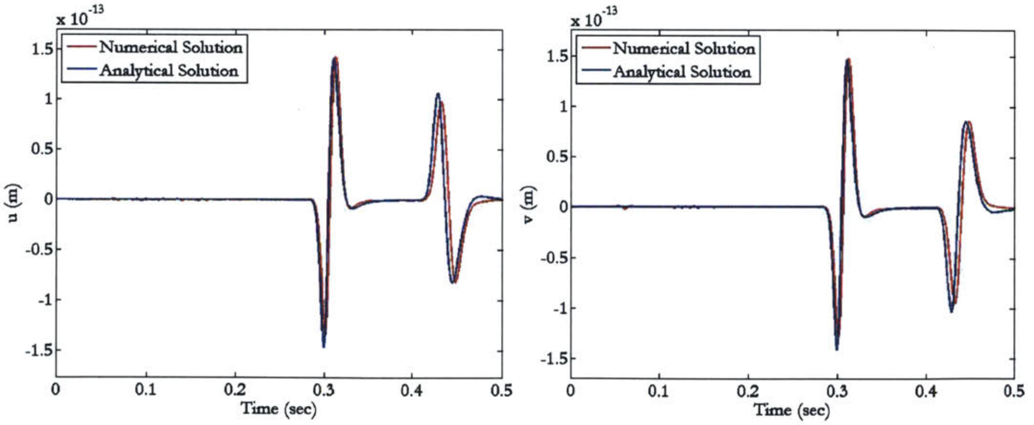

(a) (b)

Fig. 3.26: *Displacement variations at x = y = 1500m compared with analytical solutions in (a) x-direction and (b) y-direction.*

Chapter 4

Concluding remarks

The topic of this thesis is the development of effective numerical schemes for the solution of wave propagation problems. In Chapter 2, we proposed an enriched finite element method for solving wave propagation problems in solids. The method is used as the traditional finite element procedures, but simply additional degrees of freedom (corresponding to the harmonic terms) are added to the nodes of lower- or higher- order standard elements. In many cases, only real arithmetic is employed. We have illustrated the use of the method in two-dimensional solutions, but the concept directly applies to three-dimensional solutions as well.

The method does not embed 'a priori' specific wave solutions, instead, the procedure is a general scheme that directly and automatically gives the 'best' solution possible in the assumed solution space – just like the standard displacement-based finite element method by its minimization properties [6]. Therefore, like in the standard finite element method, the assumed solution space must be rich enough to obtain an accurate approximation to the exact solution, and this means that the mesh must be fine enough and the number of harmonics used must be large enough. In this way, based on our numerical experiences thus far, accurate solutions can be obtained with reasonable meshes and solution data.

The method can be used with no enrichment functions (thus being the traditional finite element method) and thereafter harmonics to enrich the solution space can be selectively added, in an hierarchical manner [85]. This makes the method flexible and attractive for practical usage.

In Chapter 3, we proposed the method of finite spheres enriched with trigonometric functions, and using the Bathe time integration algorithm, for the solution of wave propagation problems in elastic and viscoelastic media. Advantages of the method of finite spheres are that it allows the problem domain to be discretized and boundary conditions to be incorporated without difficulty, which has been verified by way of several examples. The use of trigonometric functions in the definition of the interpolation functions to reproduce the wave fields in various media has been evaluated against analytical solutions. Furthermore, the convergence behavior of the proposed scheme was demonstrated in several examples by using *hp*-refinement for the spatial discretization.

A new strategy for addressing the numerical integration associated with the method of finite spheres was presented and tested. The convergence study of the strain energy for the cantilever plate problem showed the efficiency and reliability of the proposed numerical integration scheme.

Still under development, the method of finite spheres has much potential with many avenues to investigate. Future work should include the development of efficient techniques for node generation, selecting the radii of the spheres for acceptable accuracy, and computing the intersections of spheres with general boundaries [78]. Also, the numerical integration for irregular nodal arrangements should be studied in conjunction with effective means of arranging nodes for a complicated domain. The proposed scheme used the Bathe implicit time integration method for the solution of wave propagation problems. However, for extremely large-scale problems, an explicit time integration method has advantages and might reduce the computational effort significantly. Hence, further research should be pursued in order to develop the use of explicit time integration with the method of finite spheres.

Appendix

Formulation for linear viscoelasticity

The stress-strain relation in a linear viscoelastic medium can be defined as

$$\tau_{ij}(t)=\int_{-\infty}^{t}\psi_{ijkl}(t-\tau)\dot{\varepsilon}_{kl}(\tau)\,\mathrm{d}\tau \tag{A.1}$$

where ψ_{ijkl} is the tensor describing the behavior of viscoelasticity. In an isotropic viscoelastic body, the stress-strain relation can be expressed as

$$\tau_{ij}(t)=\delta_{ij}\int_{-\infty}^{t}\kappa(t-\tau)\dot{\varepsilon}_{kk}(\tau)d\tau+2\int_{-\infty}^{t}\mu(t-\tau)[\dot{\varepsilon}_{ij}(\tau)-\frac{1}{3}\delta_{ij}\dot{\varepsilon}_{kk}(\tau)]d\tau \tag{A.2}$$

To make (A.2) easy to read, we use the symbol * for the convolution, then rewrite (A.2) as

$$\tau_{ij}(t)=\delta_{ij}\kappa(t)*\dot{\varepsilon}_{kk}(t)+2\mu(t)*\dot{\varepsilon}_{ij}(t)-\frac{2}{3}\delta_{ij}\mu(t)*\dot{\varepsilon}_{kk}(t) \tag{A.3}$$

According to the commutative property of the convolution, we can change Eq. (A.3) as

$$\tau_{ij}(t)=\delta_{ij}\dot{\kappa}(t)*\varepsilon_{kk}(t)+2\dot{\mu}(t)*\varepsilon_{ij}(t)-\frac{2}{3}\delta_{ij}\dot{\mu}(t)*\varepsilon_{kk}(t) \tag{A.4}$$

We define $\dot{\kappa}(t)$ and $\dot{\mu}(t)$ as

$$M^{\kappa}(t)=\dot{\kappa}(t),\ M^{\mu}(t)=\dot{\mu}(t) \tag{A.5}$$

and rewrite Eq.(A.4) as

$$\tau_{ij}(t)=\delta_{ij}M^{\kappa}(t)*\varepsilon_{kk}(t)+2M^{\mu}(t)*\varepsilon_{ij}(t)-\frac{2}{3}\delta_{ij}M^{\mu}(t)*\varepsilon_{kk}(t) \tag{A.6}$$

We can compare Eq. (A.6) with the stress-strain relation of an elastic body. While the stress-strain relation of an elastic body is simply a linear relation with a constant elastic modulus, the stress-strain relation of a viscoelastic body is time dependent.

Using the Fourier transform and the inverse Fourier transform

$$F\{\kappa(t)\}=\int_{-\infty}^{\infty}\kappa(t)\exp(-i\omega t)\mathrm{d}t \text{ and } F^{-1}\{\mathrm{K}(\omega)\}=\frac{1}{2\pi}\int_{-\infty}^{\infty}\mathrm{K}(\omega)\exp(i\omega t)\mathrm{d}\omega \tag{A.7}$$

Eq. (A.6) gives

$$\tau_{ij}(\omega)=\delta_{ij}M^{\kappa}(\omega)\cdot\varepsilon_{kk}(\omega)+2M^{\mu}(\omega)\cdot\varepsilon_{ij}(\omega)-\frac{2}{3}\delta_{ij}M^{\mu}(\omega)\cdot\varepsilon_{kk}(\omega) \tag{A.8}$$

where

$$M^{\kappa}(\omega)=F\{M^{\kappa}(t)\}=F\{\dot{\kappa}(t)\},\ M^{\mu}(\omega)=F\{M^{\mu}(t)\}=F\{\dot{\mu}(t)\} \text{ and}$$

$$\dot{\kappa}(t)=F^{-1}\{M^{\kappa}(\omega)\},\ \dot{\mu}(t)=F^{-1}\{M^{\mu}(\omega)\} \tag{A.9}$$

are the frequency-dependent moduli.

Using the Fourier transform property, we have

$$\kappa(t)=F^{-1}\{\frac{M^{\kappa}(\omega)}{i\omega}\} \text{ and } \mu(t)=F^{-1}\{\frac{M^{\mu}(\omega)}{i\omega}\} \tag{A.10}$$

While comparing Eq. (A.8) with Eq. (A.2), we notice that computing the linear viscoelasticity in the frequency-domain is much easier than in the time-domain. We simply replaced the real and time-dependent moduli in Eq.(A.2) with the complex and frequency-dependent ones in Eq.(A.8).

We obtain the frequency-dependent moduli, $M^{\kappa}(\omega)$ and $M^{\mu}(\omega)$ using the generalized Maxwell body shown in *Fig. A.1,*

$$M^{\kappa}(\omega)=\kappa_R+\sum_{l=1}^{n}\frac{i\kappa Y_l^{\kappa}\omega}{\omega_l+i\omega} \text{ and } M^{\mu}(\omega)=\mu_R+\sum_{l=1}^{n}\frac{i\mu Y_l^{\mu}\omega}{\omega_l+i\omega} \tag{A.11}$$

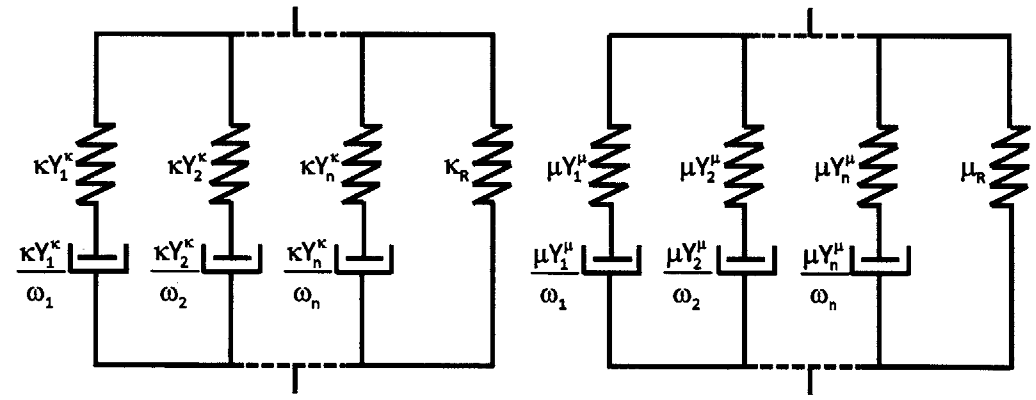

(a) *(b)*

***Fig. A.1:** Schematic of the generalized Maxwell body for (a) the complex viscoelastic bulk modulus and (b) the complex viscoelastic shear modulus.*

From Eq. (A.11), we calculate the relaxed and unrelaxed bulk moduli with

$$M_R^\kappa = \lim_{\omega\to 0} M^\kappa(\omega) = \lim_{\omega\to 0}(\kappa_R + \sum_{l=1}^{n} \frac{i\kappa Y_l^\kappa \omega}{\omega_l + i\omega}) = \kappa_R \text{ and}$$

$$M_U^\kappa = \lim_{\omega\to\infty} M^\kappa(\omega) = \lim_{\omega\to\infty}(\kappa_R + \sum_{l=1}^{n} \frac{i\kappa Y_l^\kappa \omega}{\omega_l + i\omega}) = \kappa_R + \kappa\sum_{l=1}^{n} Y_l^\kappa \tag{A.12}$$

In the same way, we get the relaxed and unrelaxed shear moduli,

$$M_R^\mu = \mu_R \text{ and } M_U^\mu = \mu_R + \mu\sum_{l=1}^{n} Y_l^\mu \tag{A.13}$$

where the unrelaxed bulk and shear moduli, M_U^κ and M_U^μ, are elastic bulk and shear moduli respectively so we have

$$\kappa = \kappa_R + \kappa\sum_{l=1}^{n} Y_l^\kappa \text{ and } \mu = \mu_R + \mu\sum_{l=1}^{n} Y_l^\mu \tag{A.14}$$

Using Eq. (A.10), we have

$$\kappa(t) = F^{-1}\left\{\frac{M^\kappa(\omega)}{i\omega}\right\} = F^{-1}\left\{\frac{\kappa_R}{i\omega} + \sum_{l=1}^{n} \frac{\kappa Y_l^\kappa}{\omega_l + i\omega}\right\} = \left[\kappa_R + \kappa\sum_{l=1}^{n} Y_l^\kappa \exp(-\omega_l t)\right]\cdot H(t) \text{ and}$$

$$\mu(t) = F^{-1}\left\{\frac{M^\mu(\omega)}{i\omega}\right\} = F^{-1}\left\{\frac{\mu_R}{i\omega} + \sum_{l=1}^{n} \frac{\mu Y_l^\mu}{\omega_l + i\omega}\right\} = \left[\mu_R + \mu\sum_{l=1}^{n} Y_l^\mu \exp(-\omega_l t)\right]\cdot H(t) \tag{A.15}$$

where $H(t)$ is the Heaviside unit step function.

Substituting $\kappa_R = \kappa - \kappa\sum_{l=1}^{n} Y_l^\kappa$ and $\mu_R = \mu - \mu\sum_{l=1}^{n} Y_l^\mu$ into (A.15), we have

$$\kappa(t)=\left[\kappa-\kappa\sum_{l=1}^{n}Y_l^{\kappa}(1-\exp(-\omega_l t))\right]\cdot H(t) \text{ and}$$

$$\mu(t)=\left[\mu-\mu\sum_{l=1}^{n}Y_l^{\mu}(1-\exp(-\omega_l t))\right]\cdot H(t) \qquad \text{(A.16)}$$

and obtain the time derivative of the relaxation function

$$\begin{aligned}M^{\kappa}(t)&=\dot{\kappa}(t)\\&=-\kappa\sum_{l=1}^{n}Y_l^{\kappa}\omega_l\exp(-\omega_l t)\cdot H(t)+\kappa\left[1-\sum_{l=1}^{n}Y_l^{\kappa}(1-\exp(-\omega_l t))\right]\cdot\delta(t) \text{ and}\\M^{\mu}(t)&=\dot{\mu}(t)\\&=-\mu\sum_{l=1}^{n}Y_l^{\mu}\omega_l\exp(-\omega_l t)\cdot H(t)+\mu\left[1-\sum_{l=1}^{n}Y_l^{\mu}(1-\exp(-\omega_l t))\right]\cdot\delta(t)\end{aligned} \qquad \text{(A.17)}$$

Inserting Eq. (A.17) into Eq. (A.6) we get

$$\begin{aligned}\tau_{ij}(t)&=-\delta_{ij}\kappa\int_{-\infty}^{t}\sum_{l=1}^{n}Y_l^{\kappa}\omega_l\exp(-\omega_l(t-\tau))\cdot H(t-\tau)\varepsilon_{kk}(\tau)d\tau\\&+\delta_{ij}\kappa\int_{-\infty}^{t}\left[1-\sum_{l=1}^{n}Y_l^{\kappa}(1-\exp(-\omega_l(t-\tau)))\right]\cdot\delta(t-\tau)\varepsilon_{kk}(\tau)d\tau\\&-2\mu\int_{-\infty}^{t}\sum_{l=1}^{n}Y_l^{\mu}\omega_l\exp(-\omega_l(t-\tau))\cdot H(t-\tau)\varepsilon_{ij}(\tau)d\tau\\&+2\mu\int_{-\infty}^{t}\left[1-\sum_{l=1}^{n}Y_l^{\mu}(1-\exp(-\omega_l(t-\tau)))\right]\cdot\delta(t-\tau)\varepsilon_{ij}(\tau)d\tau\\&+\frac{2}{3}\delta_{ij}\mu\int_{-\infty}^{t}\sum_{l=1}^{n}Y_l^{\mu}\omega_l\exp(-\omega_l(t-\tau))\cdot H(t-\tau)\varepsilon_{kk}(\tau)d\tau\\&-\frac{2}{3}\delta_{ij}\mu\int_{-\infty}^{t}\left[1-\sum_{l=1}^{n}Y_l^{\mu}(1-\exp(-\omega_l(t-\tau)))\right]\cdot\delta(t-\tau)\varepsilon_{kk}(\tau)d\tau\end{aligned} \qquad \text{(A.18)}$$

and with further manipulations, we have

$$\begin{aligned}\tau_{ij}(t) &= \delta_{ij}\kappa\varepsilon_{kk}(t) - \delta_{ij}\kappa\sum_{l=1}^{n} Y_l^{\kappa}\omega_l \int_{-\infty}^{t} \exp(-\omega_l(t-\tau))\cdot\varepsilon_{kk}(\tau)d\tau \\ &+2\mu\varepsilon_{ij}(t) - 2\mu\sum_{l=1}^{n} Y_l^{\mu}\omega_l \int_{-\infty}^{t} \exp(-\omega_l(t-\tau))\varepsilon_{ij}(\tau)d\tau \\ &-\frac{2}{3}\delta_{ij}\mu\varepsilon_{kk}(t) + \frac{2}{3}\delta_{ij}\mu\sum_{l=1}^{n} Y_l^{\mu}\omega_l \int_{-\infty}^{t} \exp(-\omega_l(t-\tau))\varepsilon_{kk}(\tau)d\tau\end{aligned} \qquad (A.19)$$

Here we define the function,

$$\zeta_l^{ij}(t) = \omega_l \int_{-\infty}^{t} \exp(-\omega_l(t-\tau))\cdot\varepsilon_{ij}(\tau)d\tau \qquad (A.20)$$

Finally, we have the stress-strain relation in the form,

$$\begin{aligned}\tau_{ij}(t) &= \kappa\varepsilon_{kk}(t)\delta_{ij} + 2\mu(\varepsilon_{ij}(t) - \frac{1}{3}\varepsilon_{kk}(t)\delta_{ij}) \\ &-\sum_{l=1}^{n}[\kappa Y_l^{\kappa}\zeta_l^{kk}(t)\delta_{ij} + 2\mu Y_l^{\mu}(\zeta_l^{ij}(t) - \frac{1}{3}\zeta_l^{kk}(t)\delta_{ij})]\end{aligned} \qquad (A.21)$$

Applying the time derivative to Eq.(A.20) we have

$$\begin{aligned}\dot{\zeta}_l^{ij}(t) &= \omega_l \frac{\mathrm{d}}{\mathrm{d}t} \int_{-\infty}^{t} \exp(-\omega_l(t-\tau))\cdot\varepsilon_{ij}(\tau)d\tau \\ &= \omega_l[-\omega_l \int_{-\infty}^{t} \exp(-\omega_l(t-\tau))\cdot\varepsilon_{ij}(\tau)d\tau + \varepsilon_{ij}(t)] \\ &= \omega_l[-\zeta_l^{ij}(t) + \varepsilon_{ij}(t)]\end{aligned} \qquad (A.22)$$

and

$$\dot{\zeta}_l^{ij}(t) + \omega_l\zeta_l^{ij}(t) = \omega_l\varepsilon_{ij}(t) \;\; ; \; l = 1,\ldots,n \; . \qquad (A.23)$$

In linear viscoelasticity, the time-domain stress-strain relation is defined with Eq. (A.21) and Eq. (A.23) using the generalized Maxwell body.

Manipulating Eq. (A.21) further we have

$$\tau_{ij}(t)=\begin{bmatrix}\kappa+\frac{4}{3}\mu & \kappa-\frac{2}{3}\mu & 0\\ \kappa-\frac{2}{3}\mu & \kappa+\frac{4}{3}\mu & 0\\ 0 & 0 & \mu\end{bmatrix}\begin{bmatrix}\varepsilon_{xx}(t)\\ \varepsilon_{yy}(t)\\ 2\varepsilon_{xy}(t)\end{bmatrix}$$

$$-\sum_{l=1}^{n}\begin{bmatrix}\kappa Y_l^{\kappa}+\frac{4}{3}\mu Y_l^{\mu} & \kappa Y_l^{\kappa}-\frac{2}{3}\mu Y_l^{\mu} & 0\\ \kappa Y_l^{\kappa}-\frac{2}{3}\mu Y_l^{\mu} & \kappa Y_l^{\kappa}+\frac{4}{3}\mu Y_l^{\mu} & 0\\ 0 & 0 & \mu Y_l^{\mu}\end{bmatrix}\begin{bmatrix}\zeta_l^{xx}(t)\\ \zeta_l^{yy}(t)\\ 2\zeta_l^{xy}(t)\end{bmatrix} \tag{A.24}$$

In Eq. (A.24), we have two distinct stresses. One is the elastic contribution and the other is the viscous contribution which on unloading disappears. We change the stress form as

$$\underline{\tau}=\underline{\tau}^{E}-\sum\nolimits_{l=1}^{n}\underline{\tau}^{Al} \tag{A.25}$$

Substituting $\kappa_R=\kappa-\kappa\sum\limits_{l=1}^{n}Y_l^{\kappa}$ and $\mu_R=\mu-\mu\sum\limits_{l=1}^{n}Y_l^{\mu}$ into (A.11) and with more manipulations, we have

$$\begin{aligned}M^{\kappa}(\omega) &= \kappa_R + \sum_{l=1}^{n} \frac{i\kappa Y_l^{\kappa}\omega}{\omega_l + i\omega} \\ &= (\kappa - \kappa\sum_{l=1}^{n} Y_l^{\kappa}) + \sum_{l=1}^{n} \frac{i\kappa Y_l^{\kappa}\omega}{\omega_l + i\omega} \\ &= \kappa[1 - \sum_{l=1}^{n} Y_l^{\kappa} + \sum_{l=1}^{n} \frac{iY_l^{\kappa}\omega}{\omega_l + i\omega}] \\ &= \kappa[1 - \sum_{l=1}^{n} \frac{Y_l^{\kappa}\omega_l + iY_l^{\kappa}\omega}{\omega_l + i\omega} + \sum_{l=1}^{n} \frac{iY_l^{\kappa}\omega}{\omega_l + i\omega}] \\ &= \kappa[1 - \sum_{l=1}^{n} \frac{Y_l^{\kappa}\omega_l}{\omega_l + i\omega}]\end{aligned}$$

and

$$\begin{aligned}M^{\mu}(\omega) &= \mu_R + \sum_{l=1}^{n} \frac{i\mu Y_l^{\mu}\omega}{\omega_l + i\omega} \\ &= (\mu - \mu\sum_{l=1}^{n} Y_l^{\mu}) + \sum_{l=1}^{n} \frac{i\mu Y_l^{\mu}\omega}{\omega_l + i\omega} \\ &= \mu[1 - \sum_{l=1}^{n} Y_l^{\mu} + \sum_{l=1}^{n} \frac{iY_l^{\mu}\omega}{\omega_l + i\omega}] \\ &= \mu[1 - \sum_{l=1}^{n} \frac{Y_l^{\mu}\omega_l + iY_l^{\mu}\omega}{\omega_l + i\omega} + \sum_{l=1}^{n} \frac{iY_l^{\mu}\omega}{\omega_l + i\omega}] \\ &= \mu[1 - \sum_{l=1}^{n} \frac{Y_l^{\mu}\omega_l}{\omega_l + i\omega}]\end{aligned} \tag{A.29}$$

and

$$\begin{aligned}M^{\kappa}(\omega) &= \kappa[1 - \sum_{l=1}^{n} \frac{Y_l^{\kappa}\omega_l(\omega_l - i\omega)}{(\omega_l + i\omega)(\omega_l - i\omega)}] \\ &= \kappa[1 - \sum_{l=1}^{n} \frac{Y_l^{\kappa}\omega_l^2 - iY_l^{\kappa}\omega_l\omega}{\omega_l^2 + \omega^2}]\end{aligned}$$

and

$$\begin{aligned}M^{\mu}(\omega) &= \mu[1 - \sum_{l=1}^{n} \frac{Y_l^{\mu}\omega_l(\omega_l - i\omega)}{(\omega_l + i\omega)(\omega_l - i\omega)}] \\ &= \mu[1 - \sum_{l=1}^{n} \frac{Y_l^{\mu}\omega_l^2 - iY_l^{\mu}\omega_l\omega}{\omega_l^2 + \omega^2}]\end{aligned} \tag{A.30}$$

We obtain the real and imaginary frequency-dependent moduli respectively as

$$\begin{aligned}\operatorname{Re} M^{\kappa}(\omega) &= \kappa[1 - \sum_{l=1}^{n} \frac{Y_l^{\kappa}\omega_l^2}{\omega_l^2 + \omega^2}] \\ \operatorname{Im} M^{\kappa}(\omega) &= \kappa\sum_{l=1}^{n} \frac{Y_l^{\kappa}\omega_l\omega}{\omega_l^2 + \omega^2}\end{aligned} \quad \text{and} \quad \begin{aligned}\operatorname{Re} M^{\mu}(\omega) &= \mu[1 - \sum_{l=1}^{n} \frac{Y_l^{\mu}\omega_l^2}{\omega_l^2 + \omega^2}] \\ \operatorname{Im} M^{\mu}(\omega) &= \mu\sum_{l=1}^{n} \frac{Y_l^{\mu}\omega_l\omega}{\omega_l^2 + \omega^2}\end{aligned} \tag{A.31}$$

Given the viscoelastic moduli, the quality factor is

$$\frac{1}{Q_{\kappa}(\omega)} = \frac{\operatorname{Im} M^{\kappa}(\omega)}{\operatorname{Re} M^{\kappa}(\omega)} = \frac{\sum_{l=1}^{n} \frac{Y_l^{\kappa}\omega_l\omega}{\omega_l^2 + \omega^2}}{1 - \sum_{l=1}^{n} \frac{Y_l^{\kappa}\omega_l^2}{\omega_l^2 + \omega^2}} \quad \text{and} \quad \frac{1}{Q_{\mu}(\omega)} = \frac{\operatorname{Im} M^{\mu}(\omega)}{\operatorname{Re} M^{\mu}(\omega)} = \frac{\sum_{l=1}^{n} \frac{Y_l^{\mu}\omega_l\omega}{\omega_l^2 + \omega^2}}{1 - \sum_{l=1}^{n} \frac{Y_l^{\mu}\omega_l^2}{\omega_l^2 + \omega^2}} \tag{A.32}$$

With further manipulations we have

$$Q_{\kappa}^{-1}(\omega) - Q_{\kappa}^{-1}(\omega)\sum_{l=1}^{n}\frac{Y_l^{\kappa}\omega_l^2}{\omega_l^2+\omega^2} = \sum_{l=1}^{n}\frac{Y_l^{\kappa}\omega_l\omega}{\omega_l^2+\omega^2}$$

$$Q_{\kappa}^{-1}(\omega) = Q_{\kappa}^{-1}(\omega)\sum_{l=1}^{n}\frac{Y_l^{\kappa}\omega_l^2}{\omega_l^2+\omega^2} + \sum_{l=1}^{n}\frac{Y_l^{\kappa}\omega_l\omega}{\omega_l^2+\omega^2}$$

$$Q_{\kappa}^{-1}(\omega) = \sum_{l=1}^{n}\frac{\omega_l\omega + \omega_l^2 Q_{\kappa}^{-1}(\omega)}{\omega_l^2+\omega^2}Y_l^{\kappa}$$

and $$Q_{\mu}^{-1}(\omega) = \sum_{l=1}^{n}\frac{\omega_l\omega + \omega_l^2 Q_{\mu}^{-1}(\omega)}{\omega_l^2+\omega^2}Y_l^{\mu} \qquad \text{(A.33)}$$

Eq. (A.33) is numerically used and hence the frequencies are discrete quantities not continuous so that we need to have a certain rule to approximate the $Q(\omega)$ values accurately. Ref. [77] mentions that if the $Q(\omega)$ values are known at frequencies $\tilde{\omega}_k$; $k = 1,...,2n-1$, with $\tilde{\omega}_1 = \omega_1$, $\tilde{\omega}_{2n-1} = \omega_n$ and the relaxation frequencies ω_l are located equidistantly in a logarithmic scale, then using the least squares method leads to the coefficients Y_l. However, usually the quality factors for the viscoelastic P- and S-waves are given [74 - 77] so that we use Eq. (A.34) instead of Eq. (A.33) to calculate the coefficients, Y_l^p and Y_l^s using the least square method.

$$Q_{\nu}^{-1}(\tilde{\omega}_k) = \sum\nolimits_{l=1}^{n}\frac{\omega_l\tilde{\omega}_k + \omega_l^2 Q_{\nu}^{-1}(\tilde{\omega}_k)}{\omega_l^2+\tilde{\omega}_k^2}Y_l^{\nu};\ k = 1,...,2n-1;\ \nu \in \{p,\ s\} \qquad \text{(A.34)}$$

where Q_p and Q_s are quality factors which characterize the attenuation of the viscoelastic P- and S-waves, respectively [77].

After obtaining the coefficients, Y_l^p and Y_l^s, we obtain the coefficients, Y_l^κ and Y_l^μ with

$$Y_l^\kappa = \frac{(c_p^2 Y_l^p - \frac{4}{3} c_s^2 Y_l^s)}{(c_p^2 - \frac{4}{3} c_s^2)}; \quad Y_l^\mu = Y_l^s \tag{A.35}$$

where c_p and c_s are the elastic P- and S- wave velocities, respectively.

Bibliography

[1] Kohno H, Bathe KJ, Wright JC. *"A finite element procedure for multiscale wave equations with application to plasma waves"*. COMPUT STRUCT 2010;88:87–94.

[2] De S, Bathe KJ. *"The method of finite spheres"*. COMPUT MECH 2000; 25; 329-345.

[3] Macri M, De S. *"Enrichment of the method of finite spheres using geometry-independent localized scalable bubbles"*. INT J NUMER METH ENG 2007; 69; 1-32.

[4] De S, Bathe KJ. *"Displacement/pressure mixed interpolation in the method of finite spheres"*. INT J NUMER METH ENG 2001; 51; 275-292.

[5] Macri M, De S. *"Towards an automatic discretization scheme for the method of finite spheres and its coupling with the finite element method"*. COMPUT STRUCT 2005;83;1429-1447.

[6] Bathe KJ. *"Finite element procedures"*. PRENTICE HALL; 1996.

[7] Harari I. *"A survey of finite element methods for time-harmonic acoustics"*. COMPUT METH APPL 2006;195:1594–607.

[8] Bathe KJ. *"The finite element method"*. In: Wah B, editor. ENCYCLOPEDIA COMPUT SCI ENG. J. Wiley and Sons; 2009. p. 1253–64.

[9] Lee R, Cangellaris AC. *"A study of discretization error in the finite-element approximation of wave solutions"*. IEEE T ANTENN PROPAG 1992;40:542–9.

[10] Guddati MN, Yue B. *"Modified integration rules for reducing dispersion error in finite element methods"*. COMPUT METH APPL MECH ENG 2004;193:275–87.

[11] Ihlenburg F, Babuška I. *"Finite element solution of the Helmholtz-equation with high wave-number.1. The h-version of the FEM"*. COMPUT MATH APPL 1995;30:9–37.

[12] Ihlenburg F, Babuška I. *"Finite element solution of the Helmholtz equation with high wave number.2. The h-p version of the FEM"*. SIAM J NUMER ANAL 1997;34:315–58.

[13] Deraemaeker A, Babuška I, Bouillard P. *"Dispersion and pollution of the FEM solution for the Helmholtz equation in one, two and three dimensions"*. INT J NUMER METH ENG 1999;46:471–99.

[14] Babuška IM, Sauter SA. *"Is the pollution effect of the FEM avoidable for the Helmholtz equation considering high wave numbers?"*. SIAM REV 2000;42:451–84.

[15] Bathe KJ, Wilson EL. *"Stability and accuracy analysis of direct integration methods"*. EARTHQUAKE ENG STRUCT 1973;1:283–91.

[16] Chin RCY. *"Dispersion and Gibbs phenomenon associated with difference approximations to initial boundary-value problems for hyperbolic equations"*. J COMPUT PHYS 1975;18:233–47.

[17] Marfurt KJ. *"Accuracy of finite-difference and finite-element modeling of the scalar and elastic wave-equations"*. GEOPHYSICS 1984;49:533–49.

[18] Wang YC, Murti V, Valliappan S. *"Assessment of the accuracy of the Newmark method in transient analysis of wave-propagation problems"*. EARTHQUAKE ENG STRUCT 1992;21:987–1004.

[19] Zingg DW, Lomax H, Jurgens H. *"High-accuracy finite-difference schemes for linear wave propagation"*. SIAM J SCI COMPUT 1996;17:328–46.

[20] Lee JF, Lee R, Cangellaris A. *"Time-domain finite-element methods"*. IEEE T ANTENN PROPAG 1997;45:430–42.

[21] Juntunen JS, Tsiboukis TD. *"Reduction of numerical dispersion in FDTD method through artificial anisotropy"*. IEEE T MICROW THEORY 2000;48:582–8.

[22] Cherukuri HP. *"Dispersion analysis of numerical approximations to plane wave motions in an isotropic elastic solid"*. COMPUT MECH 2000;25:317–28.

[23] Krenk S. *"Dispersion-corrected explicit integration of the wave equation"*. COMPUT METH APPL MECH ENG 2001;191:975–87.

[24] Atkinson JH, Westerink JJ, Luettich RA. *"Two-dimensional dispersion analyses of finite element approximations to the shallow water equations"*. INT J NUMER METH Fl 2004;45:715–49.

[25] Yue B, Guddati MN. *"Dispersion-reducing finite elements for transient acoustics"*. J ACOUST SOC AM 2005;118:2132–41.

[26] Gabriel D, Plešek J, Kolman R, Valeš F. *"Dispersion of elastic waves in the contact-impact problem of a long cylinder"*. J COMPUT APPL MATH 2010;234:1930–6.

[27] Idesman AV, Schmidt M, Foley JR. *"Accurate finite element modeling of linear elastodynamics problems with the reduced dispersion error"*. COMPUT MECH 2011;47:555–72.

[28] Liu GR. *"Meshfree methods: moving beyond the finite element method"*. CRC PRESS, 2003.

[29] Melenk JM, Babuška I. *"The partition of unity finite element method: Basic theory and applications"*. COMPUT METH APPL MECH ENG 1996;139:289–314.

[30] Laghrouche O, Bettess P, Astley RJ. *"Modelling of short wave diffraction problems using approximating systems of plane waves".* INT J NUMER METH ENG 2002;54:1501–33.

[31] El Kacimi A, Laghrouche O. *"Numerical modelling of elastic wave scattering in frequency domain by the partition of unity finite element method".* INT J NUMER METH ENG 2009;77:1646–69.

[32] El Kacimi A, Laghrouche O. *"Improvement of PUFEM for the numerical solution of high-frequency elastic wave scattering on unstructured triangular mesh grids".* INT J NUMER METH ENG 2010;84:330–50.

[33] Gottlieb D, Orszag SA. *"Numerical analysis of spectral methods: Theory and applications".* CAPITAL CITY PRESS; 1993.

[34] Patera AT. *"A spectral element method for fluid-dynamics-laminar-flow in a channel expansion".* J COMPUT PHYS 1984;54:468–88.

[35] Komatitsch D, Vilotte JP. *"The spectral element method: An efficient tool to simulate the seismic response of 2D and 3D geological structures".* B SEISMOL SOC AM 1998;88:368–92.

[36] Komatitsch D, Vilotte JP, Vai R, Castillo-Covarrubias JM, Sanchez-Sesma FJ. *"The spectral element method for elastic wave equations-application to 2-D and 3-D seismic problems".* INT J NUMER METH ENG 1999;45:1139–64.

[37] Komatitsch D, Barnes C, Tromp J. *"Simulation of anisotropic wave propagation based upon a spectral element method"*. GEOPHYSICS 2000;65:1251–60.

[38] Lee U, Kim J, Leung AYT. *"The spectral element method in structural dynamics"*. SHOCK VIB 2000;32:451–65.

[39] Karniadakis GE, Sherwin SJ. *"Spectral/hp element methods for computational fluid dynamics"*. OXFORD UNIVERSITY PRESS; 2005.

[40] Stupazzini M, Zambelli C, Massidda L, Paolucci R, Maggio F, Prisco C. *"The spectral element method as an effective tool for solving large scale dynamic soil-structure interaction problems"*. In: PROCEEDINGS OF THE EIGHTH U.S. NATIONAL CONFERENCE ON EARTHQUAKE ENGINEERING, 2006.

[41] Seriani G, Oliveira SP. *"Dispersion analysis of spectral element methods for elastic wave propagation"*. WAVE MOTION 2008;45:729–44.

[42] Zhong WX, Howson WP, Williams FW. *"Precise solutions for surface wave propagation in stratified material"*. J VIB ACOUST 2001;123:198–204.

[43] Cho J, Lee U. *"An FFT-based spectral analysis method for linear discrete dynamic systems with non-proportional damping"*. SHOCK VIB 2006;13:595–606.

[44] Chakraborty A, Gopalakrishnan S. *"A spectral finite element model for wave propagation analysis in laminated composite plate"*. J VIB ACOUST 2006;128:477–88.

[45] Gopalakrishnan S, Chakraborty A, Roy Mahapatra D. *"Spectral finite element method"*. SPRINGER-VERLAG; 2008.

[46] Cockburn B, Karniadakis G, Shu CW. *"Discontinuous Galerkin methods: Theory, computation, and applications"*. SPRINGER; 2000.

[47] Arnold DN, Brezzi F, Cockburn B, Marini LD. *"Unified analysis of discontinuous Galerkin methods for elliptic problems"*. SIAM J NUMER ANAL 2002;39:1749–79.

[48] Brezzi F, Cockburn B, Marini LD, Suli E. *"Stabilization mechanisms in discontinuous Galerkin finite element methods"*. COMPUT METH APPL MECH ENG 2006;195:3293–310.

[49] Massimi P, Tezaur R, Farhat C. *"A discontinuous enrichment method for threedimensional multiscale harmonic wave propagation problems in multi-fluid and fluid-solid media"*. INT J NUMER METH ENG 2008;76:400–25.

[50] Petersen S, Farhat C, Tezaur R. *"A space-time discontinuous Galerkin method for the solution of the wave equation in the time domain"*. INT J NUMER METH ENG 2009;78:275–95.

[51] Belytschko T, Lu YY, Gu L. *"Element-free Galerkin methods".* INT J NUMER METH ENG 1994; 37; 229-256.

[52] Jia XF, Hu TY. *"Element-free precise integration method and its applications in seismic modeling and imaging".* GEOPHYS J INT 2006; 166; 349-372.

[53] Godinho L, Dors C, Soares D, Amado-Mendes P. *"Solution of time-domain acoustic wave propagation problems using a RBF interpolation model with "a priori" estimation of the free parameter".* WAVE MOTION 2011; 48; 423-440.

[54] Wong ASM, Hon YC, Li TS, Chung SL, Kansa EJ. *"Multizone decomposition for simulation of time-dependent problems using the multiquadric scheme".* COMPUT MATH APPL 1999; 37; 23-43.

[55] Sarra SA, Sturgill D. *"A random variable shape parameter strategy for radial basis function approximation methods".* ENG ANAL BOUND ELEM 2009; 33; 1239-1245.

[56] Atluri SN, Kim HG, Cho JY. *"A critical assessment of the truly Meshless Local Petrov-Galerkin (MLPG), and Local Boundary Integral Equation (LBIE) methods".* COMPUT MECH 1999;24;348-372.

[57] Soares D. *"Numerical modelling of electromagnetic wave propagation by Meshless Local Petrov-Galerkin formulations".* CMES-COMP MODEL ENG 2009; 50; 97-114.

[58] Nicomedes WL, Mesquita RC, Moreira FJS. *"The Meshless Local Petrov-Galerkin Method in two-dimensional electromagnetic wave analysis".* IEEE T ANTENN PROPAG 2012; 60; 1957-1968.

[59] Wen PH. *"Meshless Local Petrov-Galerkin (MLPG) method for wave propagation in 3D poroelastic solids".* ENG ANAL BOUND ELEM 2010; 34; 315-323.

[60] Liu MB, Liu GR. *"Smoothed Particle Hydrodynamics (SPH): an overview and recent developments".* ARCH COMPUT METHOD E 2010; 17; 25-76.

[61] Herreros MI, Mabssout M. *"A two-steps time discretization scheme using the SPH method for shock wave propagation".* COMPUT METHOD APPL M 2011; 200; 1833-1845.

[62] Lee NS, Bathe KJ. *"Effects of element distortions on the performance of isoparametric elements".* INT J NUMER METH ENG 1993;36:3553–76.

[63] Strouboulis T, Copps K, Babuška I. *"The generalized finite element method: An example of its implementation and illustration of its performance".* INT J NUMER METH ENG 2000;47:1401–17.

[64] Bathe KJ. *"Conserving energy and momentum in nonlinear dynamics: A simple implicit time integration scheme".* COMPUT STRUCT 2007;85:437–45.

[65] Christon MA. *"The influence of the mass matrix on the dispersive nature of the semi-discrete, second-order wave equation".* COMPUT METH APPL MECH ENG 1999;173:147–66.

[66] Achenbach JD. *"Wave propagation in elastic solids".* NORTH-HOLLAND; 1973.

[67] Aki K, Richards PG. *"Quantitative seismology".* UNIVERSITY SCIENCE BOOKS; 2002.

[68] Lai CG, Wilmanski K. *"Surface waves in geomechanics: Direct and inverse modelling for soils and rocks".* SPRINGER; 2005.

[69] Kausel E. *"Fundamental solutions in elastodynamics: A compendium".* CAMBRIDGE UNIVERSITY PRESS; 2006.

[70] Bermudez A, Hervella-Nieto L, Prieto A, Rodriguez R. *"An optimal perfectly matched layer with unbounded absorbing function for time-harmonic acoustic scattering problems".* J COMPUT PHYS 2007;223:469–88.

[71] Ham S, Bathe KJ, *"A finite element method enriched for wave propagation problems".* COMPUT STRUCT 2012; 94-95; 1-12.

[72] Duarte CA, Oden JT. *"An h-p adaptive method using clouds".* COMPUT METHOD APPL M 1996; 139; 237-262.

[73] Chazot JD, Nennig B, Perrey-Debain E. "*Numerical simulation of acoustic waves in air and poroelastic media using the partition of unity finite element method*". J ACOUST SOC AM 2013; 133; 32-42.

[74] Carcione JM, Kosloff D, Kosloff R. "*Wave-propagation simulation in a linear viscoelastic medium*". GEOPHYS J 1988; 95; 597-611.

[75] Lombard B, Piraux J. "*Numerical modeling of transient two-dimensional viscoelastic waves*". J COMPUT PHYS 2011; 230; 6099-6114.

[76] Kristek J, Moczo P. "*Seismic-wave propagation in viscoelastic media with material discontinuities: A 3D fourth-order staggered-grid finite-difference modeling*". B SEISMOL SOC AM 2003; 93; 2273-2280.

[77] Moczo P, Kristek J, Galis M, Pazak P, Balazovjech M. "*The finite-difference and finite-element modeling of seismic wave propagation and earthquake motion*". ACTA PHYS SLOVACA 2007; 57; 177-406.

[78] De S, Bathe KJ. "*The method of finite spheres with improved numerical integration*". COMPUT STRUCT 2001; 79; 2183-2196.

[79] Mazzia A, Ferronato M, Pini G. "*A comparison of numerical integration rules for the meshless local Petrov-Galerkin method*". NUMER ALGORITHMS, 2007; 45; 61-74.

[80] Liu Y, Belytschko T. "*A new support integration scheme for the weakform in mesh-free methods*". INT J NUMER METH ENG 2010; 82; 699-715.

[81] Grätsch T, Bathe, KJ. *"A posteriori error estimation techniques in practical finite element analysis"*. COMPUT STRUCT 2005; 83; 235-265.

[82] Noh G, Ham S, Bathe KJ. *"Performance of an implicit time integration scheme in the analysis of wave propagations"*. COMPUT STRUCT 2013; 123; 93-105.

[83] Mohamed MS, Laghrouche O, El-Kacimi A. *"Some numerical aspects of the PUFEM for efficient solution of 2D Helmholtz problems"*. COMPUT STRUCT 2010; 88; 1484-1491.

[84] Linton CM, Evans DV. *"The interaction of waves with arrays of vertical circular-cylinders"*. J FLUID MECH 1990; 215; 549-569.

[85] Bucalem ML, Bathe KJ. *"The mechanics of solids and structures - hierarchical modeling and the finite element solution"*. SPRINGER; 2011.

[86] Seounghyun H, Benjamin L, Bathe KJ. " The method of finite spheres for wave propagation problems". COMPUT STRUCT 2014; 142; 1-14.